

EFFECTIVE OPERATION AND CONTROL OF HYBRID WIND-PV WATER PUMPING SYSTEM WITH MINIMAL POWER ELECTRONICS INTERFACE

Thesis

Submitted in partial fulfillment of the requirements for the degree of
DOCTOR OF PHILOSOPHY

by

SACHIN ANGADI



DEPARTMENT OF ELECTRICAL AND ELECTRONICS ENGINEERING,
NATIONAL INSTITUTE OF TECHNOLOGY KARNATAKA,
SURATHKAL, MANGALORE -575025

MARCH, 2022

DECLARATION

by the Ph.D. Research Scholar

I hereby *declare* that the Research Thesis entitled “**Effective Operation and Control of Hybrid Wind-PV Water Pumping System with Minimal Power Electronics Interface**” which is being submitted to the **National Institute of Technology Karnataka, Surathkal** in partial fulfillment of the requirement for the award of the Degree of **Doctor of Philosophy in Electrical and Electronics Engineering** is a *bonafide report of the research work carried out by me*. The material contained in this Research Thesis has not been submitted to any University or Institution for the award of any degree.



.....
SACHIN ANGADI, 155064EE15P01

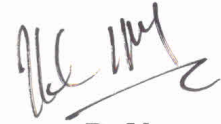
Department of Electrical and Electronics Engineering

Place: NITK-Surathkal

Date: 07-03-2022

CERTIFICATE

This is to *certify* that the Research Thesis entitled “**Effective Operation and Control of Hybrid Wind-PV Water Pumping System with Minimal Power Electronics Interface**” submitted by **Sachin Angadi** (Register Number: 155064EE15P01) as the record of the research work carried out by him, is *accepted as the Research Thesis submission* in partial fulfillment of the requirements for the award of degree of **Doctor of Philosophy**.



Prof. Udaykumar R. Yaragatti
(Research Guide)



Dr. Yellasiri Suresh
(Research Co-Guide)



Prof. Gururaj S. Punekar
(Chairman-DRPC, EEE dept.)

PROFESSOR & HEAD
DEPARTMENT OF ELECTRICAL AND ELECTRONICS ENGINEERING
NATIONAL INSTITUTE OF TECHNOLOGY KARNATAKA
SRINIVASNAGAR, SURATHKAL, MANGALORE- 575025, INDIA

Acknowledgements

It gives me immense pleasure and great sense of satisfaction to express my heartfelt gratitude to those who made this dissertation possible.

I express my sincere gratitude to my guides Prof. Udaykumar R. Yaragatti and Dr. Yellasiri Suresh for giving me an opportunity to work with them. I am extremely grateful for their invaluable and timely guidance during the course of my research work. I recall with pleasure the timely suggestions and useful discussions both academic and otherwise, I had with them during the research programme.

I wish to thank my research progress assessment committee (RPAC) members Dr. D. N. Gaonkar and Prof. A. Kandasamy, for their constructive feedback and guidance throughout the work. Thanks also goes to Dr. Jora M. Gonda, Dr. Vinatha U, Prof. B Venkatesaperumal and Prof. K.N.Shubanga former HODs for providing the necessary resources in the department to carry out my research. Also, I would like to thank present HOD, Prof. G.S.Punekar for his encouragement and suggestions. Special thanks to Dr. Sheron Figarado, Assistant Professor, Department of E & E , IIT Goa for his guidance during his service at NITK.

My heartfelt thanks to Prof. Ashok Shettar, Vice Chancellor and Prof. A. B. Raju, Head, E & E Dept., K.L.E Technological University, India., for having permitted me to complete my coursework at NITK Surathkal on deputation basis and funding my research work. I place on record my appreciation and sincere thanks to my colleagues of the department for having shared my teaching load during my absence and crucial times.

It gives me great pleasure to acknowledge the splendid support of my dear friends Mrs. Anisha Joseph, Dr. Pavana, Dr. Arjun Mudlapur,

Dr. Vijaybabu K and Mr. B Shiva Naik in sparing their time for technical discussions, proof reading of manuscripts and my thesis. Also, I would like to thank my undergraduate students Ms. Apeksha N. Patil, Mr. Shivu Tarihal and Ms. Amruta Bhatt, who helped me establish the experimental setup for my research work. I acknowledge the help of the lab staff at KLE Technological University, Mr. Ram Nargund and Mr. Sanjeev Bammigatti, for timely supply of the essential logistics to carry out my research work.

I would like to express my deepest gratitude towards my parents and my wife for their love and patience which kept me going in this journey. Their faith and unconditional love towards me are the reason for whatever I have achieved in my life.

Finally, I thank God Almighty for giving me strength at all times.

Abstract

With the growing population, the need for water and energy is compelled to increase. Employing conventional sources like fossil fuels for water pumping increases Green House Gas (GHG) emissions and the pump's Life Cycle Cost (LCC). For a sustainable future, it is inevitable to replace these conventional energy sources with renewable energy. Furthermore, with the recent advancement in power electronics and drives, renewables like solar PV and wind energy are becoming readily available for water pumping application, reducing GHG emissions and pump's LCC. Hence, considering the tremendous acceptance of renewable sources, especially solar photovoltaic (PV) and wind energy for Water Pumping System (WPS) using AC motor. This research work's primary objective is focused on effective operation and control of standalone hybrid Wind-PV WPS employing Induction Motor (IM) pump with reduced part count for better utilization of renewable energy sources.

The aforementioned problem statement is decomposed into solar PV fed boost converter and bidirectional Voltage Source Converter (VSC) assisted SEIG based Wind Energy Conversion System (WECS) to deliberate four notable contributions of this thesis. Firstly, a solar PV fed boost converter is investigated to examine the effect of input capacitor, digital filter cut-off frequency, system time constant and sampling time on implementing a perturbation-based Maximum Power Point Tracking (MPPT) algorithm. Based on two simple step tests, comprehensive guidelines to accomplish optimal performance of perturbation-based MPPT technique are suggested.

Secondly, two algorithms are proposed for bidirectional VSC assisted SEIG feeding IM pump, one for DC-link voltage regulation (DC-link voltage regulation scheme) and another for MPPT (speed sensorless hill-climbing MPPT algorithm). The advantage of the proposed DC-link voltage regulation scheme is that it senses only DC-link voltage for algorithm processing. The merit of the proposed speed sensorless hill-climbing MPPT algorithm is that it requires only dc-link voltage and two SEIG line currents information and is independent of other system parameters making

the algorithm easy to implement, generic and cost-effective. Additionally, these developed algorithms ensure a constant 'V/F' ratio of the supply at the Point of Common Coupling (PCC) for the entire operating range to prevent saturation issues concerning the SEIG and the IM pump. Decisively active and reactive power balance is investigated for both algorithms to demonstrate power balance at the PCC.

Lastly, a stand-alone hybrid Wind-PV Water Pumping System (WPS) with minimal power electronics interface, low-complex composite controls and optimal Energy Management Strategy (EMS) for effective utilization of both renewable sources is proposed. The system consists of Perturb and Observe (P&O) algorithm applied to the boost converter of the Solar PV system and voltage regulation algorithm/hill-climbing MPPT algorithm with Zero Steady-State Oscillation (ZSSO) applied to bidirectional VSC of WECS for optimal power extraction at all times. Besides optimal power extraction from the renewables, the proposed composite controller framework ensures a constant 'V/F' ratio at the PCC for the entire operating range against variations in wind velocity, solar irradiation and load.

The solar PV system, WECS, the hybrid Wind-PV system and all the developed control schemes are modeled in MATLAB/Simulink[®] and the operability of these control algorithms are experimentally verified using a low-cost TMS320F28069M controller. Extensive simulation and test results are presented to prove the viability of the proposed control schemes.

Contents

Abstract	i
List of figures	iii
List of tables	iv
Nomenclature	v
1 Introduction	1
1.1 Context	1
1.2 Literature Review	2
1.2.1 Multi-stage SPWPS	4
1.2.1.1 Research on WPS with IM drive	4
1.2.1.2 Research on WPS with BLDCM/PMSM drive	6
1.2.1.3 Research on WPS with SRM drive	6
1.2.1.4 Observations	6
1.2.2 Single-stage SPWPS	8
1.2.2.1 Research on WPS with IM drive	8
1.2.2.2 Research on WPS with BLDCM/PMSM drive	9
1.2.2.3 Research on WPS with SRM drive	9
1.2.2.4 Observations	10
1.2.3 Wind WPS	11
1.2.3.1 Stand-alone Wind WPS	11
1.2.3.2 Stand-alone WECS feeding test loads	11
1.2.3.3 Observations	12
1.2.4 Hybrid Wind-PV WPS	13
1.2.4.1 Stand-alone hybrid Wind-PV WPS	13
1.2.4.2 Stand-alone hybrid Wind-PV system feeding test loads	15
1.2.4.3 Observations	16

1.3	Motivation	19
1.4	Problem Statement	19
1.5	Research Objectives	20
1.6	Organization of the Thesis	21
2	Maximum Power Point Tracking of Solar PV System	23
2.1	Introduction	23
2.2	System Description	24
2.3	Effects of System parameters on System Time Constant	25
2.3.1	Input Capacitance	25
2.3.2	Digital Filter Cut-off frequency	25
2.3.3	Sampling time	26
2.4	Mathematical Modeling	26
2.4.1	Solar PV array	27
2.4.2	Boost Converter	27
2.5	Proposed Tests and Guidelines for System Parameter Based Performance Optimization	28
2.5.1	Step Test 01—Optimum Value Input Capacitance	28
2.5.2	Step Test 02—Optimum Digital Filter Cut-Off Frequency (ω_c)	30
2.5.3	Proposed Guidelines for the Choice of Sampling Time	32
2.6	Simulation and Experimental Study	33
2.6.1	Simulation Results	33
2.6.2	Experimental Results	35
2.7	Comparative Analysis	37
3	Voltage Regulation Algorithm for SEIG Based WECS	39
3.1	Introduction	39
3.2	System Description	40
3.3	Mathematical Modeling	41
3.3.1	Wind-Turbine Characteristics	41
3.3.2	Bidirectional Voltage Source Converter	42
3.3.3	Passive line filter	43
3.3.4	Self Excited Induction Generator	43
3.3.5	Induction Motor Pump	44
3.3.6	Active and Reactive Power at the PCC	44

3.4	DC-link Voltage Regulation (VR) Algorithm	45
3.4.1	Principle of Operation	45
3.4.2	Need for Constant ‘V/F’ ratio at the PCC	46
3.4.3	Controller Framework	47
3.5	Simulation and Experimental study	48
3.5.1	Simulation results	48
3.5.2	Experimental Results	52
4	Maximum Power Point Tracking of SEIG Based WECS	57
4.1	Introduction	57
4.2	System Description	57
4.3	Speed Sensorless Hill-Climbing algorithm	59
4.3.1	Operating Principle	59
4.3.2	Controller Framework	60
4.4	Simulation and Experimental Study	62
4.4.1	Simulation Results	62
4.4.2	Experimental Results	65
4.5	Comparative Analysis	68
5	Composite Controller for Hybrid Wind-PV Water Pumping System	71
5.1	Introduction	71
5.2	System description	72
5.3	Mathematical Modeling	74
5.4	Composite Controller Framework and Operation	74
5.4.1	Control Strategy for Solar PV system	76
5.4.2	Control Strategies for SEIG based WECS	76
5.4.2.1	DC-link Voltage Regulation (VR) Algorithm	76
5.4.2.2	Hill-Climbing MPPT Algorithm with ZSSO	77
5.4.2.3	SVPWM pulse generation with constant ‘V/F’ ratio.	78
5.4.3	Dump-load with ELC	79
5.4.4	Composite controller for hybrid Wind-PV WPS	80
5.5	Energy Management Strategy	80
5.5.1	Proposed Energy Management Strategy	80
5.5.2	Choice of Algorithm for SEIG based WECS	81
5.5.2.1	Voltage Regulation (VR) Algorithm	82

5.5.2.2	Hill-climbing MPPT algorithm	82
5.5.2.3	Suggestions	82
5.6	Simulation and Experimental study	83
5.6.1	Simulation Results	83
5.6.2	Experimental Results	85
5.7	Comparative analysis	89
6	Conclusions and Future Scope	93
6.1	Conclusions	93
6.2	Scope for Future Work	95
A	System Attributes	97
A.1	Solar PV array	97
A.2	Induction machine parameters	98
A.3	Wind-Turbine Characteristics	99
B	Experimental Setup	101
B.1	Solar PV System	101
B.2	SEIG based WECS	102
B.3	Hybrid Wind-PV Water Pumping System	103
B.4	Control Strategies: Model Based Design	104
	Bibliography	107
	Publications Based on the Thesis	116

List of Figures

1.1	Block level representation of Multi-stage SPWPS	4
1.2	Block level representation of Single-stage SPWPS	8
1.3	Block diagram of hybrid Wind-PV system for DC motor pump (Vick and Neal, 2012)	14
1.4	Block diagram of renewable energy hybrid power system for agricultural applications (Traoré et al., 2018)	14
1.5	Hybrid Wind-PV based AC and DC micro-grid implementation (Parida et al., 2018)	15
1.6	Proposed system description	20
2.1	Circuit diagram of solar photovoltaic (PV) fed boost converter and system controller	24
2.2	Equivalent circuit of single diode model of solar PV cell and boost converter using switching function	27
2.3	Experimental results: Step response of PV voltage and current for different values of input capacitance (C_{pv})	29
2.4	Experimental results: Step response of PV voltage (in p.u) for different cut-off frequencies of first order digital filter	31
2.5	Simulation results: (a) Duty ratio, (b) PV current, (c) PV voltage and (d) PV power with sampling time of 0.4 s	34
2.6	Simulation results: (a) Duty ratio, (b) PV current, (c) PV voltage and (d) PV power with sampling time of 0.1 s	34
2.7	Experimental results: (a) Duty ratio, (b) PV current, (c) PV voltage and (d) PV power with sample time of 0.4 s	35
2.8	Experimental results: (a) Duty ratio, (b) PV current, (c) PV voltage and (d) PV power with sample time of 0.3 s	35

2.9	PV power for different sampling times (Power read back accuracy of $\pm 0.28\%$ recorded using Magna Solar Emulator SL300-5/85-265)	37
3.1	Circuit diagram of the wind turbine driven, VSC assisted SEIG feeding IM pump with DC-link voltage regulation algorithm	40
3.2	Plot of line current versus frequency for Variable Frequency Drive (VFD) feeding 0.75 HP induction motor with and without constant ‘V/F’ control	46
3.3	Structure of DC-link voltage regulation scheme with constant ‘V/F’ ratio	47
3.4	Simulation results: (a) Wind velocity profile, (b) Wind power coefficient, (c) DC-link voltage, (d) Frequency, (e) Amplitude modulation index, (f) Shaft speed of the SEIG	49
3.5	(a) Fundamental RMS Line voltage and Frequency (b) ‘V/F’ ratio for entire operating range	51
3.6	Active power flow at PCC	51
3.7	Reactive power flow at PCC	51
3.8	Starting performance of the SEIG	52
3.9	DC-link Voltage	53
3.10	Frequency and amplitude modulation index	53
3.11	Dynamic behavior of system currents and voltages for DC-link Voltage Regulation (VR) algorithm: (a) VSC currents, (c) SEIG currents, (e) IM pump currents and (g) Line voltages at PCC for entire operating range ($t = 0 - 20$ s); Steady-state behavior of system currents and voltages for $v_w = 9$ m/s : (b) VSC currents, (d) SEIG currents, (f) IM pump currents and (h) Line voltages at PCC	54
4.1	Circuit diagram of wind-turbine driven, VSC assisted SEIG feeding IM pump with speed sensorless hill-climbing MPPT algorithm	58
4.2	(a) Power coefficient curve (b) Mechanical power developed by wind turbine for varying wind velocity	59
4.3	Hill-Climbing Algorithm for VSC assisted SEIG based WECS with frequency (F) as control variable	61

4.4	Simulation results: (a)Wind velocity profile, (b) Wind power coefficient, (c) Mechanical shaft speed of the SEIG, (d) Active power developed by the wind-turbine, (e) Operating frequency of the VSC, (f) Active power generated by the SEIG, (g) Amplitude modulation index, (h) Active power consumed by the IM pump, (i) DC-link voltage, (j) Active power dissipated in dump load	63
4.5	(a) Fundamental RMS Line voltage and Frequency of the supply at the PCC, (b) ‘V/F’ ratio of the supply at the PCC for entire operating range	64
4.6	Starting performance of the SEIG	65
4.7	DC link Voltage	66
4.8	Frequency and amplitude modulation index	66
4.9	Dynamic behavior of system currents and voltages for speed sensorless hill-climbing MPPT algorithm: (a) VSC currents, (c) SEIG currents, (e) IM pump currents and (g) Line voltages at PCC for entire operating range (t = 0 - 2 0 s); Steady-state behavior of system currents and voltages for $v_w = 10$ m/s : (b) VSC currents,(d) SEIG currents, (f) IM pump currents and (h) Line voltages at PCC	67
5.1	Circuit diagram of proposed stand-alone hybrid Wind-PV based water pumping system	73
5.2	Mathematical model of the hybrid Wind-PV WPS	74
5.3	Structure of proposed composite controller implementation for the hybrid Wind-PV WPS	75
5.4	Proposed hill-climbing MPPT algorithm with ZSSO for SEIG based WECS	78
5.5	Flowchart of Energy management strategy	81
5.6	Simulation Results: (a) Solar irradiance and wind velocity profile, (b) Duty ratio of boost converter, (c) DC-link voltage, (d) Solar PV power, (e) Operating frequency of the VSC, (f) SEIG active power, (g) Amplitude modulation index of the VSC, (h) IM pump active power, (i) Wind power coefficient, (j) Dump load active power	84
5.7	DC link Voltage	86
5.8	Frequency and amplitude modulation index	87
5.9	Duty ratio of the boost converter	87

5.10	Dynamic behavior of system currents and voltages for proposed composite controller: (a) VSC currents, (c) SEIG currents, (e) IM pump currents and (g) Line voltages at PCC for entire operating range ($t = 0 - 40$ s); Steady-state behavior of system currents and voltages for $F = 40$ Hz : (b) VSC currents, (d) SEIG currents, (f) IM pump currents and (h) Line voltages at PCC	88
B.1	Experimental setup of solar PV system	101
B.2	Experimental setup of SEIG based WECS	102
B.3	Experimental setup of hybrid Wind-PV WPS	103
B.4	Model Based Design Framework using Altair Embed and TMS320F28069M for Rapid Control Prototyping and Interactive HIL simulation	104

List of Tables

1.1	Summary of multi-stage SPWPS	7
1.2	Summary of single-stage SPWPS	10
1.3	Summary of Wind WPS	12
1.4	Summary of Hybrid Wind-PV WPS	18
2.1	Steady state values of system variables	33
2.2	Steady-state efficiency of P&O algorithm recorded for different sampling times (Power read back accuracy of $\pm 0.28\%$ recorded using Magna Solar Emulator SL300-5/85-265)	36
2.3	Steady state values of system variables for theoretical, simulation and experimental studies ($T_s = 0.4$ s)	37
2.4	Comparison of methods for choice of sampling time in solar photovoltaic systems	38
4.1	Qualitative comparison of MPPT techniques for WECS	69
5.1	Steady-state active and reactive power recorded at every interval for entire operating range ($t = 0-40$ s)	89
5.2	Comparison of available controllers with proposed composite controller for hybrid Wind-PV water pumping system	91
A.1	Solar PV array specifications	97
A.2	Electrical Machine specifications	98
A.3	Co-efficients of Magnetization Curve of 1.5 HP SEIG	98
A.4	Wind-Turbine Specifications	99
B.1	Particulars of components used to develop laboratory prototype of solar PV fed boost converter	102

B.2 Particulars of components used to develop laboratory prototype of SEIG based WECS	103
--	-----

Nomenclature

AC	Alternating current
ADC	Analog to Digital Converter
APC	Active Power Control
AWPRC	Anti-Windup Proportional Resonant Controller
BLDCM	Brushless DC Motor
CSC	Canonical Switching Cell
CVC	Constant Voltage Control
DC	Direct current
DCD-RLS	Dichotomous Coordinate Descent-Recursive Least Squares
DFIG	Doubly Fed Induction Generator
DTC	Direct Torque Control
ELC	Electronic Load Control
EMS	Energy Management Strategy
FLS	Fuzzy logic systems
FOC	Field Oriented Control
GHG	Green House Gas
GR	Gear Ratio
IFOC	Indirect Field Oriented Control
IM	Induction Motor
INC	Incremental Conductance
LCC	Life Cycle Cost
MLUT	Modified Look Up Table
MPP	Maximum power point
MPPT	Maximum power point tracking
MRAS	Model Reference Adaptive System
PCC	Point of Common Coupling
PMSM	Permanent Magnet Synchronous Motor
PMSG	Permanent Magnet Synchronous Generator
PSO	Particle Swarm Optimization
PTO	Predictive torque control
PV	Photovoltaic
PWM	Pulse Width Modulation

P&O	Perturb and Observe
REWPS	Renewable Energy based Water Pumping System
SEIG	Self Excited Induction Generator
SIDO	Single Input Dual Output
SPWM	Sinusoidal Pulse Width Modulation
SPWPS	Solar Photovoltaic Water Pumping System
SRM	Switched Reluctance Motor
SVC	Static Voltage Compensator
SVPWM	Space Vector Pulse Width Modulation
TCR	Thyristor Controlled Reactor
TIBO	Two Inductor Boost Converter
TLBO	Teaching Learning Based Optimization
VFD	Variable Frequency Drive
VSI	Voltage Source Inverter
VSC	Voltage Source Converter
VVVF	Variable Voltage Variable Frequency
V/F	Voltage / Frequency ratio
WECS	Wind Energy Conversion System
WPS	Water Pumping System
ZSSO	Zero Steady-State Oscillation
a	Diode ideality factor
$a_0 - a_6$	Coefficients of magnetization curve of 1.5 HP SEIG
C_{dc}	DC link capacitance (output capacitance of boost converter)
C_f	Filter capacitance
C_{pv}	Input capacitance
$C_1 - C_6$	Coefficients of wind-turbine model
D	Duty cycle
E_g	Bandgap energy of the semiconductor (1.12 eV for polycrystalline Si at 25 ° C)
F	Stator frequency of the SEIG
F_{sb}	Switching frequency of the boost converter
F_s	Switching frequency of the VSC
F_{rated}	Rated frequency of the motor
G	Solar irradiation incident on solar PV module
G_n	Solar irradiation incident on solar PV module at STC

H_1, H_2, H_3	Hall sensor signals from BLDCM
i_d	Current through bypass diode
i_{dr}	Rotor direct axis current of SEIG
i_{ds}	Stator direct axis current of SEIG
i_L	Inductor current of the boost converter
i_m	SEIG magnetizing current
i_0	Saturation current of the parallel diode
i_{ph}	Photo current
$i_{ph,n}$	Nominal photo current
i_{av}, i_{bv}, i_{cv}	VSC phase currents
i_{as}, i_{bs}, i_{cs}	SEIG phase currents
i_{ai}, i_{bi}, i_{ci}	IM pump phase currents
i_{dc}	DC-link current
i_{pv}	PV output current
i_{qr}	Rotor quadrature axis current of SEIG
i_{qs}	Stator quadrature axis current of SEIG
i_{sc}	Short circuit current of the panel
$i_{sc,n}$	Short circuit current of the panel at STC
J	Moment of inertia of SEIG
k	Boltzman constant
K_p	Pump constant
K_I	Short circuit current/temperature coefficient of the solar PV module
L	Boost converter inductance
L_f	Filter inductance
L_r	Rotor inductance of SEIG
L_s	Stator inductance of SEIG
L_{lr}	Rotor leakage inductance of SEIG
L_{ls}	Stator leakage inductance of SEIG
L_m	Magnetising inductance of SEIG
m_a	Amplitude modulation index
N_r	Motor speed in revolutions per minute
P	Number of poles in SEIG
P_{mp}	Power at maximum power point of solar PV array
P_t	Wind-turbine power

P_s	SEIG active power
q	Charge of the electron ($1.60217646 \times 10^{-19} C$)
Q	Charge of input capacitor
Q_s	SEIG reactive power
r	Radius of the wind-turbine
R_r	Rotor resistance of SEIG
R_s	Stator resistance of SEIG
R_{se}	Series resistance of the PV panel
R_p	Shunt resistance of the PV panel
R_{mp}	Equivalent resistance offered by PV array at maximum power point
R_f	Filter inductance
R_0	Boost converter load resistance
S	Switching function
$S_1 - S_6$	PWM pulses applied to VSC
T_s	Sampling time
T_{es}	Electromagnetic torque of the SEIG
T_m	Load torque of the SEIG
T_t	Mechanical torque developed by Wind-turbine
T_L	Load torque of induction motor pump
T_c	Actual temperature of PV cell
T_n	Nominal temperature of PV cell
t	Time in seconds
v_{dc}	DC link voltage
v_{dref}	Reference DC link voltage
V_{Lrms}	Line-line RMS voltage
v_{ab}, v_{bc}, v_{ca}	Line voltages at PCC
v_{dr}	Rotor direct axis voltage of SEIG
v_{ds}	Stator direct axis voltage of SEIG
v_{pv}	PV output voltage
v_{qr}	Rotor quadrature axis voltage of SEIG
v_{qs}	Stator quadrature axis voltage of SEIG
v_T	Thermal voltage of the diode
v_{OC}	Open circuit voltage of the PV panel
v_{mp}	PV array voltage at maximum power point

$v_{OC,n}$	Open circuit voltage of the PV panel at STC
ΔD	Perturbation step size.
ω_r	Rotor speed of the SEIG in electrical rad/s
ω_c	Cut-off frequency of digital filter
ω_m	Induction motor speed
δ_T	Difference of nominal and actual temperature ($T_c - T_n$)
τ_1	Approximate system time constant of solar PV system
τ_2	Effective system time constant of solar PV system
λ	Tip speed ratio
ω_t	Wind-turbine shaft speed
ω_{sh}	SEIG shaft speed in mechanical rad/s
v_w	Wind velocity
β	Pitch factor

Chapter 1

Introduction

This chapter presents a brief overview of Renewable Energy based Water Pumping System (REWPS). Further, a critical review of solar PhotoVoltaic (PV), wind and hybrid Wind-PV water pumping systems are presented in particular to understand prevailing trends. The formulated problem statement and research objectives that the thesis answers are explained in the final sections of this chapter.

1.1 Context

Water is one of the crucial resources for the sustenance of life, and its scarcity is realized in many places. To cater to the need of water, over 30 million water pumps are installed in the country, consuming approximately 110 billion units of energy per annum (20% of the country's electricity consumption) (IEEFA, 2018). With the growing population, the need for water and energy is compelled to increase. Approximately 16.5% of the country's electricity used to pump the water is from fossil fuels contributing to global warming (Katherine, 2014). According to the Global Energy Assessment, there should be negative Global Greenhouse Gas (GHG) emissions after 2070 for a sustainable future (Olhoff and Christensen, 2020). This demands a significant transformation in the energy ecosystem of the country. Water Pumping System (WPS) driven by conventional energy result in increased GHG emission, leading to global warming. Additionally, they suffer other drawbacks like motor burnouts, maintenance due to grid voltage variations, frequent power cuts/outages, transmission, distribution losses and poor power quality of the grid. One solution to this problem is to explore the possibility of using renewable sources efficiently to meet

energy demands for water pumping. The advancement in power electronics and computing technologies has attracted many researchers to innovate and provide efficient REWPSs. Solar PV, solar thermal, wind energy, and biomass are the renewable sources used to pump water across the globe ([Gopal et al., 2013](#)). Solar PV and wind energy are the most widely used renewables due to their omnipresence, matured technology, and optimized cost. Besides GHG reductions, literature suggests that adapting renewable energy for water pumping leads to reduction in the Life Cycle Cost (LCC) of the WPS.

The LCC of a typical pumping system includes the cost of the motor pump, maintenance cost and the cost incurred for energy spent on pumping. The majority of the pumping LCC is due to the energy utilized for pumping ([Tutterow et al., 2002](#)). Thus, if the conventional energy is used for pumping, it will increase the LCC of the pump, carbon footprint, and GHG emissions. To overcome these limitations, use of renewable energy for pumping applications is strongly recommended. Furthermore, renewable energy sources like solar PV and wind energy are stochastic and non-linear. Hence, an appropriate power conditioning circuit and control schemes are needed to extract maximum power from the chosen renewable source/s yielding optimal LCC of REWPS. This firmly builds the motivation to investigate control strategies, power conditioning circuits, and motors used in REWPS to utilize renewable energy sources effectively.

1.2 Literature Review

This section presents a detailed review of the research in REWPS. So far, numerous review articles on REWPSs are published in the literature. Authors ([Gopal et al., 2013](#)) have identified solar PV, solar thermal, biomass, wind and hybrid wind-PV sources as five possible renewable energy sources that can be used to pump water. The solar PV, wind energy, and hybrid wind-PV systems are reported to be potential sources that will evolve with time for efficient and clean water pumping. Subsequently, ([Periasamy et al., 2015](#)) have studied classification of Solar PhotoVoltaic Water Pumping System (SPWPS) based on DC motor and AC Induction Motor (IM) driven systems. The article focuses on electrical and control Engineering perspectives like power converter stages, Maximum Power Point Tracking (MPPT) algorithms and microcontroller used for implementation of DC motor and AC IM pumps.

Authors ([Chandel et al., 2015](#)) have investigated several parameters like economic viability, pumping technology, performance analysis of installed SPWPS, sizing, degradation study, and efficiency improvement of SPWPS. The research articles investigated for efficiency improvement in this paper are minimal. Next, ([Rawat et al., 2016](#)) have presented the detailed design procedure for standalone and grid-connected SPWPS. Besides, methods for size optimization and modeling techniques for a solar PV system are also presented. Following this, ([Sontake and Kalamkar, 2016](#)) have framed SPWPS to be an interdisciplinary problem discussing challenges in fields like Mechanical, Electrical, Electronics, Computer, Control and Civil Engineering. Since the broad spectrum of challenges are being addressed, the topics concerning types of motors and control algorithms are discussed in brief.

Lately, ([Muhsen et al., 2017](#)) studied design procedures, SPWPS modeling, field performance, reliability, system sizing, and control strategies. In addition, some research articles based on control strategies concerning only DC motor based water pumps are discussed. Similarly, ([Chandel et al., 2017](#)) have studied directly coupled SPWPS and also presented a case study of 0.5 HP mono-block directly coupled dc motor pump in western Himalayan region of India. It is reported that directly coupled SPWPS suffer under-utilization and need MPPT algorithm for effective utilization of solar PV power. Recently, ([Li et al., 2017](#)) have investigated SPWPS with factors concerning system efficiency and optimization. In addition, the performance of several installed SPWPS have been assessed. Decisively the article strongly recommends integration of solar PV with other green technologies like wind energy for sustainable water pumping.

It is apparent from the reported reviews that the overall system efficiency is dependent on numerous factors, namely system sizing, pumping technology, economic viability and performance assessment spanning various branches of Engineering. However, the focus of this research lies in the electrical engineering aspects of REWPS. Hence, in subsequent sections, the different research avenues like the type of the motor pump, power electronic interface, and control strategies will be critically reviewed on the following topics in REWPS.

- Multi-stage AC motor based SPWPS.
- Single-stage AC motor based SPWPS.
- Wind energy based WPS.

- Hybrid Wind-PV based WPS.

1.2.1 Multi-stage SPWPS

The generic block diagram of multi-stage SPWPSs is shown in Figure 1.1, which encapsulates research avenues namely DC-DC converter (A), motor driver (B), motor (C), control strategy for A (D), control strategy for B (E), sensor inputs for D (F) and sensor inputs for E (G). Multi-stage SPWPSs consists of two power conditioning units between solar PV source and the motor pump. The first stage is meant for tracking maximum power from the solar PV source and typically a high gain DC-DC converter is used to step up the PV voltage. The second stage is employed for motor control and is specific to the motor used for pumping. Numerous motors are used for pumping namely Induction Motor (IM), Brushless DC Motor (BLDCM), Permanent Magnet Synchronous Motor (PMSM) and Switched Reluctance Motor (SRM). In this section, the literature for each of the motor pump is presented in particular.

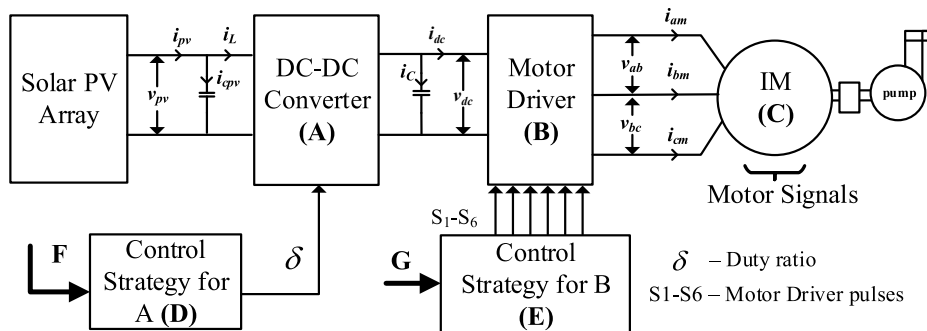


Figure 1.1: Block level representation of Multi-stage SPWPS

1.2.1.1 Research on WPS with IM drive

This section presents the research on IM based pump. Firstly the scalar control methods are discussed followed by vector control methods. Erstwhile, (Yao et al., 1994) have implemented square wave drive mode with frequency control to improve the performance of SPWPS. A simple MPPT algorithm using Constant Voltage Control (CVC) is employed using boost converter. The system is compared with conventional fixed frequency motor drive for efficiency improvement. Next, (Caracas et al., 2013) have proposed a Two-Inductor Boost Converter(TIBO) for high voltage gain and low input current ripple. Standard ‘V/F’ based Sinusoidal Pulse Width Modulation

(SPWM) is implemented for VSI fed IM pump. This system is reported to be tested for the commercial water pump and is reported to exhibit satisfactory performance. Further, (Singh et al., 2018) have discussed a simple control strategy for IM pump with a reduced number of sensors employing pump affinity laws for improved stability. The boost converter is used to track MPP using INC algorithm. Recently, considerable effect of partial shading on SPWPS is studied by (Mudlapur et al., 2019). The consequences of effects like high varying panel voltage and transients in the DC-DC converter on the overall system is investigated.

With the advancement in power semiconductor technology and availability of high-speed microcontrollers, few researchers have explored the vector control algorithms for IM based pumps. (Vitorino et al., 2011) have made vital contributions like the design of high gain Push-Pull DC-DC converter and efficient optimization algorithms for IM pump. Extensive investigations concerning vector control algorithms in addition to efficiency optimization of IMs have been carried out and Indirect Field Oriented Control (IFOC) with power factor optimization is reported to yield optimal results. A multimachine irrigation system is proposed by (Bhende and Malla, 2012) employing conventional Perturb and Observe (P&O) algorithm for MPPT and vector control algorithm for DC-link voltage regulation, demonstrating effective pumping with battery less operation. Next, (Singh and Singh, 2015) have proposed pump affinity laws to derive the reference speed for each irradiation. Further, the error in speed is processed by forcing appropriate currents hence optimizing the pump flow rate. A P&O algorithm is used to generate pulses for boost converter to extract maximum power. A satisfactory steady state and dynamic performance for varying irradiances is reported using pump affinity laws. Later on, (Talbi et al., 2018) have presented battery-less SPWPS employing P&O algorithm with variable step-size for MPPT and Predictive torque control (PTC), flux control and a fuzzy logic controller (Takagi-Sugeno type) for DC-link voltage regulation of the IM drive. The overall control strategy is reported to provide reduced torque ripple and improved torque response. Subsequently, (Singh and Shukla, 2018) have proposed Direct Torque Control (DTC) for IM pump with a novel Model Reference Adaptive System (MRAS) technique. The proposed MRAS technique eliminates the speed, voltage and current sensors. Adaptive parameter estimation is incorporated to overcome the changes in motor parameters due to temperature variation. Recently, (Errouha et al., 2019) have proposed IFOC with loss minimization and MPPT algorithm leading to enhanced

energy utilization. Lastly, Active Power Control (APC) with the Anti-Windup Proportional Resonant Controller (AWPRC) for AC voltage regulation is proposed by (Rezkallah et al., 2019). The overall strategy though complicated results in enhanced energy extraction, improved power quality, and better transient response for SPWPS.

1.2.1.2 Research on WPS with BLDCM/PMSM drive

Permanent magnet motors although expensive, offer merits like high efficiency, power density and superior power factor of operation. Hence few researchers have ventured in exploring the capabilities of BLDCM and PMSM for water pumping. (Kumar and Singh, 2016) have carried out investigations on BLDCM based water pump for improved results under low irradianations. The speed of the motor pump is controlled by varying the DC-link voltage based on changes in solar irradianations. Only hall sensor signals are read as feedback signals, no information regarding DC-link voltage or line currents are captured for control. Eventually, (Kumar and Singh, 2019) proposed further improvisation by replacing hall sensors with voltage sensors making the system simple, compact and cost effective. Next, (Maissa et al., 2017) have proposed an algorithm for maximum power extraction by employing sliding mode control to boost converter to demonstrate superior performance of the proposed sliding mode controller against conventional P&O algorithm interms of efficiency and faster transient response.

1.2.1.3 Research on WPS with SRM drive

In comparison to asynchronous and permanent magnet motors, the SRM offers high efficiency, high torque at a lower cost due to its core construction. Hence, it qualifies as a potential alternative for water pumping application. Authors (Narayana et al., 2017) have studied the Canonical Switching Cell (CSC) converter to reduce the cost of the SRM based pump system. The continuous conduction mode of operation of the CSC converter is reported to reduce the stress on system components. Furthermore, the fundamental switching scheme of a mid-point converter results in reduced losses increasing the system efficiency. Next, (Mishra and Singh, 2017) have proposed a Single Input Dual Output (SIDO) converter for SRM based SPWPS with optimal energy extraction and soft starting feature and mid-point converter for driving motor pump.

1.2.1.4 Observations

Multi-stage SPWPS encapsulates a wide range of research avenues (with columns A to G) as summarized in Table 1.1. The research in multi-stage SPWPS can be broadly classified into MPPT algorithms and motor control algorithms. The variety is observed in MPPT tracker (A), motor used for water pumping (C), MPPT algorithms (D), motor control strategy (E) and sensors used for motor control strategy (G).

Table 1.1: Summary of multi-stage SPWPS

Ref.	MPPT Tracker (A)	Motor Driver (B)	Motor (C)	MPPT (D)	Algorithm	Control Strategy (E)	Sensors for D (F)	Sensors for E (G)
1	Boost C.	VSI	IM	P&O		Frequency control	i_{pv}, u_{pv}	$i_{am}, i_{bm}, u_{ab}, u_{bc}$
2	TIBO	VSI	IM	Hill Climbing algorithm		SVPWM	i_{pv}, u_{pv}	v_{dc}
3	Boost C.	VSI	IM	INC		SPWM	i_{pv}, u_{pv}	v_{dc}
4	Boost C.	VSI	IM	P&O for partial shading		SVPWM	i_{pv}, u_{pv}	v_{dc}
5	Push-pull C.	VSI	IM	P&O		IFOC Combined with balancing current	i_{pv}, u_{pv}	i_{am}, i_{bm}, v_{dc}
6	Boost C.	VSI	IM	P&O		Power & Voltage based vector control	i_{pv}, u_{pv}	$i_{am}, i_{bm}, v_{ab}, u_{bc}, v_{dc}, N$
7	Boost C.	VSI	IM	P&O		Reference current control	i_{pv}, u_{pv}	i_{am}, i_{bm}, N
8	Boost C.	VSI	IM	Current based P&O		Predictive torque & Flux controller	i_{pv}, i_s	i_{am}, i_{bm}
9	Boost C.	VSI	IM	Modified P&O		IFOC (speed, voltages and current estimation)	i_{pv}, u_{pv}	v_{dc}, i_{dc}
10	Boost C.	VSI	IM	P&O		IFOC with loss minimization	i_{pv}, u_{pv}	i_{am}, i_{bm}, N
11	Boost C.	VSI	IM	Power ratio variable step algorithm		Active power based AWPRC controller	i_{pv}, u_{pv}	$i_{am}, i_{bm}, u_{ab}, u_{bc}$
12	Zeta C.	VSI	BLDCM	INC		v_{dc} Control	i_{pv}, u_{pv}	H_1, H_2, H_3
13	Boost C.	VSI	BLDCM	INC		Sensorless Line-voltage Control	i_{pv}, u_{pv}	v_{ab}, v_{bc}
14	Boost C.	VSI	PMSM	P&O		SMC	i_{pv}, u_{pv}	i_{am}, i_{bm}
15	CSC C.	MPC	SRM	P&O		Commutation angle control algorithm	i_{pv}, u_{pv}	H_1, H_2, H_3
16	Buck-Boost C.	MPC	SRM	INC		dwell angle self starting algorithm	i_{pv}, u_{pv}	H_1, H_2, H_3

Note: A-MPPT Tracker, B-Motor Driver, C-Motor, D-MPPT Algorithm, E-Control strategy, F-Sensors for MPPT algorithm, G-Sensors for control strategy, C-Converter, MPC - Mid point converter

- | | | |
|-----------------------------|------------------------------|------------------------------|
| 1. (Yao et al., 1994) | 7. (Singh and Singh, 2015) | 13. (Kumar and Singh, 2019) |
| 2. (Caracas et al., 2013) | 8. (Talbi et al., 2018) | 14. (Maissa et al., 2017) |
| 3. (Singh et al., 2018) | 9. (Singh and Shukla, 2018) | 15. (Narayana et al., 2017) |
| 4. (Mudlapur et al., 2019) | 10. (Errouha et al., 2019) | 16. (Mishra and Singh, 2017) |
| 5. (Vitorino et al., 2011) | 11. (Rezkallah et al., 2019) | |
| 6. (Bhende and Malla, 2012) | 12. (Kumar and Singh, 2016) | |

A high gain DC-DC converter is chosen as MPPT tracker to match the PV voltage to the DC-link voltage. Referring to Table 1.1, it is evident that the motor driver chosen is VSI for all the motors except SRM. Perturbation based MPPT algorithms like P&O and INC have been popular among researchers; however, few intelligent

algorithms based on fuzzy logic are also implemented for improved efficiency. The motor control algorithms can be broadly classified into scalar and vector control algorithms. Scalar control is simple to implement and involves PWM techniques like SPWM and SVPWM. Vector control algorithms are classified into direct and indirect control based on the presence and absence of the speed sensor. Furthermore, vector control involves intensive computation, knowledge of machine parameters, and additional sensors and hence are not a preferred choice for commercial use in remotely located stand-alone applications. The sensors used for the MPPT algorithm are PV voltage and current (v_{pv} & i_{pv}) in most of the research. However, the sensors used for the motor control algorithm depends on the type of the algorithm (scalar or vector control) and the motor used for water pumping.

1.2.2 Single-stage SPWPS

The WPS with minimal (only one) stage of power processing unit between solar PV and AC motor pump is classified as single-stage SPWPS. Figure 1.2 shows the generic block diagram of single-stage SPWPS. It is evident from the Figure 1.2 that MPPT tracker (A) and the associated algorithm (D) are eliminated in single-stage SPWPS. Hence, the research avenues in single-stage SPWPS includes the motor driver (B), motor (C), the control strategy for B (E) and sensor inputs for E (G).

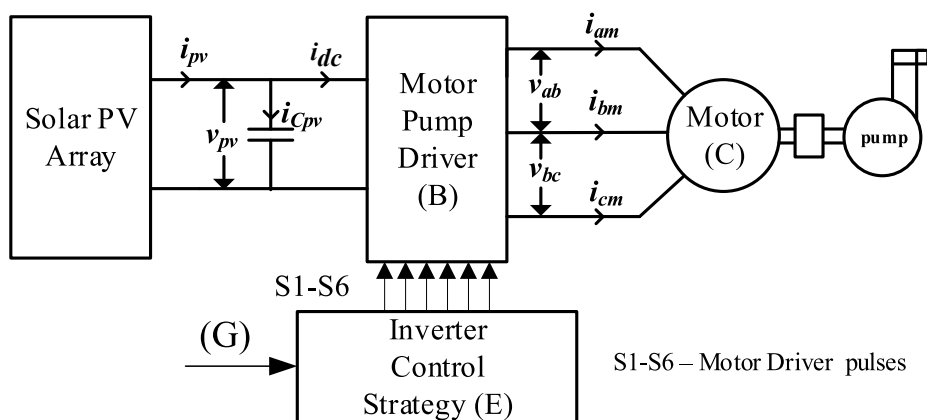


Figure 1.2: Block level representation of Single-stage SPWPS

1.2.2.1 Research on WPS with IM drive

Erstwhile, (Muljadi, 1997) attempted MPPT algorithm with AC motor based systems, A system of VSI along with IM is modeled as frequency dependent variable resistor. Frequency is suitably controlled to track MPP to utilize available energy from PV source efficiently. Later on, a novel six element circuit is proposed by (Driemeier and Zilles, 2010). The circuit proposed can be embedded into the conventional Variable Frequency Drive (VFD) fed IM system to extract maximum power from the PV source. Down the line, (Packiam et al., 2015) have conducted experiments using three Volts/Hertz based control strategies namely square wave drive, SPWM, and SVPWM with P&O as standard MPPT algorithm. It is concluded in the study that, SVPWM with P&O algorithm gives best results with fast transient response, less noise and a high lifetime of the system.

Authors (Moulay-Idriss and Mohamed, 2013) have implemented INC method to select an optimal speed for a given irradiation and temperature. The speed of the motor is regulated to the optimal speed by employing the DTC algorithm. The algorithm is reported to result in fast response, reduced steady-state oscillations and increased system efficiency. Further, a detailed investigations on the reduction of the number of sensors in single-stage IM based pump is conducted by (Shukla and Singh, 2018). The reduction in the number of sensors is reported to increase system stability and reduce the cost of the system. Lately, (Elkholy and Fathy, 2016) have presented a Teaching-Learning-Based Optimization (TLBO) algorithm to generate an optimal reference voltage corresponding to maximum power from the PV source. Further, DC-link voltage regulation is achieved using three level VSI to reduce filtering requirements of the system.

1.2.2.2 Research on WPS with BLDCM/PMSM drive

Authors (Sashidhar et al., 2018) have proposed the position sensor-less control algorithm for BLDCM pump. The proposed single-stage sensorless WPS is reported to result in increased reliability for use in the rural application, with an efficiency of 87% for the BLDC motor and 92% for the VSI at rated power.

Authors (Antonello et al., 2017) have proposed a single stage PMSM based SP-WPS to reduce cost and complexity without compromising on the utilization of available solar energy. Perturbation based extremum seeking controller sets speed reference

with a change in solar irradiation. VSI with conventional FOC regulates the speed to the desired value for maximum system efficiency. Recently, (Murshid and Singh, 2019) have developed an energy efficient PMSM drive for water pumping with least number of sensors for MPPT and motor control. System variables like speed, position, flux and voltages are estimated using only DC-link voltage for vector control of the motor. Modified P&O algorithm is employed using only DC-link voltage eliminating the use of current sensor.

1.2.2.3 Research on WPS with SRM drive

A simplified PWM based Modified Lookup Table (MLUT) approach for driving SRM motor and extracting maximum power from solar PV source is proposed by (Koreboina et al., 2017). The proposed algorithm is reported to offer reduced phase peak, torque ripple and noise of the system.

1.2.2.4 Observations

The research carried out in single stage SPWPS is summarized in Table 1.2. The crucial research avenue of single-stage SPWPS is the control strategy because it combines MPPT algorithm and motor control algorithm. The MPPT is formulated to generate the reference frequency (for scalar control) or speed (for vector control) for given irradiation using pump affinity laws. In the case of a scalar control algorithm, the frequency is used to generate SPWM or SVPWM pulses for VSI to extract maximum power from the solar PV source and drive the motor pump simultaneously. In vector control algorithm, the reference speed generated is used to implement sensed or sensorless algorithms to drive the VSI fed motor pump while extracting maximum power from the source. The discussions for the choice of motor, sensors and motor driver are same as discussions presented for multi-stage SPWPS in section 1.2.1.

1.2.3 Wind WPS

The performance of small aerogenerators, namely Self Excited Induction Generator (SEIG) and Permanent Magnet Synchronous Generators (PMSG) feeding different motors/loads employing power electronics interface used in stand-alone applications, are reviewed in this section.

Table 1.2: Summary of single-stage SPWPS

Ref.	Motor Driver (B)	Motor (C)	Control Strategy (E) for MPPT & motor control	Sensors for E (G)
1	VSI	IM	P&O + Feed forward control for variable frequency operation	i_{pv}, v_{pv}
2	VSI	IM	A Novel six element circuit + variable frequency control	v_{pv}
4	VSI	IM	INC+ Sensorless DTC	$v_{pv}, i_{am}, i_{bm}, v_{ab}, v_{bc}$
3	VSI	IM	P&O + Square wave drive, SPWM and SVPWM based Variable Voltage Variable frequency Control	i_{pv}, v_{pv}
5	VSI	IM	INC + Indirect FOC(Speed adaptive estimation using generalized integrator approach + Phase voltages estimation + phase current estimation)	i_{pv}, v_{pv}, v_{dc}
6	VSI	IM	ANN based MPPT + TLBO based motor control	i_{pv}, v_{pv}
7	VSI	PMSM	Novel MPPT + Conventional FOC	$i_{pv}, v_{pv}, i_{am}, i_{bm}, v_{ab}, v_{bc}, N$
8	VSI	PMSM	Modified P&O + sensorless FOC	v_{pv}, i_{am}, i_{bm}
9	VSI	BLDCM	INC+ Sensorless electronic commutation algorithm	i_{pv}, v_{pv}
10	Mid-point Converter	SRM	MLUT based MPPT + Simplified PWM algorithm	v_{pv}, N

Note: B-Motor Driver, C-Motor, E-Control strategy, G-Sensors for control strategy

- | | | |
|---------------------------------|--------------------------------------|------------------------------|
| 1. (Muljadi, 1997) | 4. (Moulay-Idriss and Mohamed, 2013) | 7. (Antonello et al., 2017) |
| 2. (Driemeier and Zilles, 2010) | 5. (Shukla and Singh, 2018) | 8. (Murshid and Singh, 2019) |
| 3. (Packiam et al., 2015) | 6. (Elkholy and Fathy, 2016) | 9. (Sashidhar et al., 2018) |
| | | 10. (Koreboina et al., 2017) |

1.2.3.1 Stand-alone Wind WPS

Erstwhile, (Shaltout and Abdel-Halim, 1995) have analysed stand-alone induction generator directly feeding an IM pump without intermediate DC-link. Maximum power extraction is demonstrated by adjusting the exciting current using static VAR compensator. Later, (Miranda et al., 1999) have studied IM based pump fed by wind-driven SEIG. PWM converter (VSI) with vector control is employed to control active and reactive power flow to the load while maintaining the terminal voltage constant. Next, (Ouchbel et al., 2014) have proposed an MPPT algorithm for wind-driven SEIG fed IM pump. A thyristor-based Static Voltage Compensator (SVC) is used to optimize the quantity of the pumped water. Additionally, a comparison of wind power utilized with and without MPPT algorithm is presented showing better energy utilization for system with the proposed MPPT algorithm.

A single phase IM pump fed by wind-driven PMSG is studied by (Lara et al., 2015). Operating efficiency of 70% to 95% is reported with proposed MPPT based ‘V/F’ algorithm.

Authors ([Zeddini et al., 2016](#)) have presented Particle Swarm Optimization (PSO) for a standalone, variable speed, wind-driven SEIG feeding IM pump with maximum power tracking. The proposed algorithm uses only power input and does not require knowledge of wind speed, air density, and turbine parameters to extract maximum power.

1.2.3.2 Stand-alone WECS feeding test loads

Lately, a trend of converting AC power generated by PMSG ([Koutroulis and Kalaitzakis, 2006](#), [Kazmi et al., 2010](#), [Chen et al., 2016](#), [Hussain and Mishra, 2016](#), [Fathabadi, 2017](#)) and SEIG ([Mishra et al., 2019](#)) to DC power and employing DC-DC converters for speed sensorless MPPT is fast emerging. DC-DC converters namely boost converter ([Koutroulis and Kalaitzakis, 2006](#), [Chen et al., 2016](#), [Fathabadi, 2017](#)), Sepic Converter ([Hussain and Mishra, 2016](#)) and buck converter ([Mishra et al., 2019](#)) are reported in the literature. Such systems primarily use perturbation-based techniques like hill-climbing algorithm ([Koutroulis and Kalaitzakis, 2006](#), [Fathabadi, 2017](#)), adaptive MPPT ([Kazmi et al., 2010](#), [Hussain and Mishra, 2016](#)), power control algorithm ([Chen et al., 2016](#)) and drift-free P&O ([Mishra et al., 2019](#)) for MPPT.

It is to be noted that, although the part count and sensed variables in aforementioned speed sensorless systems are minimal, the extracted power is fed into DC-bus or battery. Hence an additional converter is inevitable to transfer power to the real world application as witnessed in ([Boopathi et al., 2020](#)). As an exception, an investigation is carried out on maximum power extraction using SEIG employing a single VSC feeding generated power to the battery ([Bašić et al., 2021](#)). However, this algorithm uses machine parameters and complex optimization techniques for power processing which are difficult to implement using commercial microcontrollers/DSP's. Also, such systems require frequent tuning/maintenance and are not recommended for stand-alone systems deployed in remote locations.

1.2.3.3 Observations

The details of the research in wind WPS are summarized in Table 1.3. In the wind WPSs, the choice of the generator and the motor pump decides the power electronic interface and hence the control strategy. It is evident from Table 1.3 that the SEIG and the PMSG are the popular choices for power generation using wind-turbine. Fur-

Table 1.3: Summary of Wind WPS

Ref.	Generator	Load	PE. Interface	Control Strategy
(Shaltout and Abdel-Halim, 1995)	SEIG	IM pump	SVC	MPPT algorithm
(Miranda et al., 1999)	SEIG	IM pump	VSI	Voltage regulation
(Ouchbel et al., 2014)	SEIG	IM pump	SVC	MPPT algorithm
(Lara et al., 2015)	PMSG	SPIM pump	SVC	MPPT algorithms
(Zeddini et al., 2016)	SEIG	IM pump	TCR	MPPT using PSO
(Koutroulis and Kalaitzakis, 2006)	PMSG	Battery	Rectifier+Boost C.	Hill-climbing
(Kazmi et al., 2010)	PMSG	DC bus	Rectifier+Boost C.	Adaptive MPPT
(Chen et al., 2016)	PMSG	DC bus	Rectifier+Boost C.	Power control
(Hussain and Mishra, 2016)	PMSG	R-load	Rectifier+SEPIC C.	Adaptive MPPT
(Fathabadi, 2017)	PMSG	R-load	Rectifier+Boost C.	Hill-climbing
(Mishra et al., 2019)	SEIG	R-load	Rectifier+Buck C.	drift-free P&O
(Boopathi et al., 2020)	PMSG	IM pump	Rectifier+SEPIC+VSI	P&O
(Bašić et al., 2021)	SEIG	Battery	VSI	IRFO

thermore, it is observed that often PMSG is employed along with a diode rectifier and DC-DC converter feeding generic loads. Contrarily, the SEIG is used with minimal power electronics interface feeding IM pumps. Additionally, three phase induction machine offers merits like reduced cost, low maintenance and rugged construction. The power electronic interfaces for SEIG include thyristor-based circuits (SVC and TCR) and VSI to control the active and reactive power at the Point of Common Coupling (PCC). Decisively, it is observed that MPPT algorithms are fast emerging in Wind WPSs due to increased system efficiency.

1.2.4 Hybrid Wind-PV WPS

Renewable energy is very often seen as a clean and attractive choice for powering standalone applications in remote locations which are isolated from the grid. However solar or wind energy alone cannot be relied upon due to seasonal and daylight variations. Nevertheless, wind and solar PV sources exhibit complementary profiles. Hence hybrid Wind-PV systems for standalone applications can be seen as a reliable and feasible alternative to wind-diesel and battery coupled solar systems (Daniel and AmmasaiGounden, 2004). On this account, the hybrid Wind-PV based water pumping systems are reviewed in this section. Several researchers have investigated hybrid Wind-PV systems for standalone applications considering generic load (R/RL/non-linear loads). However, with little or no change in control strategy, the motor pump can be used in place of the generic load to study water pumping application. Hence, a few selected standalone hybrid Wind-PV systems are also discussed which can be

easily adopted for water pumping.

1.2.4.1 Stand-alone hybrid Wind-PV WPS

Authors (Vick and Neal, 2012) have presented an analysis of the following systems with DC motor pump: i) Solar PV water pumping system, ii) Wind-driven water pumping system and iii) Combined hybrid Wind-PV water pumping system for the same location. The topology configured for the hybrid Wind-PV WPS is shown in the Figure 1.3 . The performance of the hybrid system is reported to be superior to solar PV or wind energy system alone, subject to geographical location of the site. Recently, a multi-input DC-DC converter is proposed to extract maximum power from solar PV and wind turbine for water pumping using DC-motor (de Oliveira Ferreira et al., 2020). Though the proposition uses a minimal power electronics interface, it employs irradiance and wind velocity sensors for its operation making the overall system expensive. Next, a pumped hydro storage for the hybrid Wind-PV system is

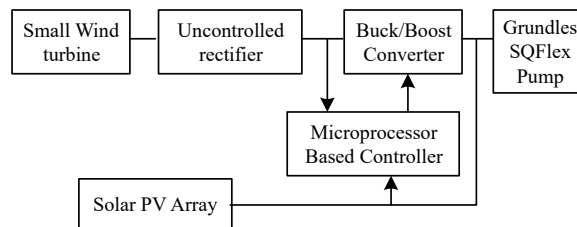


Figure 1.3: Block diagram of hybrid Wind-PV system for DC motor pump (Vick and Neal, 2012)

investigated by (Ma et al., 2014) to overcome limitations posed by intermittency of renewable sources. Several case studies are carried out on real-time data to report that hybrid Wind-PV with pumped hydro storage attains 100% energy autonomy for stand-alone applications. Further, (Traoré et al., 2018) have conducted investigations on renewable energy hybrid power system for agricultural applications shown in Figure 1.4. Three algorithms are investigated for energy management amidst renewable energy sources (SPV and wind energy), water pump, battery storage, and other small farm equipment. It is reported in the results that the third algorithm (which prioritizes the battery charging over water pumping and feeding other loads) results in the most significant system efficiency. Authors (Rehman and Sahin, 2016) have studied optimal sizing of hybrid Wind-PV system using Homer software in regions like Dhahran, Riyadh, Jeddah, Guriat and Nejran. Near optimal sizing of hybrid

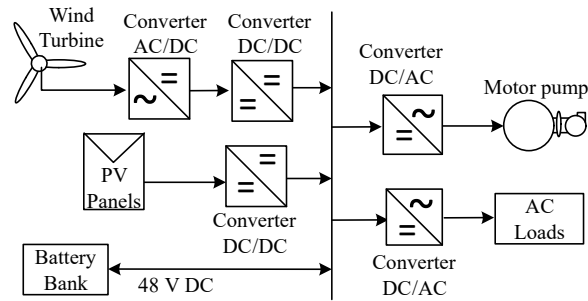


Figure 1.4: Block diagram of renewable energy hybrid power system for agricultural applications (Traoré et al., 2018)

Wind-PV system is reported to give constant pumped output throughout the year. However, over pumping is observed in spring and summer due to high sunlight and long days. Subsequently, (Parida et al., 2018), (Parida and Chatterjee, 2018) have implemented hybrid Wind-PV based AC and DC micro-grid with automatic power exchange facility. The system consists of two wind turbines, PV system, and battery storage feeding agricultural pumps and domestic loads as shown in Figure 1.5. The battery storage requirements are reported to be reduced due to the complimentary profile of wind and solar PV sources.

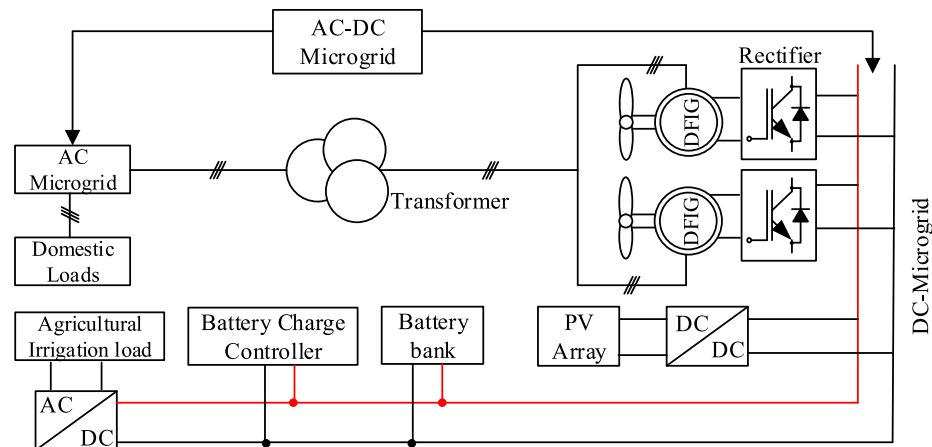


Figure 1.5: Hybrid Wind-PV based AC and DC micro-grid implementation (Parida et al., 2018)

A recent study by (Gholamshahi et al., 2019) has revealed interest in reducing part count in power electronics for water pumping using a three-phase induction motor. However, it is reported that the aforementioned system compromises the MPPT of the WECS. On this account, in few recent studies employing AC motor for WPS, the

MPPT from solar PV and WECS is typically ensured by using a dedicated power converter for power conditioning from either source and an additional converter to integrate power from these sources (Priyadarshi et al., 2020, Mezghani et al., 2020, Femi et al., 2021). Such systems require more power devices resulting in increased losses and system cost. This establishes need to investigate a hybrid Wind-PV WPS, which offers reduced part count while ensuring effective energy utilization from the renewables.

1.2.4.2 Stand-alone hybrid Wind-PV system feeding test loads

Authors (Malla and Bhende, 2014) have proposed a stand-alone, hybrid Wind-PV energy system feeding AC loads. The proposition employs five power converters for power processing and facilitates MPPT from both renewable sources. In addition to MPPT, DC-link voltage regulation is also performed to demonstrate satisfactory response for balanced and unbalanced loads. Next, (Rezkallah et al., 2018) have attempted to integrate distributed energy sources (solar PV and wind energy) at the DC bus. Two boost converters, dump load, battery charging/discharging circuit and VSI perform the power conditioning of the proposed system. Three control strategies are implemented for the stable and efficient operation of the system. The first two algorithms extract maximum power from the solar PV source and wind turbine. The third algorithm regulates the AC output voltage against changing weather conditions. The system is tested against sudden changes in load (non-linear and unbalanced load). Subsequently, a topological modification to (Rezkallah et al., 2018) is proposed in (Pradhan et al., 2019) by inclusion of machine side VSC in place of the boost converter. A composite sliding mode controller is employed to this machine side VSC exhibiting improved steady-state and dynamic performance for rural electrification. Lately, (Krishan and Suhag, 2020) have proposed novel control strategy focused towards energy storage while ensuring MPPT from both renewables and AC output voltage regulation. The proposition employs four power converters and is tested with satisfactory response for critical and non-critical loads.

Authors (Daniel and AmmasaiGounden, 2004) have presented a novel method of integration between solar PV and wind energy with minimal power electronics interface. The square wave inverter is used to integrate renewable energy sources. Successful operation of the proposed system is demonstrated against variations in irradiance and wind speed. Since a single converter is used for integration, DC-link

voltage regulation and maximum power extraction are not addressed using this topology. Further, an improvement to (Daniel and AmmasaiGounden, 2004) is suggested by (Prakash et al., 2016) including boost converter for DC-link voltage regulation. However, MPPT of both renewables is not achieved despite inclusion of an additional boost converter. Recently, a system identical to (Prakash et al., 2016) is investigated by (Nindra et al., 2019) with DFIG. The proposition is reported to offer solar PV MPPT and output voltage regulation while compromising on MPPT of WECS.

1.2.4.3 Observations

The complexity in hybrid Wind-PV systems increases due to the presence of multiple sources. Nevertheless, several studies have reported that the hybrid Wind-PV systems provide energy autonomy in a stand-alone application, overcoming limitations posed by the stochastic nature of solar PV and wind energy sources. Additionally, these systems lead to the reduction of energy storage requirements.

The details of the research discussed in stand-alone hybrid Wind-PV systems are summarized in Table 1.4, which illustrates the power electronic interfaces and control strategies employed for solar PV system, WECS and the load. The power electronic interface and related control strategies are chosen based on the type of the wind generator, type of the motor pump/load and the PCC between the sources and the load. While some researchers have focused on the MPPT of both renewables, few have shown consistent efforts to reduce the power converter count and or device count. However, in such systems with reduced power electronics interface, the MPPT of renewable energy source/s is compromised.

Table 1.4: Summary of Hybrid Wind-PV WPS

Ref.	Wind G. Load	Power Electronic Interface			Control Strategy for	
		Load Co.	WECS	SPVS	WECS	SPVS
1	AC G. DC motor pump	Buck-Boost C.	Rectifier	Buck-Boost C.	3 Energy management strategies	MPPT A. MPPT A.
2	AC G. DC motor pump	Multi-input DC-DC converter				
3	AC G. pump load	DC-AC Inverter				Not Specified
4	AC G. motorpump	VSI	Rectifier +DC-DC C.	DC-DC C.	3 Power management strategies	
5	SEIG IM pump	VSI	VSC	Boost C.	Vector Co.	Voltage Co. MPPT A.
6	PMSG IM pump	VSI	Cuk C. 1	Cuk C. 2	SPWM	MPPT A. MPPT A.
7	PMSG IM pump	VSI	Buck C. 1	Buck C. 2	SPWM	MPPT A. MPPT A.
8	PMSG AC loads	VSI	Rectifier+Boost C.	DC-DC C.	Voltage C.	MPPT A. MPPT A.
9	BLDCM AC loads	VSI	Rectifier+Boost C. 1	Boost C. 2	SVPWM	MPPT A. MPPT A.
10	PMSG AC loads	VSI 1	VSI 2	Boost C.	SVPWM	MPPT A. MPPT A.
11	PMSG AC loads	VSI	Rectifier + Boost C. 1	Boost C. 2	Voltage Co.	MPPT A. MPPT A.
12	SEIG R load		VSI		Conventional square wave drive	
13	SEIG AC loads		VSI	Boost C.	Voltage Co.	Voltage Co. Voltage Co.
14	DFIG AC load		VSI	Boost C.	Voltage Co.	Voltage Co. MPPT A.

Ref-Reference; G-Generator; Co-Control; C-Converter; A.-Algorithm

1. (Vick and Neal, 2012)
2. (de Oliveira Ferreira et al., 2020)
3. (Ma et al., 2014)
4. (Traoré et al., 2018)
5. (Gholamshahi et al., 2019)
6. (Priyadarshi et al., 2020)
7. (Mezghani et al., 2020)
8. (Malla and Bhende, 2014)
9. (Rezkaallah et al., 2018)
10. (Pradhan et al., 2019)
11. (Krishan and Suhag, 2020)
12. (Daniel and Amma-saiGounden, 2004)
13. (Prakash et al., 2016)
14. (Nindra et al., 2019)

1.3 Motivation

Based on the literature reviewed, it is apparent that significant work is done in multi-stage and single-stage SPWPS. However, there is scope for investigation in Wind WPS and hybrid Wind-PV WPS. Furthermore, these REWPS are likely to be operated in a stand-alone mode where efficiency, reliability and less/no maintenance become crucial. On this line, few important figures of merit that are to be considered for the development of REWPS are:

1. Maximum power extraction from renewable source/s.
2. Minimal power electronic interface.
3. Effectiveness of system controller and its implementation feasibility.
4. System robustness.

Given the aforementioned factors, to ensure superior performance of REWPS, it is critical to accomplish design with maximum power extraction from renewable source/s employing minimal power electronics interface. Additionally, effective and low-complex controls are highly desirable for deployment in remotely located standalone applications to reduce/eliminate frequent maintenance.

1.4 Problem Statement

The problem statement of the thesis is deduced from the motivation. The possibility of integration of solar PV with wind energy to provide a reliable power supply for uninterrupted water pumping capability is fast emerging. This instills need to investigate the behaviour of hybrid Wind-PV source, power electronic interface and motor pump in an integrated environment. Thus, the problem formulation of the research work carried out in this thesis is described as effective operation and control of standalone hybrid Wind-PV WPS ensuring maximum power extraction from both renewable sources employing reduced power converter count.

1.5 Research Objectives

The proposed system used to deliberate the objectives of the research work carried out is shown in Figure 1.6. The system consists of solar PV and wind energy as renewable sources of active power feeding induction motor pump. A three-phase squirrel cage induction machine is configured as SEIG to extract power from the wind turbine. The power electronic interface for integration and maximum power extraction from renewable energy sources includes a dc-dc boost converter and a bidirectional Voltage Source Converter (VSC). The composite controller controls the overall system employing a reduced sensor set.

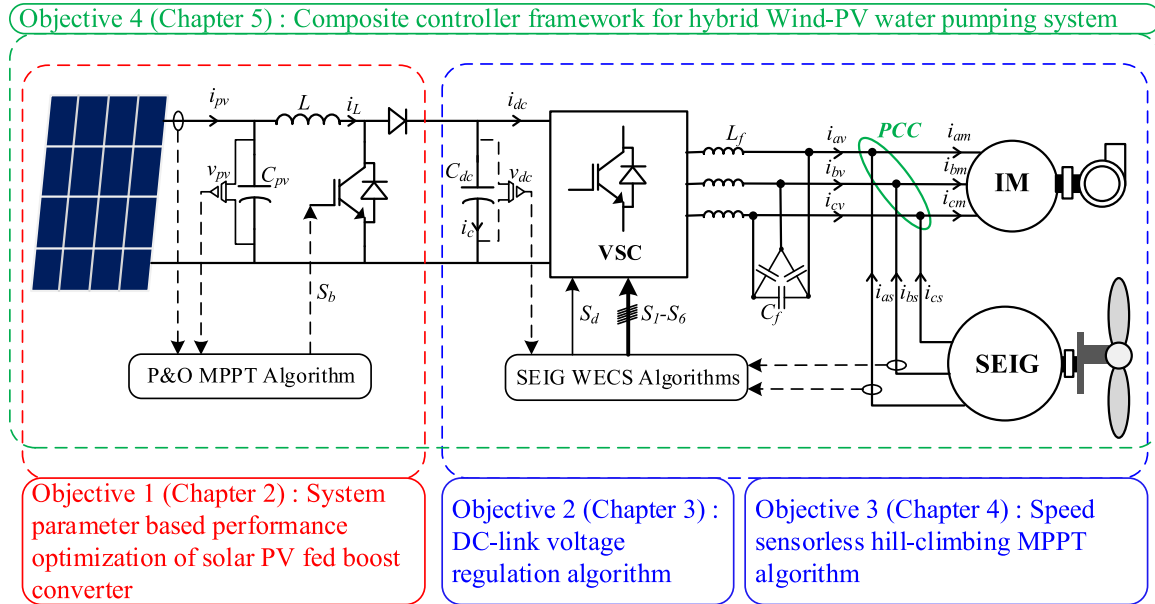


Figure 1.6: Proposed system description

Figure 1.6 also shows the breakdown of the formulated problem statement into the following objectives the thesis answers in subsequent chapters.

1. To study the factors influencing the system time constant and their effects on sampling time to improve the performance of the solar PV system with perturbation-based MPPT algorithm.
2. To develop and validate a DC-link voltage regulation scheme for SEIG-based WECS that employs only DC-link voltage information and facilitates a constant ‘V/F’ ratio at the Point of Common Coupling (PCC), thus avoiding saturation issues in the SEIG and the IM pump.

3. To propose and verify speed sensorless hill-climbing MPPT algorithm for SEIG based WECS employing minimal power electronic interface and reduced sensor set.
4. To propose and verify low-complex composite controller framework for hybrid Wind-PV WPS with minimal power electronic interface and reduced sensor set.

1.6 Organization of the Thesis

The work presented in this thesis is organized as follows:

Chapter 1: Presents the current trends in REWPS with a detailed literature review.

In addition, the formulated problem statement and the defined objectives are discussed. Finally, the organization of the thesis is provided in the last section of this chapter.

Chapter 2: In this chapter, a simple procedure to choose the optimal sampling time for a solar PV system with perturbation-based MPPT algorithm is suggested. The recommendations are made based on two simple step tests. In the process, the effect of system parameters, namely input capacitance, digital filter cut-off frequency and the system time constant on the choice of sampling time is examined. Comprehensive guidelines for choosing sampling time to ensure optimal performance are suggested based on simulation and test results.

Chapter 3: Presents a DC-link voltage regulation algorithm for SEIG-based WECS feeding an induction motor pump. The proposed algorithm ensures the constant flux operation of the SEIG and the IM pump by facilitating a constant ‘V/F’ ratio supply at the Point of Common Coupling (PCC). Viability of the proposed control strategy is verified by an extensive simulation study and experimental results obtained from a developed laboratory prototype.

Chapter 4: Proposes a speed sensorless hill-climbing algorithm for SEIG-based WECS feeding an induction motor pump. A detailed simulation study of this algorithm is performed and the findings are verified using test results. Finally, a qualitative comparison study with other available wind

MPPT algorithms is performed to justify the suitability of the algorithm for a stand-alone application.

Chapter 5: Proposes a stand-alone hybrid Wind-PV WPS with a minimal power electronics interface, simple composite controls, and an optimal energy management strategy to utilize renewable sources effectively. The operability of the proposed low-complex controller is validated using extensive simulation and experimental study. Further, a comparative study is performed with the recently developed hybrid Wind-PV WPS to justify the proposal's suitability for a stand-alone application.

Chapter 6: Summarizes the conclusions of Chapter 2 through 5 and suggest pointers for further research in this field.

Appendix A: Presents the details of the system attributes used for simulation and experimental verification of contributions in Chapters 2 through 5, consisting of data pertaining to the solar PV array, electrical machines, and the wind turbine.

Appendix B: Describes the experimental setup of the standalone solar PV system, SEIG-based Wind Energy Conversion System (WECS) and hybrid Wind-PV WPS used to obtain test results of all investigations carried out in this research work. Additionally, a Model Based Design (MBD) workflow using Altair Embed and TMS320F28069M target hardware is presented, which is employed to develop all control schemes for research work carried out in this thesis.

Chapter 2

Maximum Power Point Tracking of Solar PV System

2.1 Introduction

This chapter introduces a solar PV fed boost converter as an elementary part of a hybrid Wind-PV WPS. As the solar PV array exhibits non-linear power characteristics, Maximum Power Point Tracking (MPPT) algorithms are imperative in such systems. Of all the MPPT schemes, perturbation-based MPPT techniques are popular due to their simplicity and reasonable efficiency. While novel MPPT algorithms claim increased energy utilization over classic perturbation techniques, their performance is governed by optimal algorithm parameters like sampling time and perturbation size.

Several investigations are carried out to study the effect of T_s and perturbation step size (ΔD) on system performance. A theoretical analysis guiding the optimal choice of T_s and ΔD using small-signal modeling is carried out by (Femia et al., 2005, 2009). Subsequently, a focused research on choice of optimal T_s is rendered by (Kivimäki et al., 2017a,b) using step-response of small-signal model. All the investigations mentioned above are mathematically laborious and are not generic.

Hence, a generic and empirical formulation for the choice of optimal sampling time is proposed in this chapter, eluding the small-signal model. In this regard, a solar PV fed boost converter is investigated to examine the effect of input capacitor, digital filter cut-off frequency, system time constant and sampling time (T_s) on implementing a Perturb and Observe (P&O) algorithm. Further, two simple step tests (to determine

the effective system time constant) and proposed guidelines are presented to choose the optimal performance T_s . Test results reveal that an appropriate choice of T_s using suggested guidelines could increase efficiency and ensure system stability.

2.2 System Description

The circuit schematic of solar PV fed boost converter is shown in Figure 2.1. It consists of a solar PV array, boost converter feeding resistive load and the system controller. A P&O algorithm with direct duty ratio perturbation is adopted to ensure maximum power transfer from the source to the load. For simulation studies, the required v_{pv} and i_{pv} are sampled and are processed using P&O algorithm to generate appropriate duty ratio (D). In case of experimentation, the required signals are read using inbuilt ADC of the controller. Further, a digital filter is employed to eliminate high-frequency noise before the signals are fed to the P&O algorithm. The important system parameters considered for investigation in this study affecting the performance of the system are highlighted in Figure 2.1.

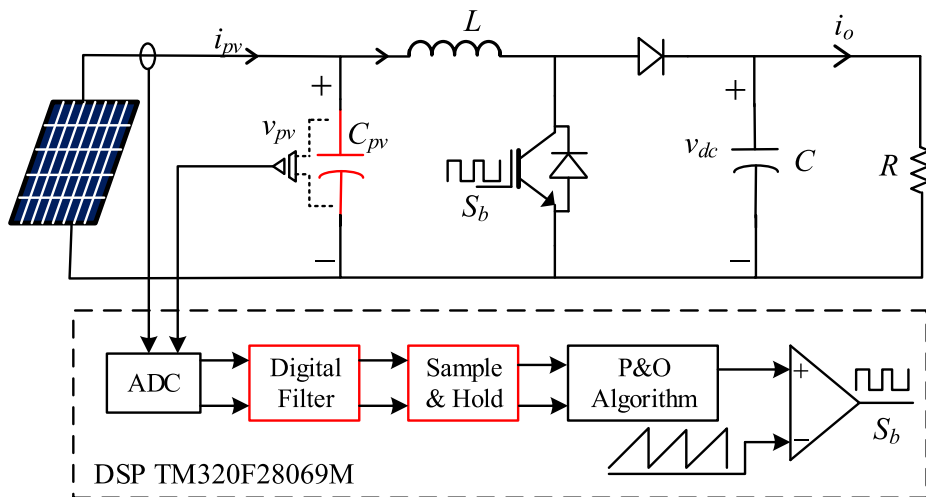


Figure 2.1: Circuit diagram of solar photovoltaic (PV) fed boost converter and system controller

2.3 Effects of System parameters on System Time Constant

The input capacitance and the digital filter cut-off frequency play a significant role in deciding the settling time of PV voltage (v_{pv}) and PV current (i_{pv}), which in turn influence the choice of the sampling time. The effect of these system parameters on the performance of solar PV systems is discussed in this section.

2.3.1 Input Capacitance

The switching frequency (F_{sb}) of the boost converter used in this study is 10 kHz. This F_{sb} introduces transients in all currents and voltages of the converter. In a boost converter based PV system, the ripple in inductor current influences the ripple in v_{pv} and i_{pv} . This ripple leads to reduction of the average values of solar PV voltage v_{pv} , current i_{pv} and hence P_{pv} . The inclusion of input capacitance (C_{pv}) helps in reducing this ripple content considerably. This C_{pv} , by definition is given by

$$C_{pv} = \frac{Q}{v_{pv}} = \frac{t \times (i_{pv} - i_L)}{v_{pv}}. \quad (2.1)$$

It is imperative from equation 2.1 that for a given operating point on PV curve, the values of i_{pv} and v_{pv} remain unchanged and the time (t) taken for charging and discharging of capacitor varies directly depending on the value of C_{pv} . Hence the settling time of the responses of v_{pv} and i_{pv} increase with increase in C_{pv} and vice versa.

2.3.2 Digital Filter Cut-off frequency

The switching frequency of the boost converter and the process of analog to digital conversion of v_{pv} and i_{pv} results in high-frequency noise in these signals. This noise, if untreated, leads to reduced efficiency of the PV system or system instability due to increased perturbations. The use of digital filters in experimental studies is imperative due to the presence of the high-frequency noise added during ADC sampling. Literature suggests that the first-order low-pass filter described by equation 2.2 is adequate to filter the high-frequency noise (Al-Atrash et al., 2010).

$$\frac{H_0(s)}{H_i(s)} = \frac{\omega_c}{\omega_c + s}, \quad (2.2)$$

where ω_c is the cut-off frequency of the filter in electrical rad/sec.

$$H_{0\mu} = \frac{\omega_c}{\sqrt{\omega^2 + \omega_c^2}} \quad (2.3)$$

$$H_{\text{delay}} = \frac{1}{\omega_c}. \quad (2.4)$$

In this study, a first-order low-pass filter is designed in continuous time domain and its digital coefficients are obtained using the bilinear transformation. This filter results in attenuation ($H_{0\mu}$) and additional delay of the signals given by equations 2.3 and 2.4, respectively. The attenuation caused by this filter is negligible; however, the delay caused by the filter significantly influences the performance of the MPPT algorithm if the cut-off frequency is not chosen judiciously.

2.3.3 Sampling time

The sampling time (T_s), also referred to as perturbation frequency, largely governs the speed and efficiency of the MPPT algorithm. If the T_s is less than the required value, it leads to reduced efficiency and, in the worst case, may cause system instability. On the contrary, if the chosen T_s is more than required, it results in a sluggish algorithm response for fast varying irradiation. Hence the informed choice of T_s is inevitable to ensure optimal speed and stability of perturbation-based MPPT algorithms.

2.4 Mathematical Modeling

In this section, the mathematical modelling of the solar PV fed boost converter is presented. Figure 2.2 shows the equivalent circuit of the system under test. The PV array is modelled using single diode model (Villalva et al., 2009). The boost converter is modelled using the concept of switching function. The input capacitance (C_{pv}) present between PV array and the boost converter is modeled as extended part of PV module modelling.

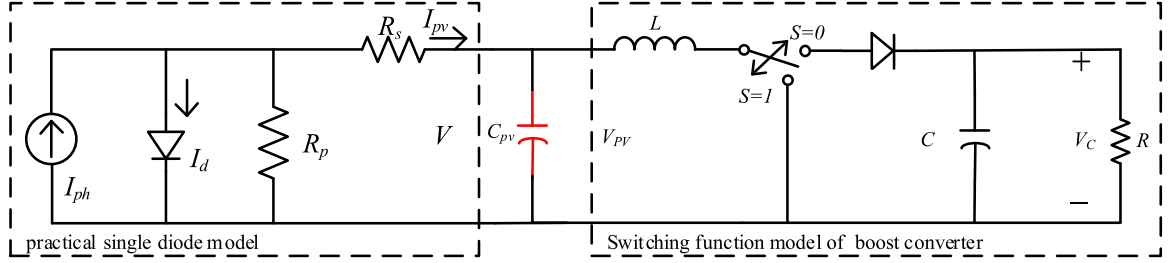


Figure 2.2: Equivalent circuit of single diode model of solar PV cell and boost converter using switching function

2.4.1 Solar PV array

The current available at terminals of PV cell (i_{pv}) is governed by internal (series and parallel resistance of PV cell) and external factors (solar irradiance, temperature) (Villalva et al., 2009). Employing KCL, i_{pv} is represented as,

$$i_{pv} = i_{ph} - i_0 \left(e^{\frac{V+R_s I}{aV_T}} - 1 \right) - \frac{v_{pv} + R_s i_{pv}}{R_p}. \quad (2.5)$$

The current generated by light (i_{ph}) is dependent on solar irradiance and temperature given as,

$$i_{ph} = (i_{ph,n} + K_I \delta_T) \frac{G}{G_n}. \quad (2.6)$$

The diode saturation current (i_0) is dependent on the ambient temperature T_c given as,

$$i_0 = \left[\frac{i_{SC,n}}{\exp\left(\frac{V_{OC,n}}{aV_{t,n}}\right) - 1} \right] \left(\frac{T_n}{T_c} \right)^3 \exp \left[\frac{qE_g}{ak} \left(\frac{1}{T_n} - \frac{1}{T_c} \right) \right]. \quad (2.7)$$

2.4.2 Boost Converter

The boost converter is expressed using equations 2.8 and 2.9 employing concept of switching function (S).

$$\frac{di_L}{dt} = \frac{v_{pv} - S.v_0}{L} \quad (2.8)$$

$$\frac{dv_{dc}}{dt} = \frac{S.i_L - \frac{v_0}{R}}{C_{dc}}. \quad (2.9)$$

A capacitor used at the output of the PV cell is used to derive the PV voltage

(v_{pv}) given as,

$$v_{pv} = \frac{1}{C_{pv}} \int (i_{pv} - i_L) dt. \quad (2.10)$$

2.5 Proposed Tests and Guidelines for System Parameter Based Performance Optimization

In this section, the details of the proposed tests and the guidelines for optimal solar PV system performance with a perturbation-based MPPT algorithm is discussed. Also, preliminary test results and their inferences are presented to support the hypothesis. The system parameters used for simulation and experimental studies are taken of commercial 50 W PV module and are listed in Table A.1.

2.5.1 Step Test 01—Optimum Value Input Capacitance

To restrict the effect of harmonics induced by virtue of high switching frequency in boost converter, an input capacitor (C_{pv}) is connected across the PV array and is calculated using equation 2.11, (Ayop and Tan, 2018)

$$C_{pv} = \frac{T(\Delta i_L)}{8(\Delta v_{pv})}, \quad (2.11)$$

where

$$\Delta i_L \text{ (inductor current ripple)} = 30\% \text{ of } i_{pv} = 0.3 \times 2.94 = 0.882$$

$$\Delta v_{pv} = 0.1\% \text{ of } v_{pv} = 0.001 \times 85 = 0.085$$

$T = 1/F_{sb}$, F_{sb} being the switching frequency of Boost converter.

The value of C_{pv} calculated using above parameters and equation 2.11 is $130 \mu F$. In this study, $C_{pv} = 220 \mu F$ is chosen for simulation and experimental investigations to account for non-idealities, ADC noise and for factor of safety. The expression for C_{pv} described in equation 2.11 varies with the chosen power converter. However, the aforementioned exercise is essential to avoid unnecessary selection of large value of input capacitance.

A simple test (Step test-01) is performed to determine the approximate system time constant (τ_1) of system under consideration for different values of C_{pv} .

Step test 01: Following are the sequence of steps involved in carrying out the test.

1. Configure an experimental setup consisting of Solar PV array, C_{pv} and the power converter under test (setup is shown in Figure 2.1 for this study)
2. Choose appropriate value of C_{pv} and vary the duty ratio from minimum to maximum value and capture the responses of v_{pv} and i_{pv} . (In this study, $C_{pv} = 220 \mu F$ is chosen and D is varied from 0.1 to 0.7 in steps of 0.05)
3. Repeat step 2 for different values of C_{pv} , to see the effect of input capacitance on τ_1 . (In this study, responses are investigated for $C_{pv} = 220 \mu F$, $440 \mu F$ and $660 \mu F$).

Figures 2.3 (a) and (b) show the behaviour of the settling time of v_{pv} and i_{pv} respectively, recorded for step changes in duty ratio for three different C_{pv} values. The τ_1 is dependent on the value of C_{pv} of the system.

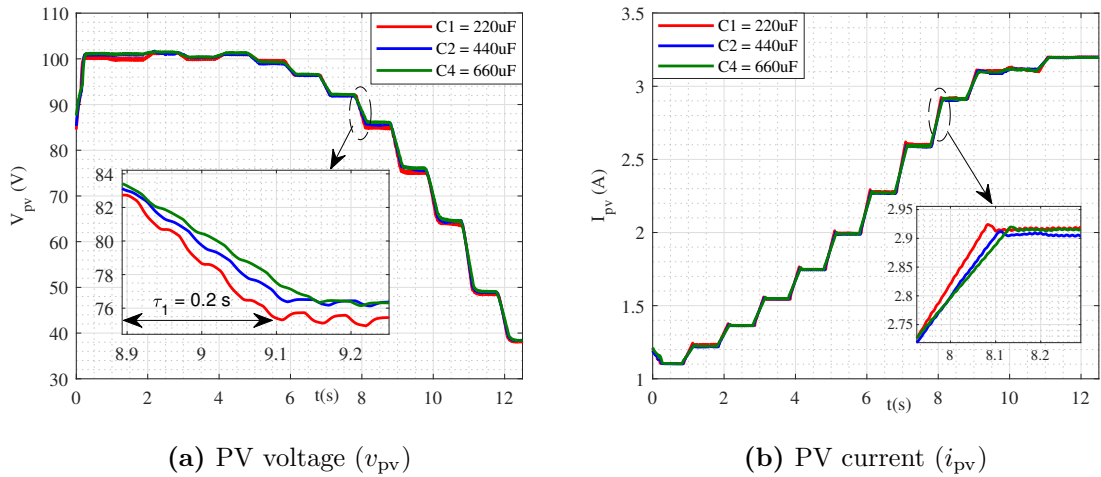


Figure 2.3: Experimental results: Step response of PV voltage and current for different values of input capacitance (C_{pv})

Following inferences are made based on equation 2.11 and the results of Step test 01 conducted on the system:

1. The value of C_{pv} depends on the switching frequency of the power converter, ripple in PV voltage and PV current and is calculated using equation 2.11.

2. The value of C_{pv} is directly proportional to the settling time of responses of PV voltage and current.
3. The τ_1 of the system is **0.2 s** for $C_{pv} = 220\mu F$.

The value of τ_1 increases with increase in (C_{pv}) and vice versa. The τ_1 recorded should be considered as an approximate system time constant. Another simple step test (Step test 02) helps to estimate additional delay and attenuation caused by the digital filter and determine effective system time constant (τ_2) as seen by the controller.

2.5.2 Step Test 02—Optimum Digital Filter Cut-Off Frequency (ω_c)

The precision of voltage and current measurements are crucial in perturbation based MPPT algorithms. Filters are invariably employed to reduce the noise in sensed variables. Recently, digital filters for noise filtering are fast emerging. The performance of the chosen filter is predominantly decided by the cut-off frequency. If the cut-off frequency of the filter is arbitrarily chosen to over-filter noise, then it will result in undesired addition of delay, which will further make the system sluggish. To demonstrate the undesired addition of delay caused by the inclusion of filters, another simple step-test (step test - 02) is performed. This test helps in determining the effective system time constant (τ_2) as seen by the controller.

Step test 02: Following are the sequence of steps involved in carrying out the test.

1. Configure experiment set-up with chosen value of C_{pv} in step test-01. ($C_{pv} = 220 \mu F$)
2. Configure digital filter to eliminate/reduce the noise due to ADC. (First order filter with cut-off frequency of 157 rad/s, 314 rad/sec and 628 rad/s are used in this study, first cut-off frequency (100 Hz = 628 rad/s) is empirically chosen as 0.01 times switching frequency (10 kHz))
3. Introduce a step change in D of switch (S_b) and record the response of digital filter output (v_{pv}) for different cut-off frequencies. (During experimentation,

the response of v_{pv} was observed to be slightly slower compared to i_{pv} , hence v_{pv} was chosen as criteria over i_{pv})

In addition to the system time constant, the digital filter introduces additional delay based on the chosen cut-off frequency. Figure 2.4 reveals the effect of reducing the cut-off frequency of the digital filter. It is evident from the waveform that the delay introduced by the filter increases as the cut-off frequency is reduced. This delay introduced by filter into the signal will further increase the settling time of the sensed variables. Hence, the settling time of the v_{pv} and i_{pv} should be calculated after they are subjected to the filter. Also, it is recommended that the same digital filter be used to filter noise from v_{pv} and i_{pv} to maintain uniform delay and attenuation. This will ensure appropriate decision making by P&O algorithm.

A low-pass digital filter with cut-off frequency of 628 rad/s (100 Hz) is employed in the present experimental studies resulting in effective time constant of **0.25 s** (τ_2) as seen from the controller. It is to be noted that τ_2 represents the cumulative delay (system time constant (τ_1) + digital filter delay) not the delay caused by digital filter alone.

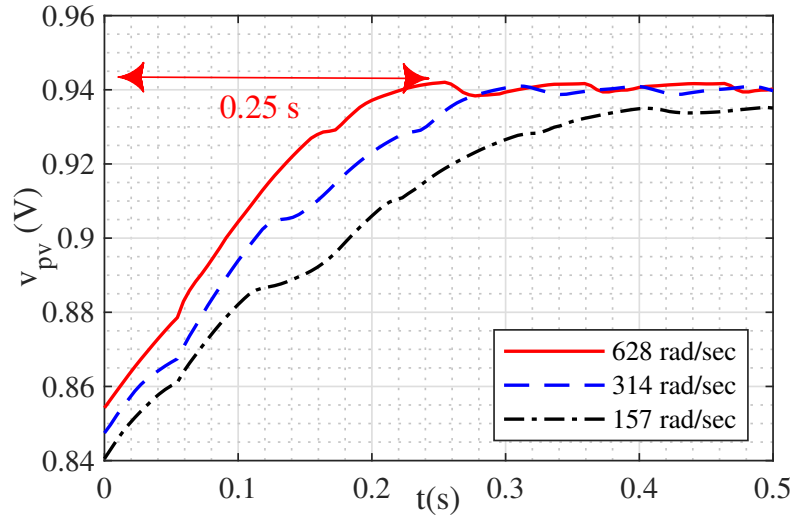


Figure 2.4: Experimental results: Step response of PV voltage (in p.u) for different cut-off frequencies of first order digital filter

2.5.3 Proposed Guidelines for the Choice of Sampling Time

The values of the τ_1 and τ_2 are obtained using two tests discussed in Sections 2.5.1 and 2.5.2 respectively. A simple procedure for the choice of T_s is recommended using this data to ensure optimal performance of perturbation based MPPT algorithms. The following are the suggested guidelines for the choice of T_s .

1. For a given switching frequency F_{sb} , obtain the value of C_{pv} using equation 2.11 ($C_{pv} = 220 \text{ uF}$).
2. Conduct step test for system under test using control variable (D , in this case) and determine the τ_1 of the system under test ($\tau_1 = 0.2 \text{ s}$).
3. Determine the effective delay (τ_2) introduced in the sensed variables (v_{pv} and i_{pv}), including that of the digital filter delay for chosen cut-off frequency. ($\tau_2 = 0.25 \text{ s}$)
4. Select sampling time for perturbation based algorithm (T_s) more than (τ_2), ($T_s = K\tau_2$) approximately. where $K = 1.5$ is empirically chosen.
 - (a) Experiments are conducted for four different T_s (0.5 s, 0.4 s, 0.3 s, 0.2 s)
 - (b) Behaviour of D , v_{pv} , i_{pv} and P_{pv} are presented for $T_s = 0.4s$ ($T_s > 1.5\tau_2$) and $T_s = 0.3s$ ($T_s < 1.5\tau_2$).
 - (c) Average PV power extraction is discussed for all four sampling times.
5. Energize the system under test with suitable perturbation based algorithm and chosen T_s , and observe the behavior of control variable (D) and system variables (v_{pv} and i_{pv}) to exhibit sustained three-step and quasi three-step waveforms respectively, around their respective steady-state values.
6. The T_s can further be optimized by adjusting 'K', based on the required tracking speed and the energy extraction.
7. Check the behaviour of control variable and the system variables for step-change in irradiance to ensure three-step and quasi three-step waveforms respectively.

It is noteworthy that the proposed tests and guidelines are comprehensive. These tests and guidelines can be easily extended to any power converter and perturbation based MPPT algorithm for performance improvement.

2.6 Simulation and Experimental Study

The simulation and experimental studies are performed on 250 W solar PV array configured by series connection of five solar PV modules. The attributes of solar PV module used for simulation and solar PV profile emulation are described in Table A.1.

2.6.1 Simulation Results

The mathematical model of the solar PV fed boost converter discussed in section 2.4 is implemented using MATLAB/Simulink and corresponding results are presented in this section. After the choice of suitable C_{pv} , the results are captured for two different sampling times and irradiance. The data used for simulation is listed in Table A.1. The expected steady-state values of the system variables for two different solar irradiance are as shown in Table 2.1. The steady-state value of D in Table 2.1 is obtained using equation 2.12 (Fannakh et al., 2018).

$$D = 1 - \sqrt{\frac{R_{mp}}{R}}. \quad (2.12)$$

Table 2.1: Steady state values of system variables

G (W/m^2)	V_{mp} (V)	I_{mp} (A)	R_{mp} (Ω)	P_{mp} (W)	D_{mp}
800	86.14	2.331	36.95	200	0.45
1000	85.63	2.91	29.42	250	0.5

The performance of the system is studied by analyzing system variables namely D , i_{pv} , v_{pv} and P_{pv} for step change in solar irradiance (G) from 800 W/m^2 to 1000 W/m^2 . The variables are captured for T_s of 0.4 s and 0.1 s shown in Figures 2.5 and 2.6 respectively. Initial value of D is set to 0.5 to shorten the tracking time during startup of the system.

Figure 2.5 (a) shows the variation of D for step change in G . The response settles in 1.5 s exhibiting a three step perturbation for $G = 800$ W/m^2 . Further, a step change in G is introduced at $t = 7.5$ s, D settles to D_{mp} with three step response in less than 2 s. The overall response in Figure 2.5 (a) proves the logical correctness of the P&O algorithm. However, the optimal performance of the algorithm depends

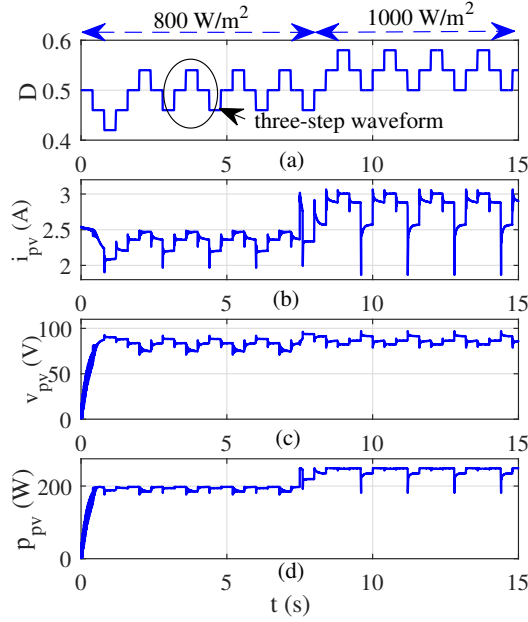


Figure 2.5: Simulation results: (a) Duty ratio, (b) PV current, (c) PV voltage and (d) PV power with sampling time of 0.4 s

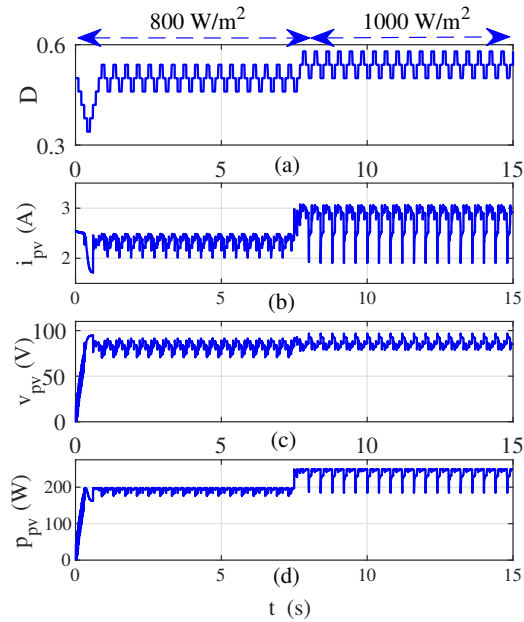


Figure 2.6: Simulation results: (a) Duty ratio, (b) PV current, (c) PV voltage and (d) PV power with sampling time of 0.1 s

on the appropriate choice of T_s . Figure 2.5 (b) - (d) shows the response of v_{pv} , i_{pv} and p_{pv} . All three variables exhibit three-step waveform around steady-state values indicated in Table 2.1 for step change in G .

Results for a T_s of 0.1 s are shown in Figure 2.6. In Figure 2.6 (a), D exhibits stable three-step variation around the steady-state value. However, a disturbance is observed in i_{pv} and v_{pv} for every duty ratio perturbation resulting in increased disturbance in P_{pv} . For every change in D , the operating point changes and require v_{pv} and i_{pv} to settle at new steady-state values. Variables v_{pv} and i_{pv} undergo transients for the time defined by the system time constant before they settle at steady-state values. If the consequent change in D results before the responses of v_{pv} and i_{pv} have settled, then the resulting v_{pv} and i_{pv} will exhibit disturbance. Lesser the value of T_s more severe is the disturbance. The effect of this disturbance is not significant in simulation studies due to absence of non-idealities and ADC process. However, it becomes critical in experimental studies as disturbances in v_{pv} and i_{pv} cause cumulative disturbance in P_{pv} , adversely affecting the power extraction.

2.6.2 Experimental Results

The details of the experimental setup used to obtain test results are presented in section B.1. Unlike the simulation model, the experimental setup consists of non-idealities viz. inductor resistance, capacitor resistance, switch resistance and switch stray capacitance. Additionally, i_{pv} and v_{pv} are to be read via ADC for algorithm processing. During this conversion, the signals are prone to disturbance due to the added noise during sampling process. Hence, the values of T_s for same value of input capacitance may change in comparison to simulation studies. Figures 2.7 and 2.8 shows the response of D , i_{pv} and v_{pv} for step change in G from 800 W/m^2 to 1000 W/m^2 for a T_s of 0.4 s and 0.3 s respectively.

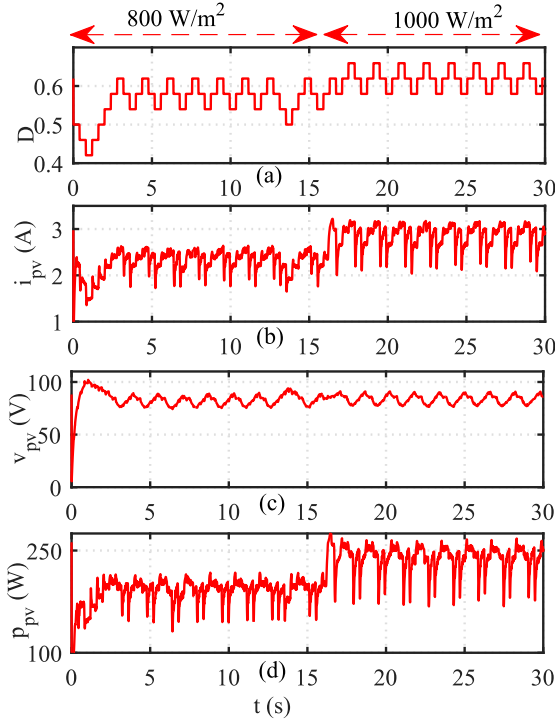


Figure 2.7: Experimental results: (a) Duty ratio, (b) PV current, (c) PV voltage and (d) PV power with sample time of 0.4 s

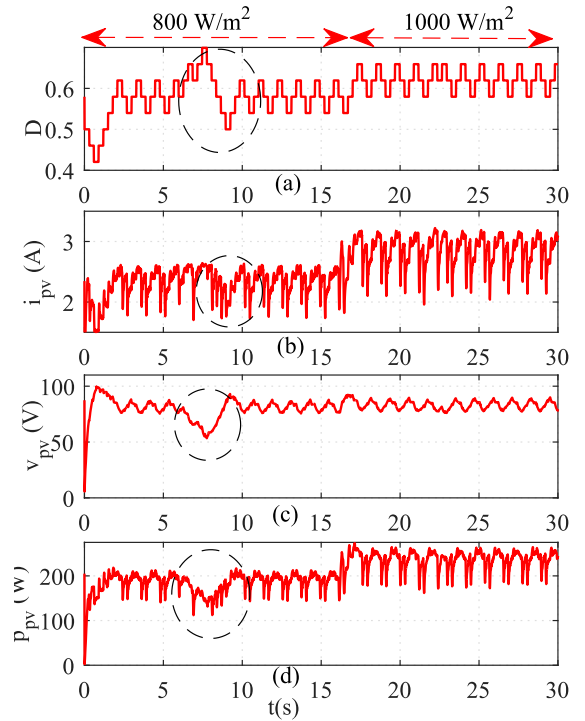


Figure 2.8: Experimental results: (a) Duty ratio, (b) PV current, (c) PV voltage and (d) PV power with sample time of 0.3 s

The behaviour of D , v_{pv} , i_{pv} and P_{pv} for T_s of 0.4 s is captured in Figure 2.7 (a)-(d). The control variable, D exhibits perfect three-step oscillation around steady-state value. For every change in D , i_{pv} and v_{pv} exhibit quasi three-step variation. This can be attributed to presence of non-idealities in experimentation.

Hence, the quasi three-step waveforms for i_{pv} and v_{pv} is considered satisfactory. Further increase in T_s to achieve precise three-step waveform results in sluggish response. The P_{pv} follows the variations in v_{pv} and i_{pv} and oscillates around anticipated steady state value. The chosen sampling time ($T_s = 0.4$ s) ensures fast tracking and stable steady state operation for step change in G yielding optimal performance.

Figure 2.8 shows the response of D , v_{pv} , i_{pv} and P_{pv} for T_s of 0.3 s. It is evident that the noise in i_{pv} and v_{pv} is confusing the P&O algorithm. The confusion is mainly due to reduced T_s , which is insufficient for the responses to settle for perturbations in D . Figure 2.8 (a) shows the response of D exhibiting three-step waveform with two wrong decisions by the P&O algorithm highlighted in Figure 2.8 (a). The responses of i_{pv} and v_{pv} for perturbations in D are shown in Figure 2.8 (b), (c) respectively. It is evident that i_{pv} and v_{pv} though oscillating around steady-state value, exhibit increased disturbances. The P_{pv} further exhibits the cumulative effect of these disturbances as shown in Figure 2.8 (d) leading to reduced energy extraction.

To demonstrate the significance of the T_s in experimentation, tests are conducted for four different T_s viz. 0.5 s, 0.4 s, 0.3 s and 0.2 s and the average power extraction is captured in Figure 2.9. Additionally, the MPPT efficiency as recorded by Magna solar emulator is shown in Table 2.2. Contemplating average power plots and the steady state efficiencies for different sampling times, $T_s = 0.4$ s is suggested to be optimal sampling time owing to reasonable transient response and steady-state efficiency. It is evident from Figure 2.9 that $T_s > 0.4$ s increases the tracking time, while $T_s < 0.4$ s results in reducing efficiency or in worst case lead to system instability. Choice of T_s is trade-off between the tracking speed and stability margin. Hence, judicious choice of T_s is crucial for optimal performance of solar PV system with perturbation based MPPT algorithm.

Table 2.2: Steady-state efficiency of P&O algorithm recorded for different sampling times (Power read back accuracy of $\pm 0.28\%$ recorded using Magna Solar Emulator SL300-5/85-265)

Sampling time T_s (s)	Efficiency (%)
0.5	97.2
0.4	94.9
0.3	91
0.2	84

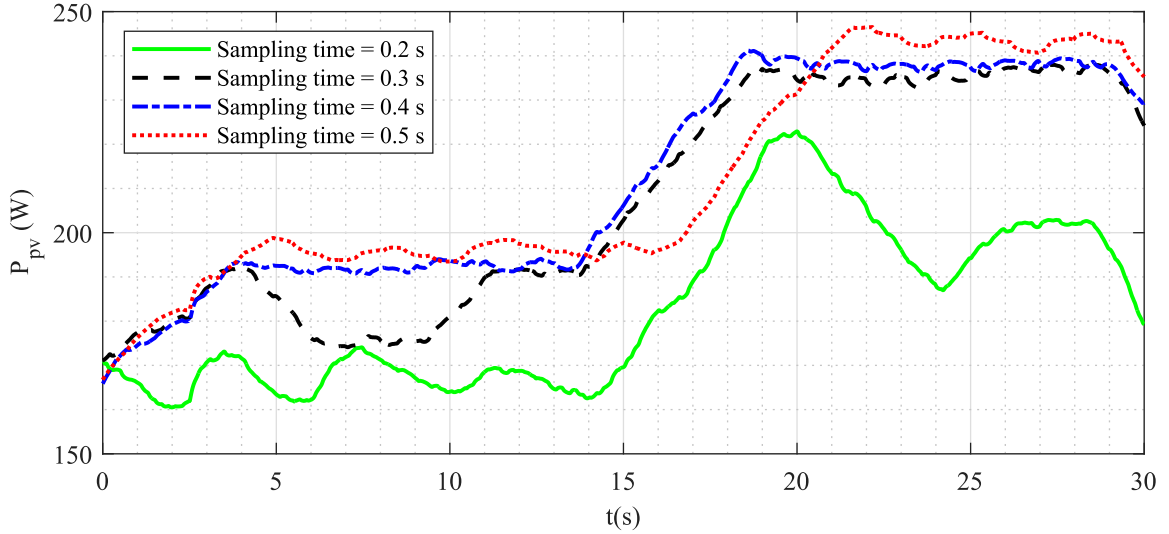


Figure 2.9: PV power for different sampling times (Power read back accuracy of $\pm 0.28\%$ recorded using Magna Solar Emulator SL300-5/85-265)

2.7 Comparative Analysis

The comparison of theoretical, simulation and experimental studies is summarized in Table 2.3. It is evident that, the simulation results are in close agreement with theoretical values compared to experimental results. The findings of this study suggest that the experiment results are more susceptible to T_s due to the existence of non-idealities and ADC conversion. Hence, even the smallest change in T_s results in a significant shift in power extraction and stability margin.

Table 2.3: Steady state values of system variables for theoretical, simulation and experimental studies ($T_s = 0.4$ s)

Parameters	G (W/m^2)	V_{mp} (V)	I_{mp} (A)	R_{mp} (Ω)	P_{mp} (W)	D_{mp}
Theoretical results	800	86.14	2.331	36.95	200	0.45
	1000	85.63	2.91	29.42	250	0.5
Simulation results	800	82.7	2.35	35.19	194	0.5
	1000	87.5	2.81	31.13	245.875	0.54
Experimental results $T_s = 0.4s$	800	82.15	2.27	35.24	186.48	0.58
	1000	83.46	2.843	30.12	237.27	0.62

Decisively, a comparison of the proposed method for selecting T_s is presented in Table 2.4. The time constant of the system is obtained using a simple step test

(step test 01) in this work, compared to the mathematically intensive small signal based approach (Femia et al., 2005, 2009, Elgendy et al., 2011, 2012, Kivimäki et al., 2017a,b) and DCD-RLS approach (Dadkhah and Niroomand, 2018). The inclusion of a digital filter adds a delay to the sensed variables. This critical consideration of additional delay is estimated in this study using another step-test (step-test 02), which is seen to be neglected in (Femia et al., 2005, 2009) (Kivimäki et al., 2017a, Dadkhah and Niroomand, 2018).

Table 2.4: Comparison of methods for choice of sampling time in solar photovoltaic systems

Parameters \ Ref	1	2	3	4	Proposed
System time constant	SSM (τ)	SSM	SSM (τ)	DCD-RLS(τ)	Step test -01 (τ_1)
Digital Filter delay	Neglected	100 Hz (0.01 s)	Neglected	Neglected	Step-test - 02 (τ_2)
T_s	$1.1 \times \tau$	Trial and error	τ	τ	$1.5\tau_2$
Comprehensiveness	No	No	No	No	Yes

Note:—SSM: Small-signal model, DCD-RLS: dichotomous coordinate descent-recursive least squares (a parameter identification technique), τ = Settling time of solar PV system, τ_1 = System time constant in present study, τ_2 = Effective system time constant in present study considering digital filter delay.

1. (Femia et al., 2005, 2009)
2. (Elgendy et al., 2011, 2012)
3. (Kivimäki et al., 2017a,b)
4. (Dadkhah and Niroomand, 2018)

It is worth noting that the tests discussed in Sections 2.5.1 and 2.5.2 are comprehensive and can be performed on any given power converter and load to obtain τ_1 and τ_2 . Further the guidelines proposed in Section 2.5.3 can be employed to chose optimal T_s for performance optimization.

Chapter 3

Voltage Regulation Algorithm for SEIG Based WECS

3.1 Introduction

In the previous chapter, a solar PV fed boost converter with a perturbation based MPPT algorithm is investigated to ensure optimal performance. This chapter introduces SEIG-based WECS as a subsequent part of the hybrid Wind PV WPS. As the system suggests, the DC-link capacitor of the VSC to cater to reactive power of the SEIG and the IM pump, its voltage regulation becomes crucial. In this regard, a DC-link Voltage Regulation (VR) algorithm for VSC assisted SEIG-based WECS feeding IM pump is proposed in this chapter. In addition to voltage regulation, the developed control scheme facilitates a constant ‘V/F’ ratio of the supply at the PCC, resulting in the constant flux operation of the SEIG and the IM pump for varying wind velocities. The developed control scheme employs a single voltage sensor for algorithm processing, making the proposition speed sensorless and cost-effective.

In this chapter, the mathematical model of the wind turbine, the SEIG with saturation effects, power electronic interface and the IM pump are presented in detail. Extensive simulation and experimental results are presented to prove the viability of the DC-link VR algorithm against wind velocity and load variations.

3.2 System Description

The system configuration of wind turbine driven, VSC assisted, SEIG feeding IM pump is shown in Figure 3.1. The variable speed wind turbine characteristics are emulated via armature current control of a separately excited DC motor that transfers mechanical power to the SEIG. A DC-link capacitor fulfills the reactive power requirement of the SEIG via VSC, which facilitates bidirectional power flow. Initial voltage for DC-link capacitor is made available using a 12 V battery which meets the reactive power requirement of the SEIG during starting. Once the generation is sustained, the reactive power demand of the SEIG is fulfilled by the charged DC-link capacitor. A three-phase IM pump load is inserted as an active load on the SEIG. The system controller acquires only DC-link voltage information to regulate the DC-link voltage against varying wind velocities and load. To protect the system against light load or no load, a dump load with Electronic Load Control (ELC) is operated in parallel with a DC-link capacitor.

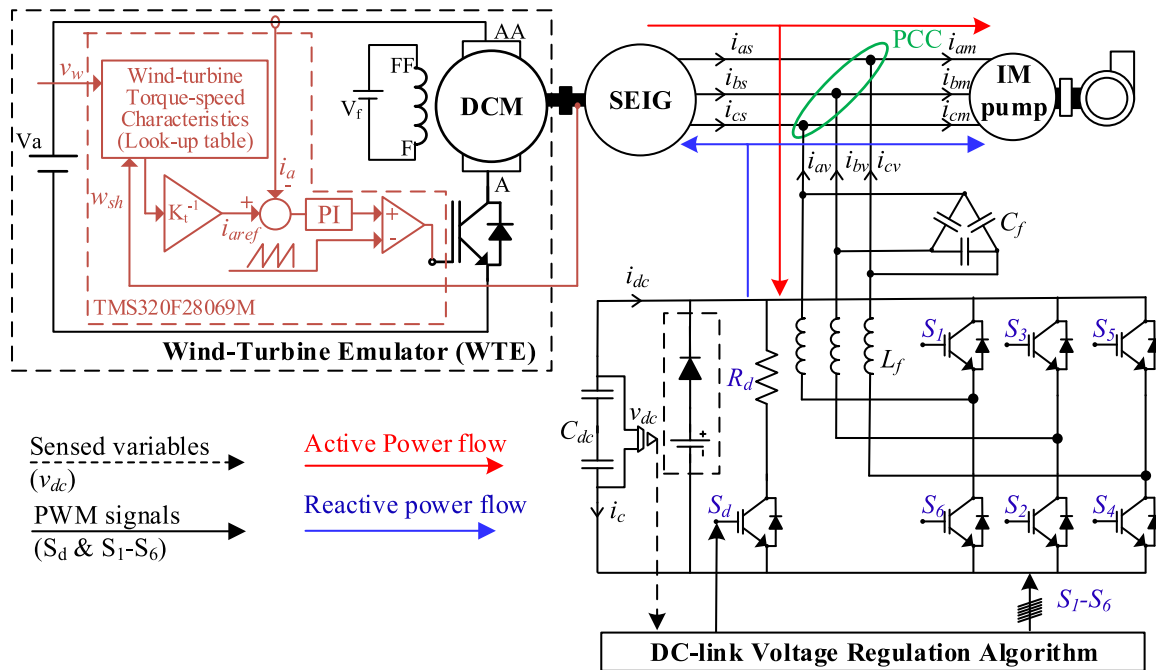


Figure 3.1: Circuit diagram of the wind turbine driven, VSC assisted SEIG feeding IM pump with DC-link voltage regulation algorithm

The VSC, the SEIG and the IM pump are connected in parallel, forming PCC at the AC terminals. The stator windings of the SEIG and the IM pump are connected

in delta and are tied to the same frequency and voltage as decided by the VSC. A simple LC line filter is employed at the VSC line terminals to convert the steep pulsed line voltages to quasi-sinusoidal waveforms, reducing the ‘dV/dt’ stress for both the machines connected at the PCC. In the system under consideration, the SEIG and the DC-link capacitor are the sources of active and reactive power respectively and the active/reactive power flow in the system is as indicated in Figure 3.1.

3.3 Mathematical Modeling

In this section, detailed mathematical model of wind-turbine driven, VSC assisted SEIG feeding IM pump is described.

3.3.1 Wind-Turbine Characteristics

Wind-turbine converts the kinetic energy available in the wind to the usable electrical energy employing appropriate electrical generator. This power is characterized by performance coefficient (C_p), which inturn is dependent on tip speed ratio (λ) defined as,

$$\lambda = \frac{r\omega_t}{v_w} \quad (3.1)$$

where, r is the radius of the wind turbine blade in ‘ m ’, ω_t is turbine shaft speed in rad/sec , v_w is the wind velocity in m/sec . The C_p as a function of λ and blade pitch angle (β) is expressed as,

$$C_p(\lambda) = C_1 \left(\frac{C_2}{\lambda_i} - C_3\beta - C_4 \right) e^{\frac{-C_5}{\lambda_i}} + C_6\lambda_i \quad (3.2)$$

where, λ_i is given by,

$$\frac{1}{\lambda_i} = \frac{1}{\lambda + 0.08\beta} - \frac{0.035}{1 + \beta^3} \quad (3.3)$$

The mechanical power (P_t) and torque (T_t) made available by the wind-turbine to the SEIG is described by equations 3.4 and 3.5 respectively.

$$P_t = 0.5\rho\pi r^2 C_p v_w^3 \quad (3.4)$$

$$T_t = \frac{P_t}{w_t} \quad (3.5)$$

A gear-box with a gear ratio of ‘GR’ is employed between wind-turbine and the SEIG. This GR relates the mechanical speed (w_t) and the torque (T_t) of the wind-turbine to the speed (w_{sh}) and torque (T_m) of the SEIG given by equations 3.6-3.7

$$\omega_{sh} = w_t \times GR \quad (3.6)$$

$$T_m = \frac{T_t}{GR} \quad (3.7)$$

The system parameters used in (3.1) - (3.7) for wind-turbine modeling are defined in Appendix A.3.

3.3.2 Bidirectional Voltage Source Converter

The concept of switching function is employed to model the dynamics of bidirectional VSC (Lee and Ehsami, 2001). The line voltages (v_{ab}, v_{bc}, v_{ca}) of the VSC are modeled as function of DC-link voltage (v_{dc}) and switching function (S_1, S_3, S_5) and are expressed as,

$$\begin{aligned} v_{ab} &= v_{dc} \times (S_1 - S_3) \\ v_{bc} &= v_{dc} \times (S_3 - S_5) \\ v_{ca} &= v_{dc} \times (S_5 - S_1) \end{aligned} \quad (3.8)$$

The phase currents $[i_{av}, i_{bv}, i_{cv}]^T$ of the VSC are derived using phase currents of the SEIG $[i_{as}, i_{bs}, i_{cs}]^T$ and IM pump $[i_{ai}, i_{bi}, i_{ci}]^T$ by employing KCL at the PCC,

$$[i_{av}, i_{bv}, i_{cv}]^T = [i_{as}, i_{bs}, i_{cs}]^T + [i_{ai}, i_{bi}, i_{ci}]^T \quad (3.9)$$

Now, the DC-link current (i_{dc}) is obtained as sum of switch and diode currents of upper switches of the VSC and is given by

$$i_{dc} = S_1 \times i_{av} + S_3 \times i_{bv} + S_5 \times i_{cv} \quad (3.10)$$

For the generator operation of the SEIG, the i_{dc} is negative and flows into the DC-link capacitor (C_{dc}), resulting in building up of v_{dc} . The dynamics of the v_{dc} is governed by

$$\frac{dv_{dc}}{dt} = -\frac{i_{dc}}{C_{dc}} \quad (3.11)$$

where, C_{dc} is the DC-link capacitor.

3.3.3 Passive line filter

A passive LC filter is employed per phase to reduce the harmonic content in the line-line voltages (Kewat et al., 2018). The R_f in equation 3.12 refers to small resistance, which can be attributed to the internal resistance of the line filter inductance (L_f) and capacitance (C_f). The line filter parameters used in this study are defined in Table B.2. For ease of implementation, these filters are modeled in the s-domain given by.

$$\frac{v_{i(s)}}{v_{o(s)}} = \frac{R_f C_f s + 1}{L_f C_f s^2 + R_f C_f s + 1} \quad (3.12)$$

where, $v_{i(s)}$ and $v_{o(s)}$ are input and output of the filter respectively.

3.3.4 Self Excited Induction Generator

The SEIG model configured in this study takes dq axis voltages as inputs and generates dq axis currents. The dynamics of the SEIG with dq axis stator and rotor currents as state variables is given by,

$$\begin{bmatrix} \dot{i}_{ds} \\ \dot{i}_{qs} \\ \dot{i}_{dr} \\ \dot{i}_{qr} \end{bmatrix} = \frac{1}{L_m^2 - L_s L_r} \begin{bmatrix} L_r R_s & -\omega_r L_m^2 & -L_m R_r & -\omega_r L_m L_r \\ \omega_r L_m^2 & L_r R_s & \omega_r L_m L_r & -L_m R_r \\ -L_m R_s & \omega_r L_m L_s & L_s R_r & \omega_r L_s L_r \\ -\omega_r L_m L_s & -L_m R_s & -\omega_r L_s L_r & L_s R_r \end{bmatrix} \begin{bmatrix} i_{ds} \\ i_{qs} \\ i_{dr} \\ i_{qr} \end{bmatrix} + \begin{bmatrix} -L_r & 0 & L_m & 0 \\ 0 & -L_r & 0 & L_m \\ L_m & 0 & -L_s & 0 \\ 0 & L_m & 0 & L_s \end{bmatrix} \begin{bmatrix} v_{ds} \\ v_{qs} \\ v_{dr} \\ v_{qr} \end{bmatrix} \quad (3.13)$$

To explain the operation of the induction machine as SEIG, it is essential to model magnetizing inductance (L_m) as a non-linear function of magnetizing current (i_m). In this study, a sixth order polynomial is used to express L_m in terms of i_m and is given by

$$i_m = \sqrt{(i_{ds} + i_{dr})^2 + (i_{qs} + i_{qr})^2} \quad (3.14)$$

$$L_m = a_0 + a_1 i_m + a_2 i_m^2 + a_3 i_m^3 + a_4 i_m^4 + a_5 i_m^5 + a_6 i_m^6 \quad (3.15)$$

The electromagnetic torque (T_{es}) developed by SEIG is expressed as function of stator currents, rotor currents, number of poles (P) and L_m given by

$$T_{es} = \left(\frac{3P}{2} \right) L_m (i_{qs} i_{dr} - i_{ds} i_{qr}) \quad (3.16)$$

The behavior of the shaft speed (w_{sh}) is captured employing swing equation given by .

$$\frac{dw_{sh}}{dt} = \frac{T_{es} - T_m}{J} \quad (3.17)$$

3.3.5 Induction Motor Pump

A three phase IM pump is employed as load in this study. This load can be modelled using (3.13)-(3.17) with inclusion of following changes. For motoring operation, the T_e , T_L are positive and the value of L_m is modelled to be constant corresponding to rated voltage and frequency. The load torque is modeled as function of motor speed (w_m) and pump constant (K_p) given by.

$$T_L = K_p \omega_m^2 \quad (3.18)$$

The machine parameters used to model the SEIG and IM pump characteristics are listed in Appendix A.2.

3.3.6 Active and Reactive Power at the PCC

The instantaneous active (p_s) and reactive (q_s) power of the SEIG are computed using respective voltages and currents in the stationary reference frame (Krause et al., 2002)

given by.

$$\begin{bmatrix} p_s \\ q_s \end{bmatrix} = \begin{bmatrix} v_{ds} & v_{qs} \\ -v_{qs} & v_{ds} \end{bmatrix} \begin{bmatrix} i_{ds} \\ i_{qs} \end{bmatrix} \quad (3.19)$$

3.4 DC-link Voltage Regulation (VR) Algorithm

This section presents the developed control scheme to regulate the DC-link voltage. First, the operating principle is elucidated, followed by the significance of the constant ‘V/F’ ratio at the PCC. Lastly, the controller implementation is discussed in detail.

3.4.1 Principle of Operation

The DC-link voltage (v_{dc}) rises if there is an increase in active power pumped into the DC-link capacitor (C_{dc}) and vice versa. In SEIG based WECS, for a given v_w , the active power generation is directly proportional to the operating slip. For an increase in active power into the C_{dc} , the v_{dc} tends to rise. To correct this voltage, the controller increases the frequency (F) of the VSC. This rise in F reduces the operating slip resulting in lowering active power generation by the SEIG.

Additionally, the load (IM pump load) consumption increases with an increase in F . This dual effect of reducing the generation and building load, suddenly regulates the v_{dc} by diverting the excess power to the load. Conversely, a decrease in active power in the C_{dc} tends to reduce v_{dc} . This error in v_{dc} is regulated by decreasing the F of the VSC.

A simple PI controller is chosen to implement the aforementioned algorithm with frequency (F) of the VSC as control variable. Control law governed by equation 3.20 is used to regulate the actual v_{dc} to the set reference value (v_{dcref}).

$$F_{new} = \begin{cases} F_{old} + F_{\Delta} & \text{if } v_{dc} > v_{dcref} \\ F_{old} - F_{\Delta} & \text{if } v_{dc} < v_{dcref} \end{cases} \quad (3.20)$$

where,

F_{new} is the updated frequency

F_{old} is the operating frequency

F_{Δ} is the correction applied using PI controller and is proportional to $(v_{dc} - v_{dcref})$

3.4.2 Need for Constant ‘V/F’ ratio at the PCC

For variable frequency operation of the induction motor, it is essential that the ‘V/F’ ratio of the machine is maintained constant to avoid the flux saturation. The saturated induction machine draws high magnetizing current increasing the losses in the machine. The plot of steady state current drawn versus the operating frequency for Variable Frequency Drive (VFD) with and without constant ‘V/F’ ratio are shown in Figure 3.2, which reveals that for constant m_a and v_{dc} , if the F is reduced, the current drawn increases. On the contrary, for the VFD with constant ‘V/F’ control (constant v_{dc} and varying m_a) the current reduces with the reduction in operating frequency. This firmly establishes the need to maintain ‘V/F’ ratio constant for frequency sensitive loads like induction motor.

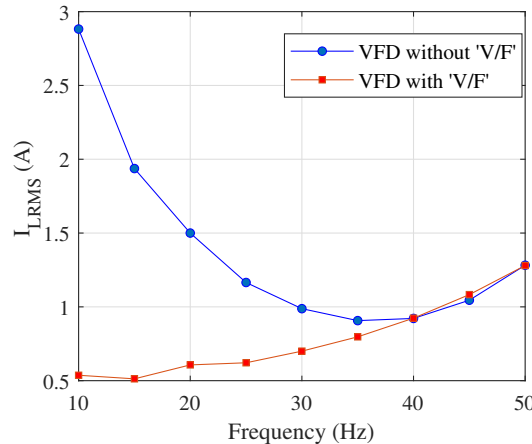


Figure 3.2: Plot of line current versus frequency for Variable Frequency Drive (VFD) feeding 0.75 HP induction motor with and without constant ‘V/F’ control

To avoid saturation in the IM pump and the SEIG, the amplitude modulation index (m_a) is varied to maintain a constant ‘V/F’ ratio. Hence the flux of the IM pump and the SEIG are maintained constant for all operating frequencies. The DC-link voltage and frequency are used to calculate the m_a . It is to be noted that sensing v_{dc} as one of the feedback variables enhances the reliability of the Variable Voltage Variable Frequency (VVVF) source in the event of severe DC-link voltage sag or swell.

3.4.3 Controller Framework

The implementation of DC-link Voltage Regulation (VR) scheme of the VSC assisted SEIG is shown in Figure 3.3. In addition to voltage regulation, the algorithm also maintains the constant ‘V/F’ ratio at the PCC to facilitate constant flux operation of the SEIG and the IM pump.

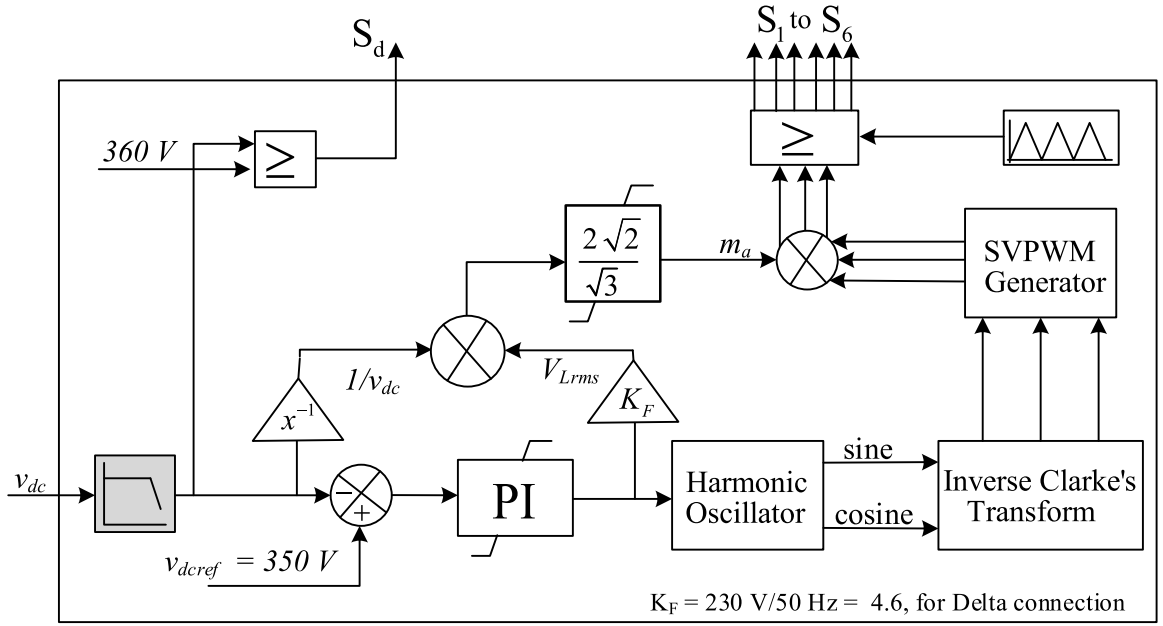


Figure 3.3: Structure of DC-link voltage regulation scheme with constant ‘V/F’ ratio

The reference DC-link voltage ($v_{dc\text{ref}}$) is predefined (350 Volts) based on the required line-line voltage ($V_{L\text{rms}} = 230 \text{ V}$) and chosen PWM technique (SVPWM technique) for VSC (Mohan et al., 2003).

$$\begin{aligned}
 V_{L\text{rms}} &= 0.612 \times 1.15 \times m_a \times v_{dc} \\
 230 &= 0.612 \times 1.15 \times 1 \times v_{dc} \\
 v_{dc} &= 350
 \end{aligned} \tag{3.21}$$

The output of the PI controller (F) is fed to the harmonic oscillator. The harmonic oscillator generates sine and cosine waveforms of variable frequency. Further using suitable reference frame transformation, three sinusoidal waveforms are generated. These sinusoidal waveforms are injected with a third harmonic component to generate SVM sinusoid templates. Concurrently appropriate m_a is calculated by

$$m_a = \frac{V_{Lrms}}{v_{dc}} \cdot \frac{2 \cdot \sqrt{2}}{\sqrt{3}} \quad (3.22)$$

Lastly, the SVPWM unit templates are multiplied with a calculated m_a to generate reference SVPWM waveforms. These reference waveforms are compared with high frequency carrier to generate six pulses which control the VSC to facilitate Variable Voltage Variable Frequency (VVVF) supply at the PCC with a constant ‘V/F’ ratio.

The control for the dump load is exercised using pulse S_d and is governed by

$$S_d = \begin{cases} 1 & \text{if } v_{dc} > 360V \\ 0 & \text{if } v_{dc} < 360V \end{cases} \quad (3.23)$$

The threshold voltage for dump load is deliberately set to 360 V to demonstrate transfer of control from DC-link voltage control to ELC and vice versa. The v_{dc} equals 350 V and 360 V during ELC off (DC-link voltage controller active) and ELC on (DC-link voltage controller inactive - no load/light load condition) respectively. Also, it helps in the validation of controller to maintain constant flux against variations in v_{dc} .

3.5 Simulation and Experimental study

To investigate the performance of the system under consideration with the proposed control strategy, simulation and experimental studies are carried out using system attributes given in appendix A.2 and A.3. The results of these studies will be discussed in this section.

3.5.1 Simulation results

In the present study, the performance of the DC-link VR algorithm to regulate the v_{dc} against variations in wind velocities and the load is investigated. Figure 3.4 (a) illustrates a total of six perturbations introduced to analyze the system behavior which includes four step changes in wind velocity, insertion of IM pump at $t = 4$ s and removal of IM pump at $t = 17$ s.

Figure 3.4 (b) to (f) presents the variations in wind power coefficient (C_p), DC-link voltage (v_{dc}), Frequency (F), amplitude modulation index (m_a) and shaft speed (w_{sh})

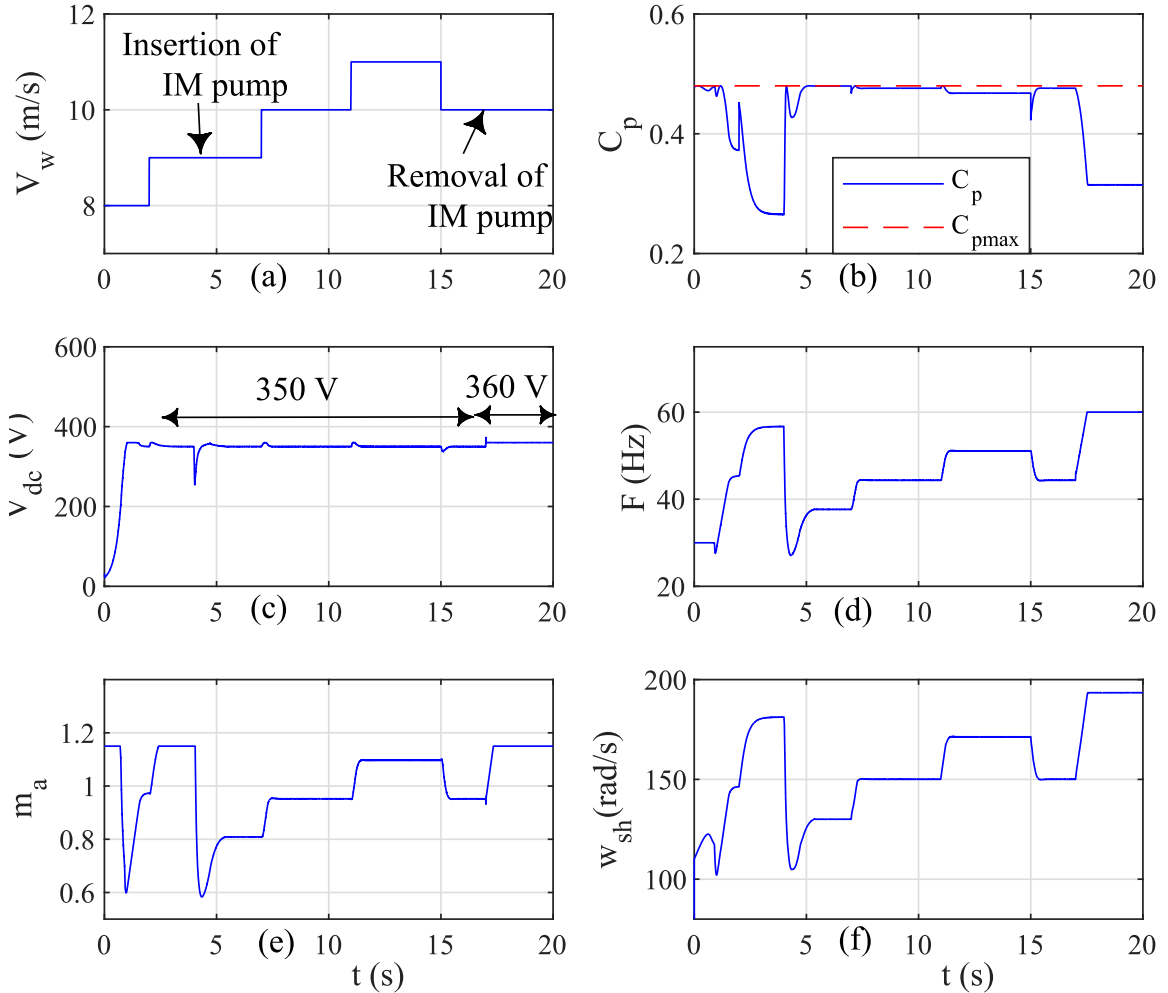


Figure 3.4: Simulation results: (a) Wind velocity profile, (b) Wind power coefficient, (c) DC-link voltage, (d) Frequency, (e) Amplitude modulation index, (f) Shaft speed of the SEIG

for all the perturbations under consideration.

At $t = 0$ s, the pulses ($S_1 - S_6$ and S_d) are applied to the VSC. The v_{dc} starts to build, taking the aid of the initial voltage across the DC-link capacitor (C_{dc}). Initially there is no load on the system, hence the generated active power is pumped into the C_{dc} which leads to increase in F as governed by equation 3.20. The F settles at 44 Hz for v_w of 8 m/s. At $t = 2$ s, the F further increases and settles at 58 Hz due to increase in v_w to 9 m/s.

At $t = 4$ s, an IM pump is inserted as a load on the system. A sudden dip in v_{dc} to 254 V is seen, this can be attributed to large active and reactive power required

for starting of the IM pump. However, the fast acting PI controller decreases the F to 38 Hz which regulates v_{dc} to predefined reference of 350 V.

At $t = 7$ s and $t = 11$ s, v_w is increased from 9 m/s to 10 m/s and from 10 m/s to 11 m/s respectively. This increases active power pumped into the C_{dc} leading to increase in F to 44 Hz and 51 Hz respectively. On the contrary at $t = 15$ s, v_w is decreased from 11 m/s to 10 m/s bringing back F to 44 Hz.

At $t = 17$ s, the IM pump is disconnected. The F starts increasing to reduce the generated power before it saturates at 60 Hz. After saturation of F , v_{dc} starts to rise and reaches 360 V, transferring control to the ELC. The active power generated by the SEIG at v_w of 10 m/s is diverted to the dump load.

Besides DC-link voltage regulation, the algorithm also commits to maintaining ‘V/F’ ratio of the supply at the PCC constant. Figure 3.5 (a) shows the magnitude of fundamental RMS line voltage (V_{1rms}) and operating frequency at the PCC and that of Figure 3.5 (b) reveals the ‘V/F’ ratio of the power supply at the PCC for the entire operating range (from $t = 0$ -20 s). By virtue of the constant ‘V/F’ block in the VR algorithm, for every change in frequency, the V_{1rms} varies accordingly to maintain the ‘V/F’ ratio equal to 4.6 at the PCC against all disturbances. For the region where the IM pump is present as the load, the ‘V/F’ ratio is maintained at 4.6. However, a deviation in ‘V/F’ ratio is seen at two instances with dump load (R load). This can be attributed to saturation of F at 60 Hz and transfer of control to ELC with dump load.

In addition to analyzing the behavior of the system variables for all perturbations, following noteworthy observations can be made from the Figure 3.4.

- It is evident from Figure 3.4 (b) that, C_p exhibits superior performance when IM pump is connected (from $t = 4$ s to $t = 17$ s) and deviates significantly from its ideal value of 0.48 otherwise. This can be attributed to adequate sizing of IM pump for chosen SEIG and the judicious choice of the gear ratio employed in the wind-turbine.
- Figure 3.4 (e) depicts that for every change in F , the m_a value changes accordingly as governed by (3.22) to ensure constant ‘V/F’ ratio of 4.6 at the PCC.
- Although the proposed algorithm is speed sensorless, The behavior of shaft speed of SEIG (ω_{sh}) is crucial as it decides the optimal λ to ensure best C_p

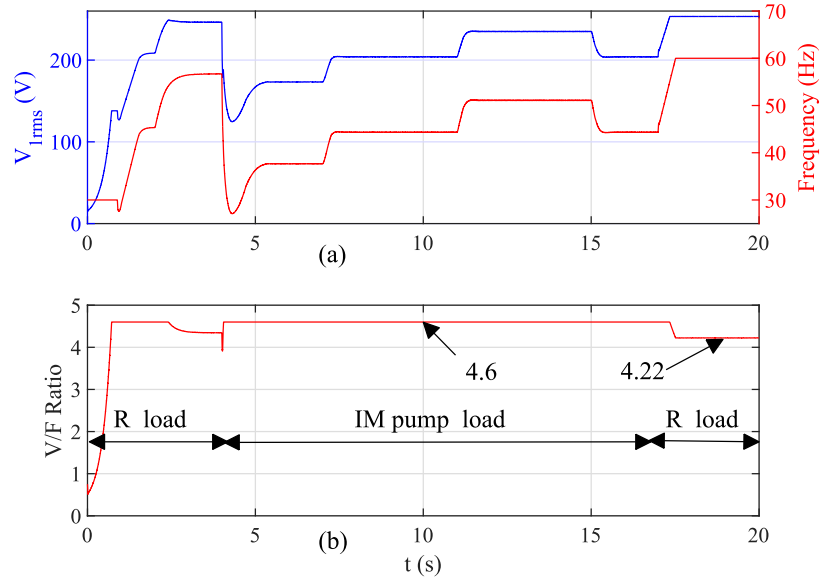


Figure 3.5: (a) Fundamental RMS Line voltage and Frequency (b) ‘V/F’ ratio for entire operating range

value. Figure 3.4 (f) shows that the ω_{sh} exhibits direct proportionality with F . This aspect of the system is exploited to design the proposed control strategy choosing F as control variable.

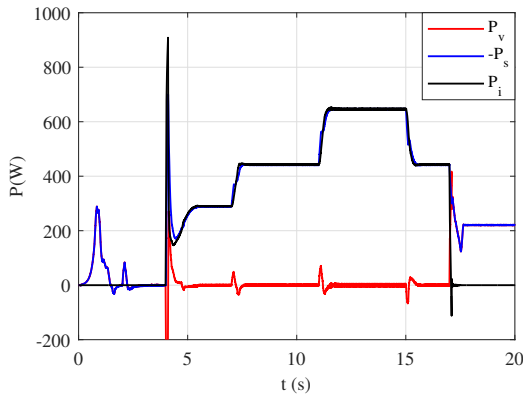


Figure 3.6: Active power flow at PCC

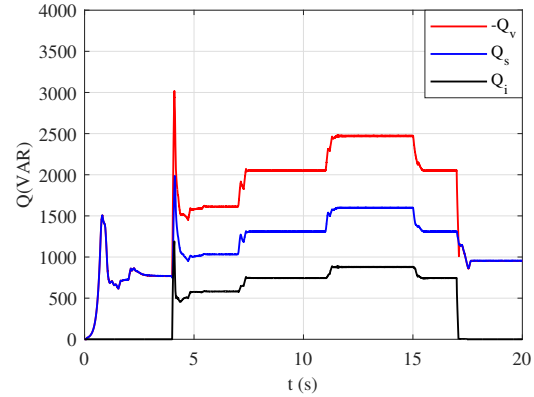


Figure 3.7: Reactive power flow at PCC

To substantiate the synergy between the VSC, the SEIG and the IM pump connected at the PCC, active and reactive power at the PCC is examined. In the system under consideration, the active power and reactive power requirement are fulfilled by the SEIG and the VSC assisted DC-link capacitor, respectively and is given by

$$\begin{aligned}
P_s &= P_v + P_i \\
Q_v &= Q_s + Q_i
\end{aligned}
\tag{3.24}$$

where,

P_s, P_v, P_i are the average active power of the SEIG, VSI and the IM respectively

Q_s, Q_v, Q_i are the average reactive power of the SEIG, VSI and the IM respectively

Figure 3.6 and Figure 3.7 shows the active and reactive power computed at the PCC for all the perturbations. It is evident from the plots that equation 3.24 is satisfied for entire operating range, thus confirming the system power balance.

3.5.2 Experimental Results

The laboratory prototype developed for verification of DC-link VR algorithm is shown in Figure B.2. The test results are obtained for the same set of perturbations discussed for simulation study, shown in Figure 3.4 (a) of section 3.5.1.

The starting performance of the SEIG is assessed at the rated frequency with maximum mechanical power input to ensure safe operating currents in the system for the proposed algorithm. The starting transients of the line voltage and current of the SEIG are captured in Figure 3.8. It is evident from the waveforms that the starting transients die out in 0.5 s and the steady-state currents are within the operable limits of the induction machine configured as the SEIG thus manifesting a satisfactory starting response.

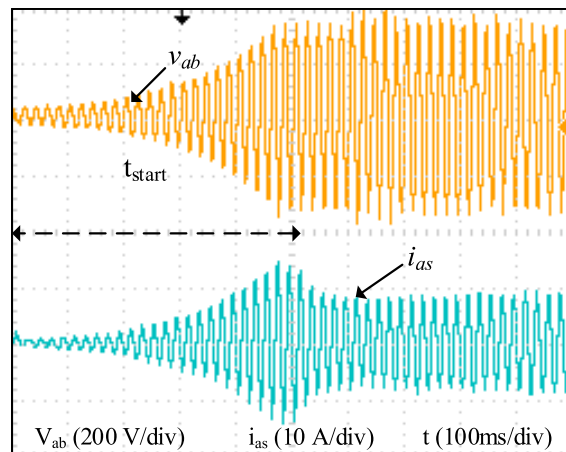


Figure 3.8: Starting performance of the SEIG

The behaviour of v_{dc} is recorded in Figure 3.9 and that of F and m_a are recorded in Figure 3.10. The variations in v_{dc} , F and m_a for the entire operating range comply with discussions presented for simulation studies shown in Figure 3.4 (c), (d) and (e) of section 3.5.1.

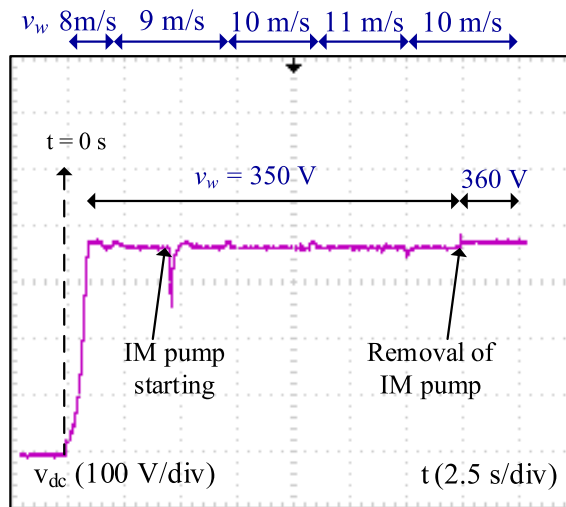


Figure 3.9: DC-link Voltage

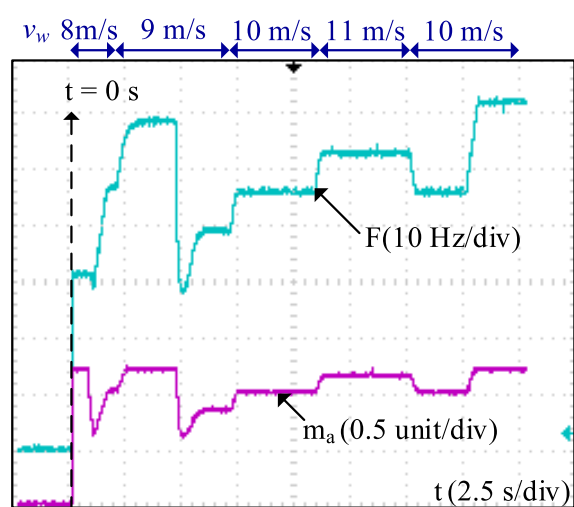


Figure 3.10: Frequency and amplitude modulation index

Figure 3.11 illustrates the behavior of the system line currents and voltages recorded for all perturbations. The system currents consist of line currents of the VSC (Figure 3.11 (a) and (b)), the SEIG (Figure 3.11 (c) and (d)) and the IM pump (Figure 4.9 (e) and (f)). Figure 3.11. (a),(c) and (e) illustrate the behavior of the system line currents for all the perturbations shown in Figure 3.11 (a), which unveils that the current levels are within operable limits of SEIG, IM and VSC.

The system voltages (Figure 3.11 (g) and (h)) are the line voltages at the PCC, where the VSC, the SEIG and the IM pump are connected in parallel. Figure 3.11 (g) captures the line voltage variation at the PCC. It is observed that the peak of the line voltage varies with variation in v_w . This can be attributed to variation in line voltage magnitude by the controller following F , to maintain constant ‘V/F’ ratio at the PCC.

The steady-state system currents and voltages for VR algorithm is captured at $v_w = 9$ m/s is shown in Figure 3.11 (b),(d),(f) and (h). From these waveforms, it is apparent that the system currents and voltages are quasi sinusoidal and balanced, exhibiting satisfactory steady-state response of the system.

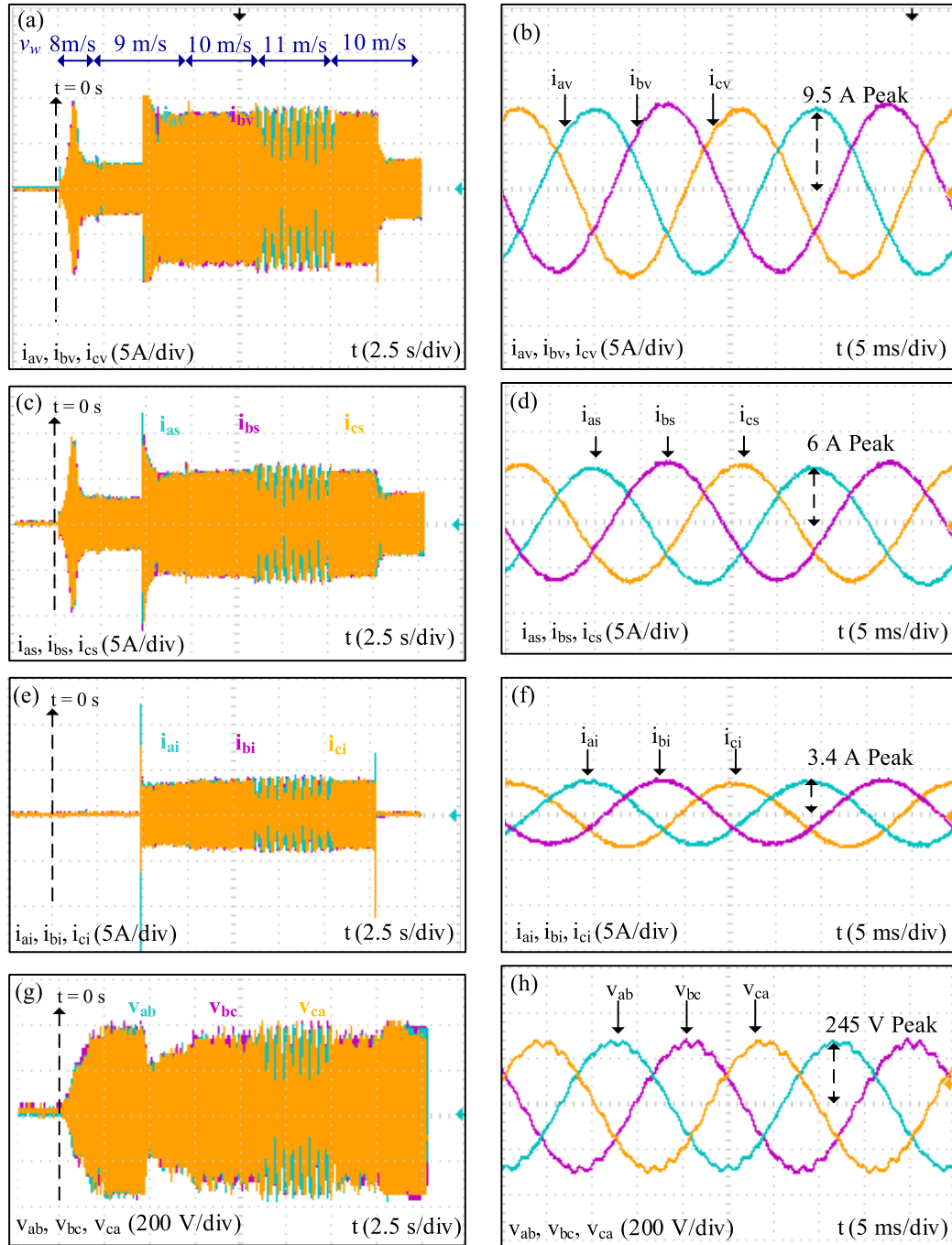


Figure 3.11: Dynamic behavior of system currents and voltages for DC-link Voltage Regulation (VR) algorithm: (a) VSC currents, (c) SEIG currents, (e) IM pump currents and (g) Line voltages at PCC for entire operating range ($t = 0 - 20$ s); Steady-state behavior of system currents and voltages for $v_w = 9$ m/s : (b) VSC currents, (d) SEIG currents, (f) IM pump currents and (h) Line voltages at PCC

The simulation and test results reveal that the VR algorithm regulates v_{dc} to value of 350 V against frequent variations in v_w and the load. It is noteworthy that the algorithm requires just the magnitude information of the v_{dc} for algorithm processing. Additionally, the algorithm also maintains the ‘V/F’ ratio constant at the PCC, thus preventing saturation issues in the IM pump and the SEIG.

Chapter 4

Maximum Power Point Tracking of SEIG Based WECS

4.1 Introduction

In the previous chapter, a DC-link voltage regulation algorithm for VSC assisted SEIG-based WECS feeding IM pump is presented. This chapter proposes another control technique for the identical system to track Maximum Power Point (MPP) employing a simple hill-climbing algorithm. The proposition involves a single VSC for power conditioning and MPPT. Secondly, it uses only the SEIG active power input for decision making and eliminates the speed and wind velocity sensors making the algorithm speed sensorless. Besides MPPT using the reduced converter count, the SEIG and the IM pump's constant flux operation are accomplished to increase the system's efficiency and life expectancy. Decisively, a comparative study is presented to highlight the merits offered by the suggested hill-climbing MPPT algorithm.

4.2 System Description

The system considered for verification of proposed speed sensorless hill-climbing MPPT algorithm is identical to system discussed in section 3.2. It consists of wind turbine emulator, the SEIG, two level VSC, IM pump, Electronic Load Control (ELC) with dump load and system controller.

As can be seen, only two-level VSC is employed to effectively transfer the power

from the SEIG to the IM pump. A simple hill-climbing algorithm is employed to extract maximum power from the wind turbine. This algorithm requires active power generated by the SEIG which in turn is computed by sensing two line currents ($i_{as,l}$ and $i_{bs,l}$) of the SEIG and the DC-link voltage (v_{dc}). In the system under consideration, the SEIG caters to the active power requirement and the DC-link capacitor assisted by VSC fulfill the reactive power requirement. The active and reactive power flow is as shown in Figure 4.1, ensuring power balance in the system.

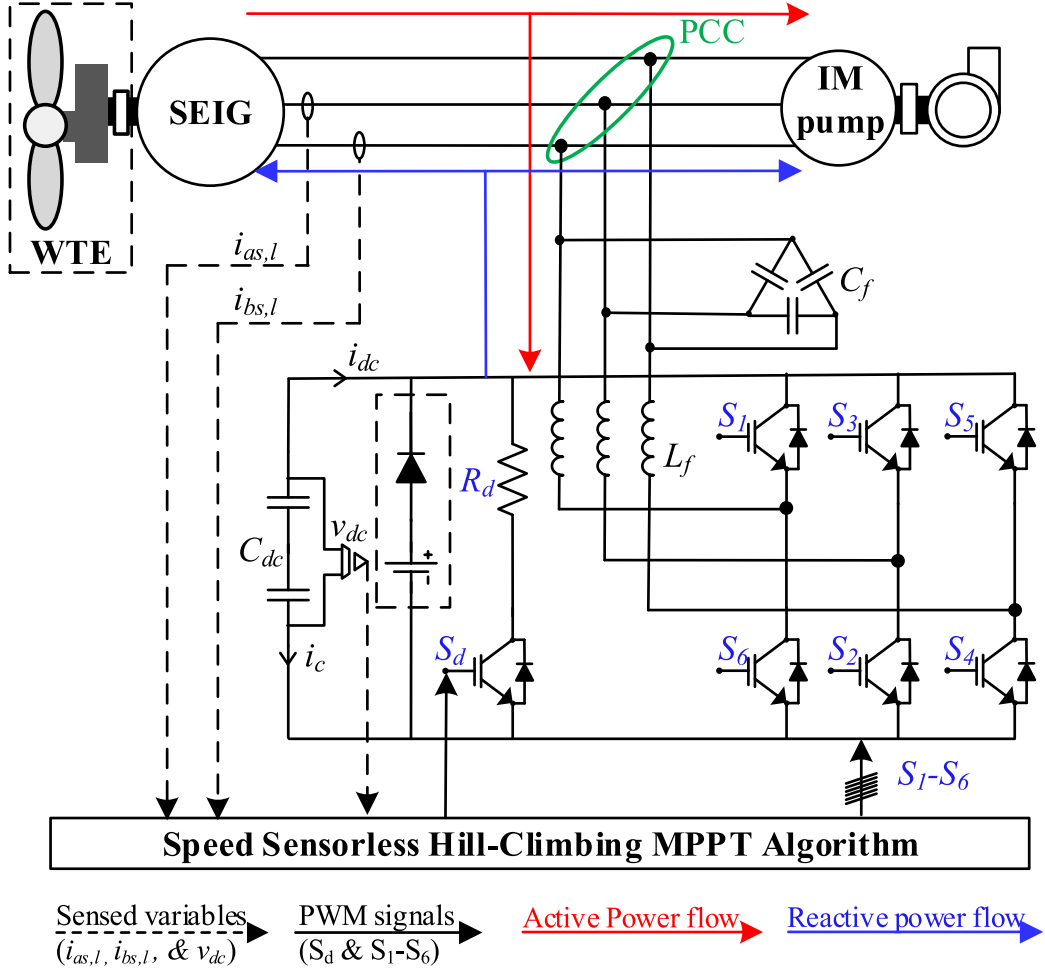


Figure 4.1: Circuit diagram of wind-turbine driven, VSC assisted SEIG feeding IM pump with speed sensorless hill-climbing MPPT algorithm

4.3 Speed Sensorless Hill-Climbing algorithm

This section presents the operating principle of the WECS and the framework of a speed sensorless hill-climbing algorithm for maximum power point tracking.

4.3.1 Operating Principle

The power extracted from the wind-turbine is characterized by the power coefficient curve and varies with varying wind velocities (v_w) as shown in Figure 4.2 (a) and (b) respectively. Further, it is evident from Figure 4.2 that, there exist a single operating point to ensure maximum power extraction from the wind, which occurs at $\lambda = \lambda_{opt} = 0.48$. To ensure this optimal operating point for WECS against varying wind velocities and loads, the MPPT algorithms are employed.

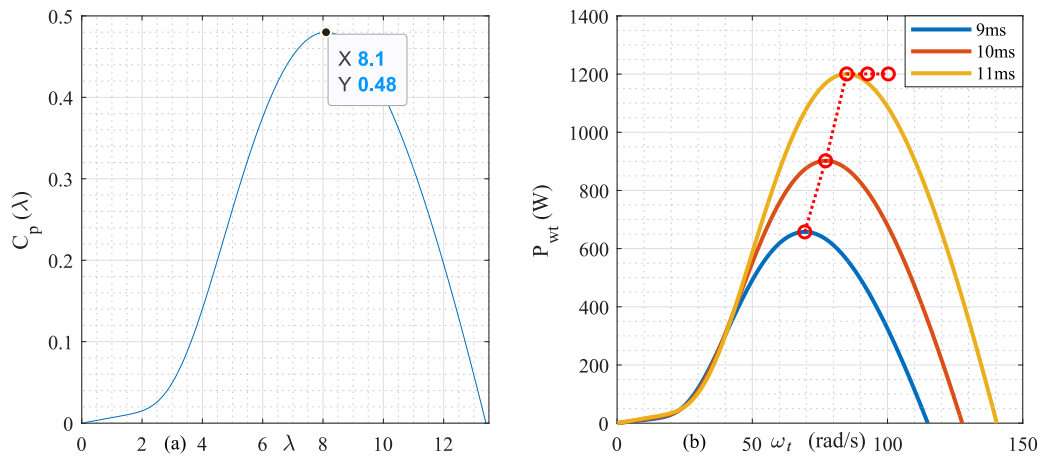


Figure 4.2: (a) Power coefficient curve (b) Mechanical power developed by wind turbine for varying wind velocity

Hill climbing algorithm is a simple perturbation based algorithm meant for MPPT in solar PV, WECS, or any source which exhibits non-linear power characteristics. These algorithms monitor perturbation in sensed/computed variables for continuous polling of the MPP and introduce a step-change in the control variable to consistently move the operating point towards Maximum Power Point (MPP). In WECS, the sensed and control variables are governed by the choice of a generator, power converter and the load.

In the present study, a simple hill-climbing algorithm is proposed to track MPP with the operating frequency (F) of the VSC as a control variable. Two line currents

of the SEIG ($i_{as,1}, i_{bs,1}$) and the DC-link voltage (v_{dc}) are sensed in this algorithm. The line voltages required for power computation are estimated using the switching pulses (S_1, S_2 and S_3) and the v_{dc} given by

$$\begin{aligned} v_{ab} &= v_{dc} \times (S_1 - S_3) \\ v_{bc} &= v_{dc} \times (S_3 - S_5) \\ v_{ca} &= v_{dc} \times (S_5 - S_1) \end{aligned} \quad (4.1)$$

The sensed line currents and the estimated line voltages are subjected to Clarke's transformation to obtain dq axis currents and voltages. Further, the generated active power from SEIG (P_s) is computed for every change in F employing equation 4.2 to track the MPP on the wind turbine's ' $C_p - \lambda$ ' curve. Unlike perturb and observe algorithm, only active power input from the SEIG is used in this algorithm for decision making, thus eliminating the need for speed sensor.

$$P_s = v_{ds}i_{ds} + v_{qs}i_{qs} \quad (4.2)$$

4.3.2 Controller Framework

The detailed flowchart of the algorithm is shown in Figure 4.3. The P_s is computed using equation 4.2. This power is sampled at regular intervals of time equal to 0.1 s (for firmware development and simulation studies) and change in active power (ΔP) is calculated. Depending on the sign of (ΔP), the SEIG's shaft speed is adjusted by controlling F judiciously. The F is continuously updated to ensure MPPT for varying wind velocities. The hill-climbing algorithm is updated every 0.1 s to generate new F . This F is given as input to the constant 'V/F' pulse generation unit discussed in section 3.4.3.

The constant 'V/F' pulse generation unit consists of the SVPWM block, m_a computation block and the ELC block. The SVPWM block takes F as input to generate orthogonal unit sinusoids employing a harmonic oscillator, which are converted to three phase sinusoids using inverse Clarke's transform. These sinusoids are injected with a third harmonic component and multiplied with m_a . The computation of m_a is performed by m_a computation block taking F and v_{dc} as inputs. The value of m_a

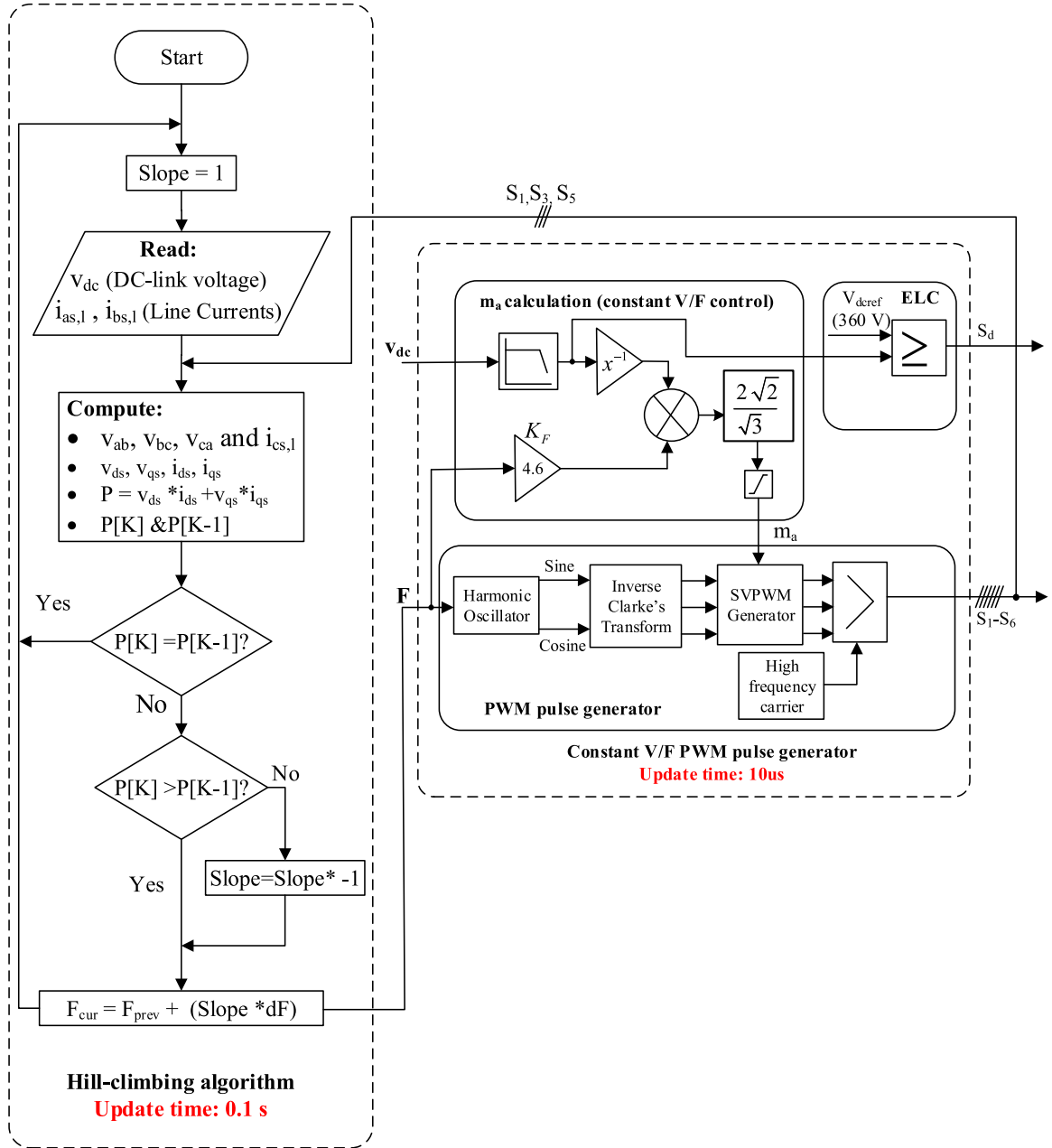


Figure 4.3: Hill-Climbing Algorithm for VSC assisted SEIG based WECS with frequency (F) as control variable

is updated for every change in frequency to maintain K_F ('V/F' ratio) constant at the PCC. The weighted sinusoids from the SVPWM generator are compared with a high-frequency carrier wave to generate the switching pulses fed to the VSC ($S_1 - S_6$). The ELC block consists of a simple comparator that compares v_{dc} with a reference

value of 360V and diverts the surplus active power to the dump load.

4.4 Simulation and Experimental Study

In this section, the simulation and experimental results are elucidated to demonstrate the MPPT of SEIG based stand-alone WECS feeding an IM pump using the proposed speed sensorless hill-climbing algorithm. The system parameters used for simulation and experimental studies are presented in sections A.2 and A.3.

4.4.1 Simulation Results

The system's performance for speed sensorless hill-climbing algorithm is assessed by closely monitoring critical variables in the wind-turbine, SEIG, VSC, and the IM pump. The perturbations for the study include step changes in wind velocity as shown in Figure 4.4 (a).

The dynamic response of the system variables (v_w , C_p , w_{sh} , P_{wt} , F , P_s , m_a , P_i , v_{dc} and P_{dc}) to the aforementioned perturbations are recorded in Figure 4.4 (a) to Figure 4.4 (j) respectively.

At $t = 0$ s, the simulation is initiated with initial shaft speed (ω_{sh}) of 120rad/sec , the v_{dc} starts to rise and reaches the predetermined voltage of 360 volts. The generated active power in the SEIG (P_s) is diverted to dump load (P_{dc}) as no other load is connected to the SEIG. The hill-climbing algorithm starts to pursue MPP by perturbing the control variable F and settles around 37.5 Hz at $t = 4$ s, exhibiting steady-state oscillations to ensure optimum C_p (0.48) and hence P_{wt} . Based on the value of F , the m_a is adjusted to ensure constant 'V/F' ratio at the PCC. At $t = 5$ s, an IM pump load is connected to the line terminals of the SEIG, entire power from the P_{dc} is now diverted to this active load accompanied by a sudden dip in v_{dc} . This dip is attributed to large active power requirement during starting of IM pump. The value of F remains unchanged as the v_w is not disturbed. However, the m_a increases to maintain the 'V/F' ratio constant at the PCC thus compensating for sudden dip in v_{dc} .

At $t = 8$ s, v_w is increased to 10 m/s with IM pump, following this increase in v_w , the value of F starts increasing from 37.5 Hz to track maximum power point and eventually settles around 41.5 Hz.

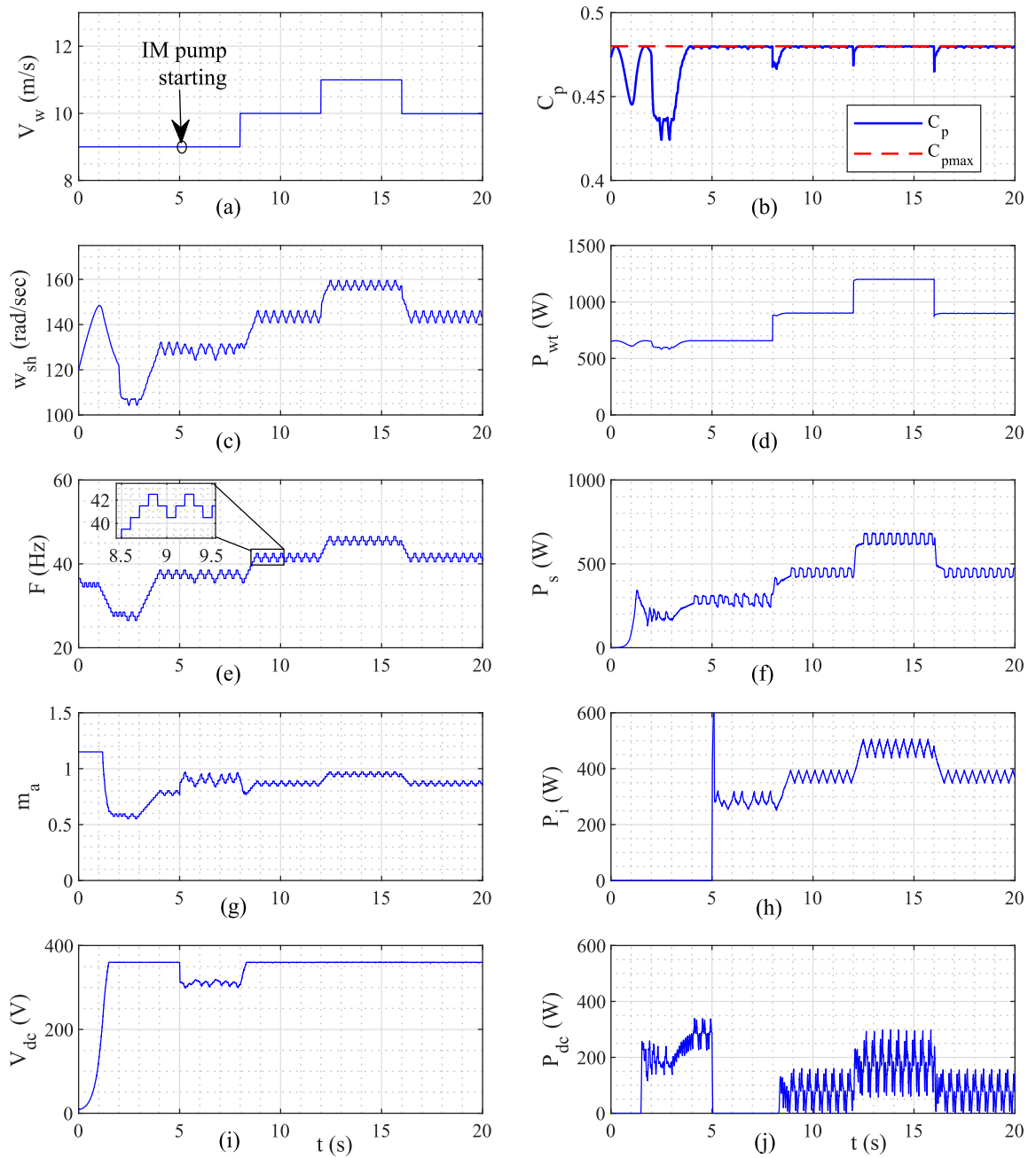


Figure 4.4: Simulation results: (a) Wind velocity profile, (b) Wind power coefficient, (c) Mechanical shaft speed of the SEIG, (d) Active power developed by the wind-turbine, (e) Operating frequency of the VSC, (f) Active power generated by the SEIG, (g) Amplitude modulation index, (h) Active power consumed by the IM pump, (i) DC-link voltage, (j) Active power dissipated in dump load

At $t = 12$ s, v_w is increased to 11 m/s with IM pump load, F starts increasing from 41.5 Hz to hunt for MPP and settles at 45 Hz. Any surplus power unused by the IM pump load is directed to dump load (P_{dc}).

At $t = 16$ s, v_w is decreased to 10 m/s with IM pump load, P_{wt} reduces drastically, the hill-climbing algorithm starts reducing the F to reduce the load and w_{sh} . Eventually, the F settles back to 41.5 Hz from 45 Hz to ensure MPP operation. In the event of a sudden decrease in wind velocity, any immediate requirement of active power is fulfilled by the power in the dump load or DC-link capacitor to prevent the collapse of the DC-link voltage.

In addition to MPPT, the speed sensorless hill-climbing algorithm also maintains the ‘V/F’ ratio of the supply at the PCC constant. The magnitude of fundamental RMS line voltage ($V_{I_{rms}}$) and operating frequency at the PCC is shown in Figure 4.5 (a) and that of Figure 4.5 (b) reveals the ‘V/F’ ratio of the power supply at the PCC for the entire operating range (from $t = 0$ -20 s). Unlike VR algorithm discussed in chapter 3, the operating frequency is independent of the type of the load (IM pump / dump load). Hence, the ‘V/F’ ratio is maintained constant at 4.6 against all the disturbances.

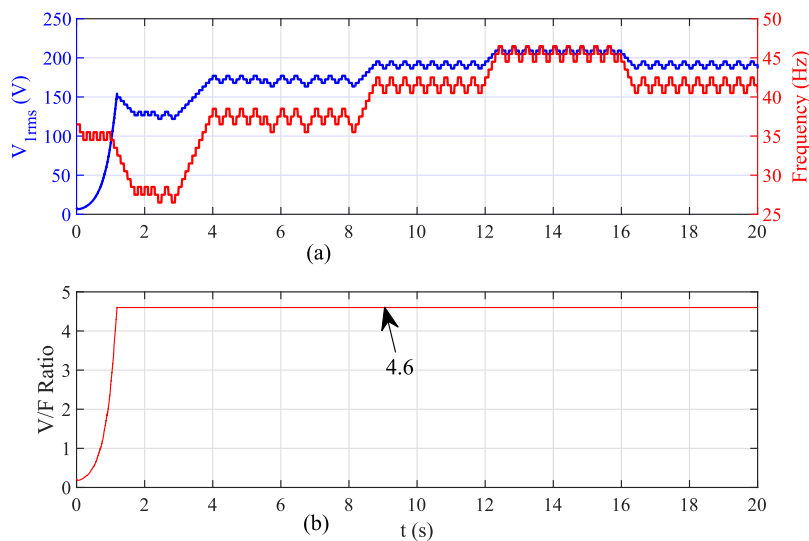


Figure 4.5: (a) Fundamental RMS Line voltage and Frequency of the supply at the PCC, (b) ‘V/F’ ratio of the supply at the PCC for entire operating range

Besides the response of system variables to the perturbations, the following are some noteworthy observations evident from Figure 4.4 that give more in-depth insights into the system’s dynamics.

- Increase in F reduces the operating slip of the SEIG leading to increased ω_{sh} and vice versa.
- The m_a changes in accordance with F as explained in Figure 4.3 to maintain constant ‘V/F’ ratio at the PCC for the entire operating range.
- For every change in v_w , a momentary dip in the C_p is observed which regains it’s optimal value (0.48) owing to action of hill-climbing algorithm.
- It is apparent from waveforms that $P_s = P_i + P_{dc}$ at all times. The P_s is first utilized by the IM pump and only surplus active power is diverted to P_{dc} .

4.4.2 Experimental Results

The details of the experimental setup used to testify the operation of speed sensorless hill-climbing algorithm is presented in appendix B.3. The starting performance of the SEIG based WECS for the proposed speed sensorless hill-climbing algorithm is shown in Figure 4.6. It is evident from the waveform that the SEIG builds the required voltage in 1.25 s completing the starting transient. Also, the SEIG currents are restricted to the operating limits of the machine during the starting process. Hence the starting performance of the system is said to be satisfactory.

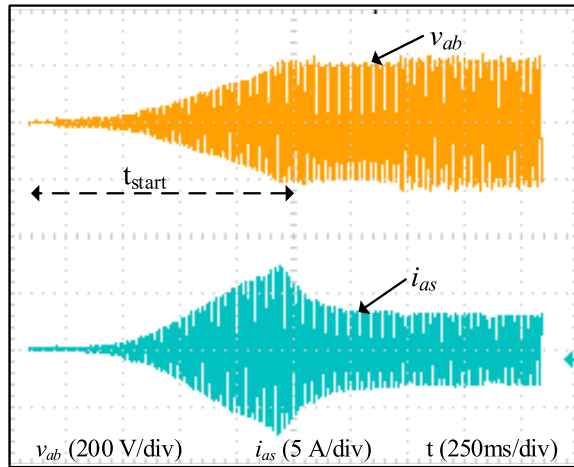


Figure 4.6: Starting performance of the SEIG

Further, the dynamic response of the system is studied by analyzing the behavior of v_{dc} , F and m_a for all the perturbations. Figure 4.7 exhibits the behavior of

the v_{dc} where it is shown to survive the crucial disturbance of IM pump starting at $t = 5$ s. For higher v_w , the ELC diverts any excess active power to the dump load thus maintaining v_{dc} at 360 V.

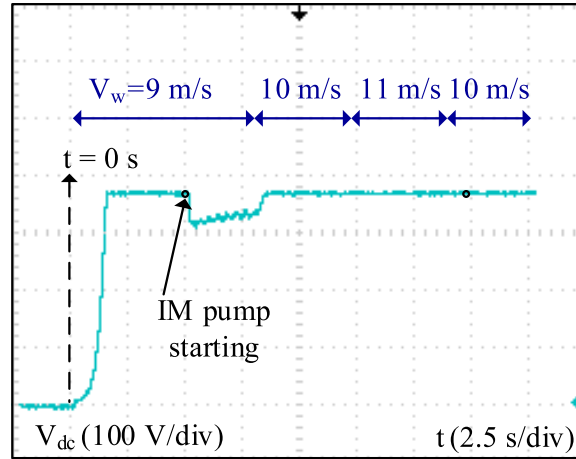


Figure 4.7: DC link Voltage

Figure 4.8 shows the response of the control variables (F , m_a) for change in v_w . The waveform exhibits that the F varies to push the ω_{sh} to an optimal value to ensure maximum power extraction against varying wind velocities. The m_a , in turn, is varied following changes in F to maintain a constant ‘V/F’ ratio at the PCC. Further, Figure 4.8 reveals that the tracking time of the proposed algorithm is approximately 5-6 time constants (0.5 s - 0.6 s) for change in v_w of 1 m/s.

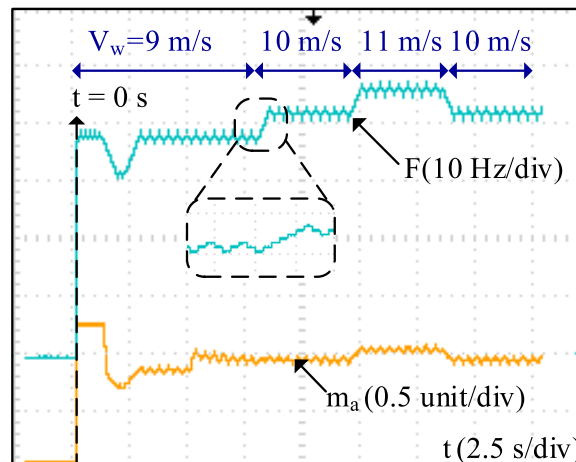


Figure 4.8: Frequency and amplitude modulation index

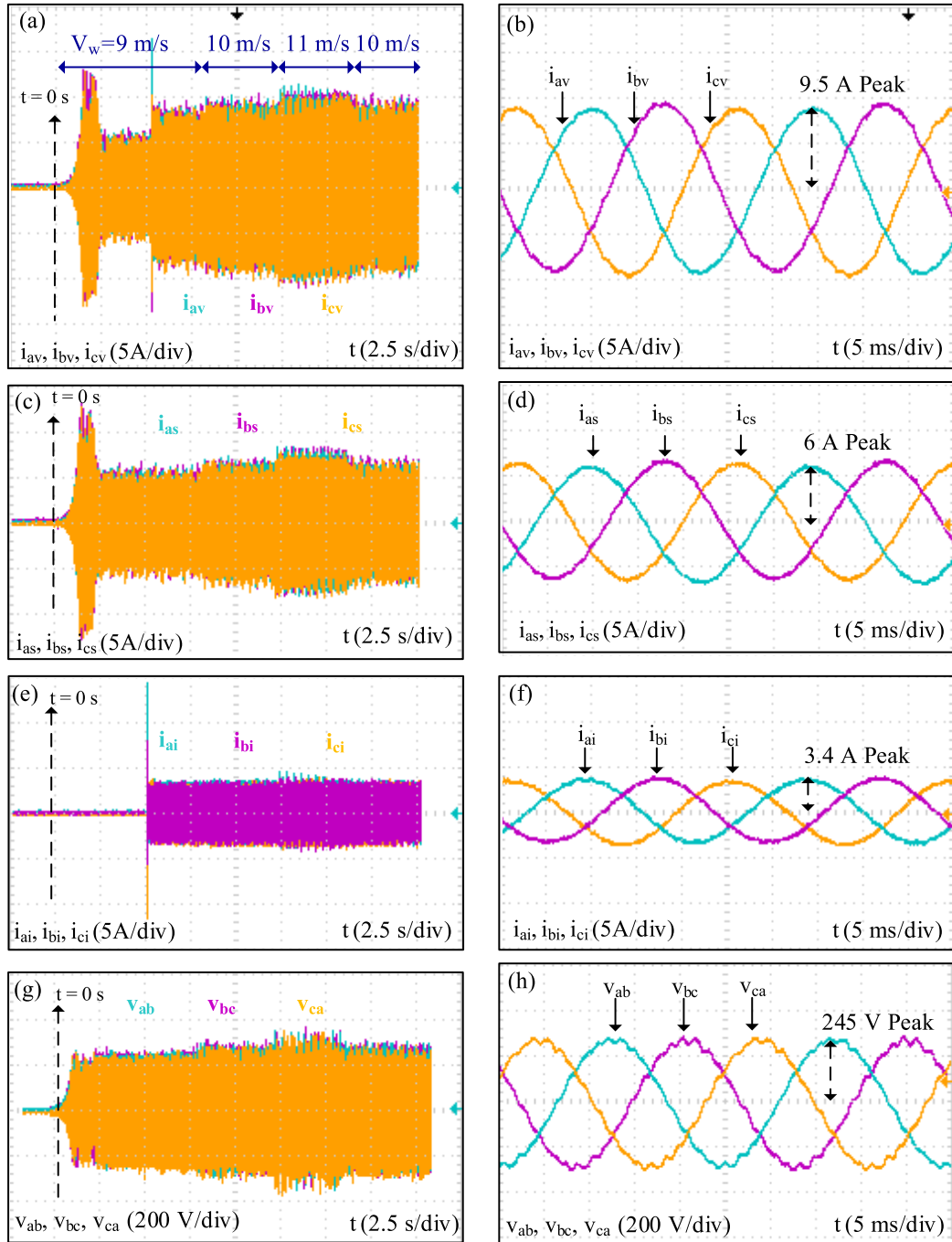


Figure 4.9: Dynamic behavior of system currents and voltages for speed sensorless hill-climbing MPPT algorithm: (a) VSC currents, (c) SEIG currents, (e) IM pump currents and (g) Line voltages at PCC for entire operating range ($t = 0 - 2.0$ s); Steady-state behavior of system currents and voltages for $v_w = 10$ m/s : (b) VSC currents, (d) SEIG currents, (f) IM pump currents and (h) Line voltages at PCC

The dynamic and steady-state response of the system currents and voltages for all perturbations are captured in Figure 4.9 (a)-(h). It is evident from these waveforms that the system currents are within permissible limits of the machines for entire operating range. Further, the steady-state waveforms captured for $F = 40$ Hz exhibit the quasi sinusoidal nature of the currents and the voltages revealing satisfactory steady-state performance yielding improved efficiency and life expectancy of the overall system.

4.5 Comparative Analysis

A qualitative comparison of the proposed algorithm with other MPPT techniques for WECS is presented in Table 4.1. The generators used in WECS dictate several aspects like cost, power converter and the output control variable for achieving MPPT. Employing SEIG as a generator (Miller et al., 1997, Mishra et al., 2019, Ouchbel et al., 2014, Bašić et al., 2019, Kumar and Vijayakumar, 2020, Bašić et al., 2021) for low-power wind turbines reduces cost and maintenance while increasing the system's robustness compared to PMSG based WECS (Chen et al., 2016, Fathabadi, 2017, Hussain and Mishra, 2016, Boopathi et al., 2020).

The VSC assisted SEIG based WPS discussed in this chapter is a desirable proposition as it uses a single VSC for power conditioning. The proposed algorithm does not require knowledge of any system parameter hence making it more comprehensive compared to (Ouchbel et al., 2014, Bašić et al., 2019, 2021). Further, it requires two current sensors and one voltage sensor for algorithm processing, which are inexpensive and less prone to aging/failure. Unlike most of the studies, the load considered for the testing algorithm is the IM pump, which exhibits dynamic loading on the SEIG based on the VSC's operating frequency. Most importantly, the proposed algorithm is realized using a low-cost TMS320F28069M controller unlike work reported in (Mishra et al., 2019, Bašić et al., 2019, 2021) showing its implementation feasibility.

Table 4.1: Qualitative comparison of MPPT techniques for WECS

P	1	2	3	4	5	6	7	8,9	10	Proposed
A	SEIG	SEIG	SEIG	SEIG	SEIG	SEIG	PMSG	PMSG	PMSG	SEIG
B	1	2	1	1	2	1	2	2	2	1
C	5	1	5	4	1	3	2	4	6	3
D	No	Yes	Yes	No	Yes	Yes	Yes	Yes	Yes	Yes
E	IM pump	Resistor	IM pump	Battery	DC Nanogrid	Battery	DC bus	Resistor	IM pump	IM pump
F	No	Yes	No	Yes	Yes	Yes	No	Yes	Yes	Yes
G	No	Yes	No	Yes	Yes	Yes	No	Yes	Yes	Yes
H	Simple	Simple	Complex	Complex	Simple	Complex	Complex	Complex	Complex	Simple
I	Low	Moderate	Moderate	Moderate	Moderate	High	Moderate	Expensive	Expensive	Low
J	Yes	No	Yes	Yes	No	Yes	No	Yes	Yes	No
K	MC	Dspace	-	Dspace	MC	Dspace	DSC	MC	FPGA	DSC

Note - P: System parameter, A: Generator used, B: Converter count, C: Sensor count, D: Speed sensorless, E: Load, F: Oscillation, G: Adaptive, H: Complexity, I: Cost, J: Knowledge of system parameter, K: Controller used for implementation; MC: Micro-Controller; DSC: Digital Signal Controller

[!hbt]

1. (Miller et al., 1997)
2. (Mishra et al., 2019)
3. (Ouchbel et al., 2014)
4. (Bašić et al., 2019)
5. (Kumar and Vijayakumar, 2020)
6. (Bašić et al., 2021)
7. (Chen et al., 2016)
8. (Fathabadi, 2017)
9. (Hussain and Mishra, 2016)
10. (Boopathi et al., 2020)

Chapter 5

Composite Controller for Hybrid Wind-PV Water Pumping System

5.1 Introduction

This chapter presents a stand-alone hybrid Wind-PV Water Pumping System (WPS) with minimal power electronics interface, simple composite controls and Energy Management Strategy (EMS) for effective utilization of renewable sources, by amalgamating contributions of chapters 2 through 4.

The proposition consists of classic Perturb and Observe (P&O) algorithm applied to the boost converter of the Solar PV system and voltage regulation algorithm/hill-climbing MPPT algorithm with Zero Steady-State Oscillation (ZSSO) applied to bidirectional Voltage Source Converter (VSC) of Wind Energy Conversion System (WECS) for optimal power extraction at all times. The constant Voltage to Frequency (V/F) ratio is ensured at the Point of Common Coupling (PCC) for the entire operating range to avoid saturation in the Self Excited Induction Generator (SEIG) and the Induction Motor (IM) pump. The energy management strategy is devised to effectively harness renewable energy from both sources while ensuring the DC-link voltage stability. The proposed system forms compelling proposition given the least converter count to integrate solar-PV and wind energy employing effective and low-complex control algorithms with optimal energy extraction. Conclusively a comparative evaluation is performed with other hybrid WPS to prove the viability of the proposed system for deployment in remotely located stand-alone applications.

5.2 System description

The structure of the proposed standalone hybrid Wind-PV WPS with a composite controller is shown in Figure 5.1. The system consists of two renewable sources, the Solar PV system and WECS. An asynchronous squirrel cage induction machine is configured as SEIG coupled to wind turbine forming WECS. Two power converters, namely the boost converter and the bidirectional VSC, are employed for power processing.

The boost converter primarily intended to extract maximum power from the solar PV system also boosts the solar PV voltage (v_{pv}) to required DC-link voltage (v_{dc}) in the range of 350-360 V. The VSC in the system is liable for active and reactive power management at the PCC and is designed to carry currents responsible for overall active and reactive power. Additionally, the VSC performs other functions like MPPT and voltage regulation for SEIG based WECS. The three-phase Induction Motor (IM) pump is the dynamic load on the system. During surplus power generation by the sources, no-load or light-load condition, the available active power is absorbed by the dump-load with Electronic Load Control (ELC). The dump-load with ELC in this study is configured using resistor bank in series with IGBT switch. The DC-link capacitor fulfills the reactive power requirement of the SEIG and the IM pump. An ancillary setup of a 12 V battery along with a series diode is placed in parallel with the DC-link capacitor to fulfill the initial reactive power requirement of the SEIG during starting.

The controller is the core of the system which is responsible for maximum power extraction from both the renewable sources, DC-link voltage regulation and power balance at the PCC. The sensors employed for overall system control consists of system currents and voltages shown in the Figure 5.1.

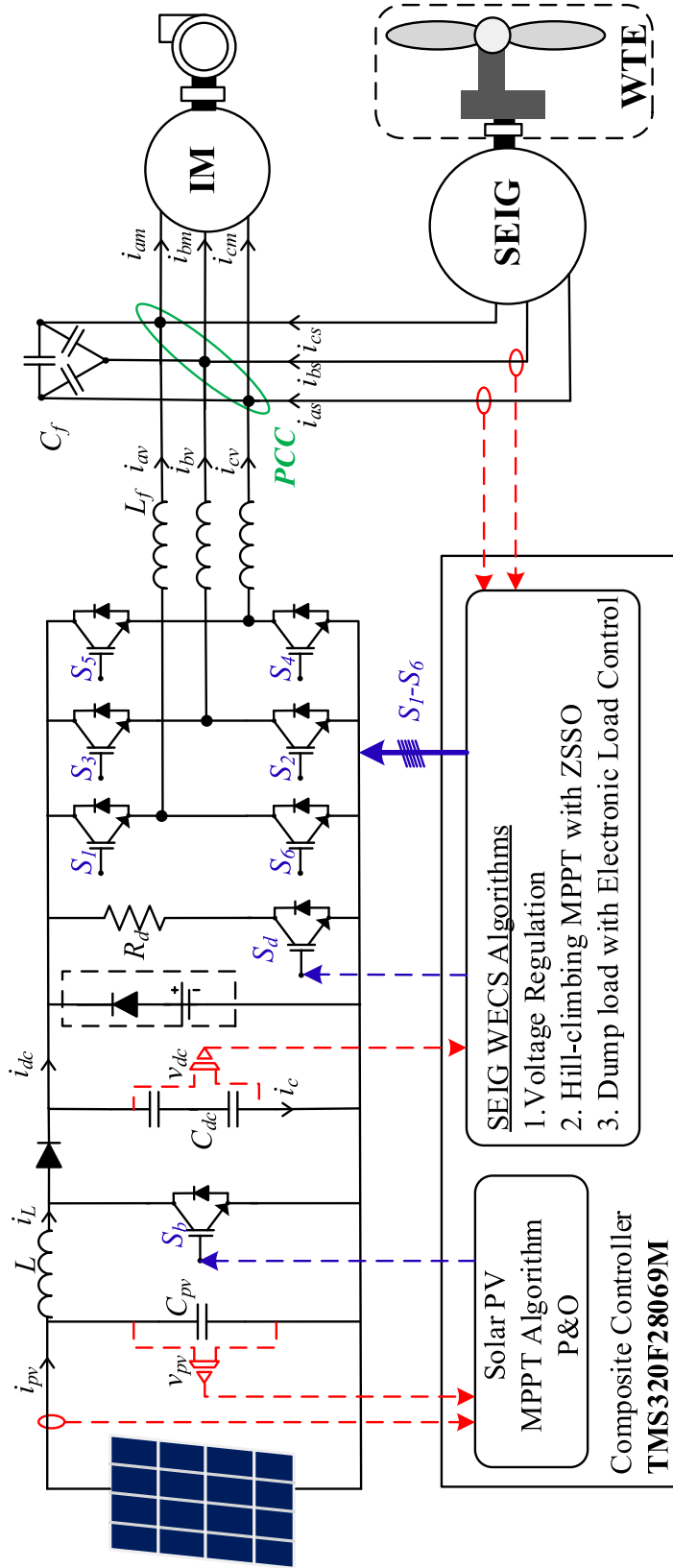


Figure 5.1: Circuit diagram of proposed stand-alone hybrid Wind-PV based water pumping system

5.3 Mathematical Modeling

The mathematical inter-relationships between various subsystems and their variables are shown in Figure 5.2. The equations describing each of these subsystems have been presented in section 2.4 and section 3.3 in detail and are omitted in this chapter for brevity.

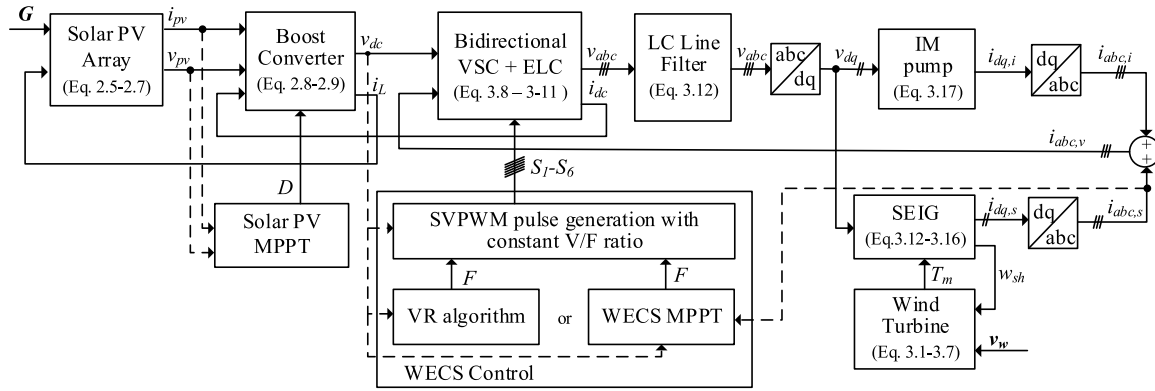


Figure 5.2: Mathematical model of the hybrid Wind-PV WPS

5.4 Composite Controller Framework and Operation

This section presents the detailed structure, implementation and working of the proposed composite controller for hybrid Wind-PV WPS. In this study, two power converters are used for power conditioning, a boost converter is employed in a solar PV system and a bidirectional VSC is used in WECS. For the entire operating range, the boost converter is driven by the P&O algorithm. The VSC used in WECS is responsible for multiple functions like driving IM pump, active and reactive power management at the PCC, v_{dc} regulation and WECS MPPT. Two control algorithms are selectively exercised for WECS to drive the VSC, one for the v_{dc} regulation using a PI controller and another for MPPT using a hill-climbing algorithm with Zero Steady-State Oscillation (ZSSO). Decisively an EMS is suggested for the hybrid Wind-PV system for optimal energy extraction from renewable sources. The decomposition of the proposed system yields a solar PV system and the WECS. The control strategy for each of these systems is discussed to explain the operation of the low-complex

composite controller for the overall system shown in Figure 5.3.

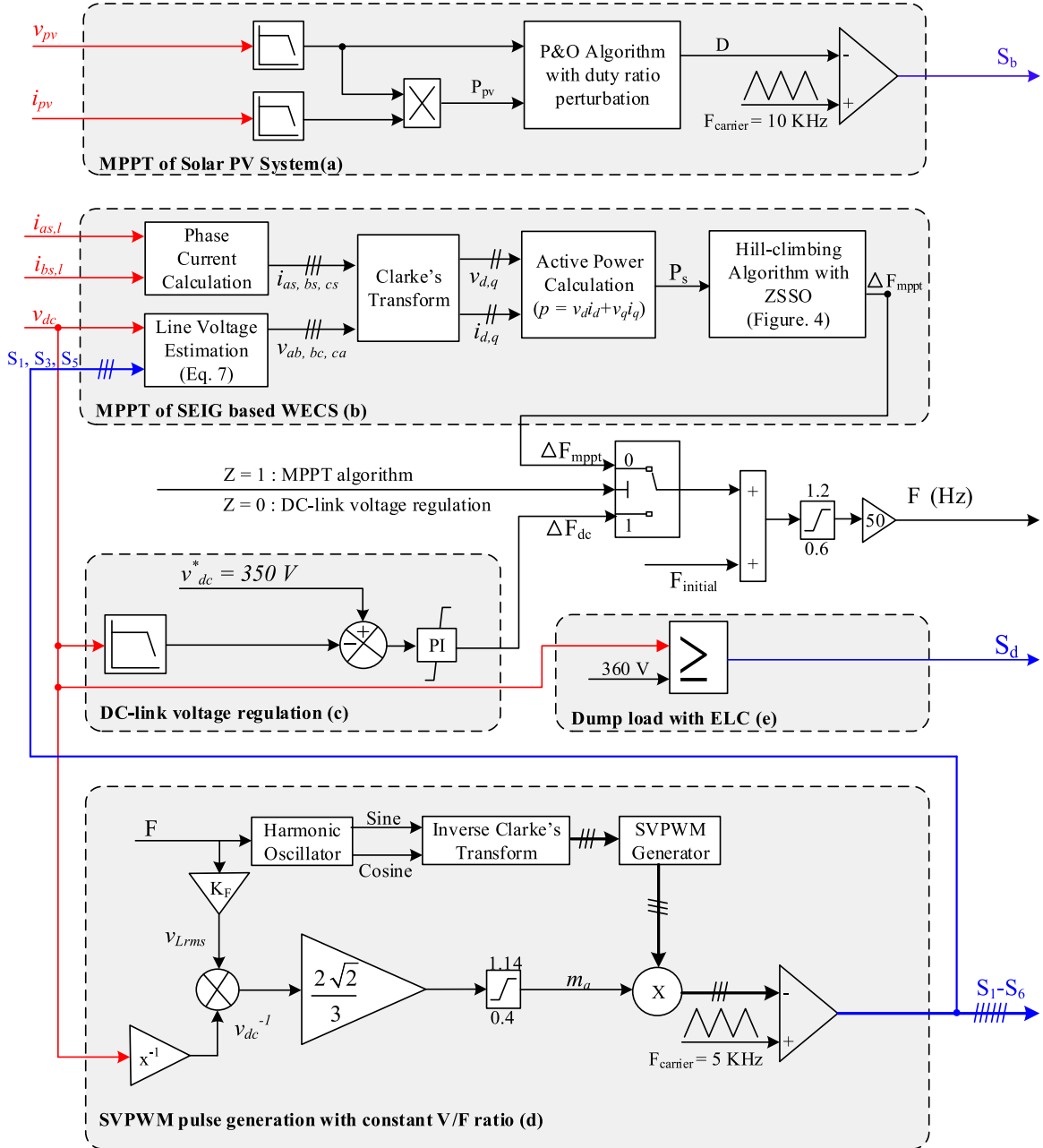


Figure 5.3: Structure of proposed composite controller implementation for the hybrid Wind-PV WPS

5.4.1 Control Strategy for Solar PV system

The Solar PV system consists of a boost converter and a 300 W PV array. A P&O algorithm with duty ratio (D) perturbation is employed to ensure MPPT (Elgendy et al., 2011). Additionally, this subsystem is also expected to boost the v_{pv} to match the v_{dc} (350-360 V). The theoretical value of duty ratio corresponding to maximum power point (D_{mpp}) for a solar PV system with a boost converter is given by (Ayop and Tan, 2018).

$$D_{mpp} = 1 - \sqrt{\frac{R_{mpp}}{R_L(F)}} \quad (5.1)$$

where, $R_{mpp} = v_{mpp}/i_{mpp}$; F is the operating frequency of the VSC.

For any variation in G , P_{pv} and R_{mpp} exhibit proportional and inverse variation, respectively. Furthermore, the load ($R_L(F)$) is VSC fed induction motor pump, which is dependent on the F . Hence, as G varies, the $R_L(F)$ is varied accordingly to ensure maximum power extraction from the solar PV array while maintaining the v_{dc} constant. Conclusively from equation 5.1, the D for varying G remains effectively constant as disturbances caused by changes in G are rejected by adjusting $R_L(F)$.

5.4.2 Control Strategies for SEIG based WECS

The SEIG based variable-speed WECS mainly consists of VSC, a dump load with ELC and the IM pump load. The SEIG, the IM pump and the VSC are connected in parallel to form the PCC. The change in v_w is considered a disturbance to this system, causing variations in input power to the SEIG. Two algorithms are formulated for the stand-alone WECS, one to regulate v_{dc} and another for MPPT.

5.4.2.1 DC-link Voltage Regulation (VR) Algorithm

The objective of this control algorithm is to regulate the value of v_{dc} to pre-defined reference (350 V). The varying v_w and load are considered as disturbances against which the v_{dc} is regulated. In the case of a hybrid Wind-PV system, the algorithm treats solar PV power pumped into DC-link also as disturbance and acts accordingly. The detailed implementation of this algorithm is presented in section 3.4 and is omitted here for brevity.

It is noteworthy that the suggested algorithm for voltage regulation uses only v_{dc} information reducing the system complexity and the cost.

5.4.2.2 Hill-Climbing MPPT Algorithm with ZSSO

This section presents the hill-climbing MPPT algorithm with ZSSO, which is an improvisation to the algorithm discussed in chapter 4. The proposition eliminates redundant oscillations on the arrival of MPP, thus increasing the steady-state power extraction from the WECS.

In SEIG based WECS under consideration, the w_{sh} varies directly as the F . Hence F is chosen as a control variable for the hill-climbing algorithm. Figure 5.3 (b) illustrates the block level implementation of the hill-climbing algorithm. Two SEIG line currents and v_{dc} are used to compute maximum power point. The line voltages required for power computation are estimated using equation 3.8. These acquired line currents and estimated line voltages are subjected to Clarke's transformation to obtain dq axis voltages and currents. The SEIG's dynamic, active power is computed using equation 4.2. This computed active power (P_s) is given as input to the hill-climbing algorithm, which yields F corresponding to optimal C_p for a given v_w achieving MPPT.

In addition to MPP tracking employing hill-climbing operation, the proposed algorithm offers steady-state averaging by eliminating redundant oscillations, which otherwise could lead to reduced energy utilization. The arrival of maximum power point is identified by continuously polling the slope $S[K]$ and its previous value $S[K-1]$. Consecutive toggles of 'S' are an indication of the steady-state of the MPPT algorithm. The number of toggles (N) can be customized to average steady-state oscillations. Further, an appropriate change in active power (dP) due to wind velocity variation can be set as tolerance (E) by the user to initiate the tracking process again.

Figure 5.4 illustrates the control logic of the hill-climbing algorithm with ZSSO. The flowchart consists of the hill-climbing algorithm logic and steady-state averaging section in particular. The steady-state averaging section determines if the MPP is reached and halts the MPPT until a considerable change in v_w is encountered. This process of steady-state averaging eliminates the oscillations near MPP and increases the energy extraction (Paz and Ordonez, 2014). The F computed by hill-climbing algorithm is fed to SVPWM pulse generation for the generation of switching pulses ($S_1 - S_6$) to be applied to the VSC.

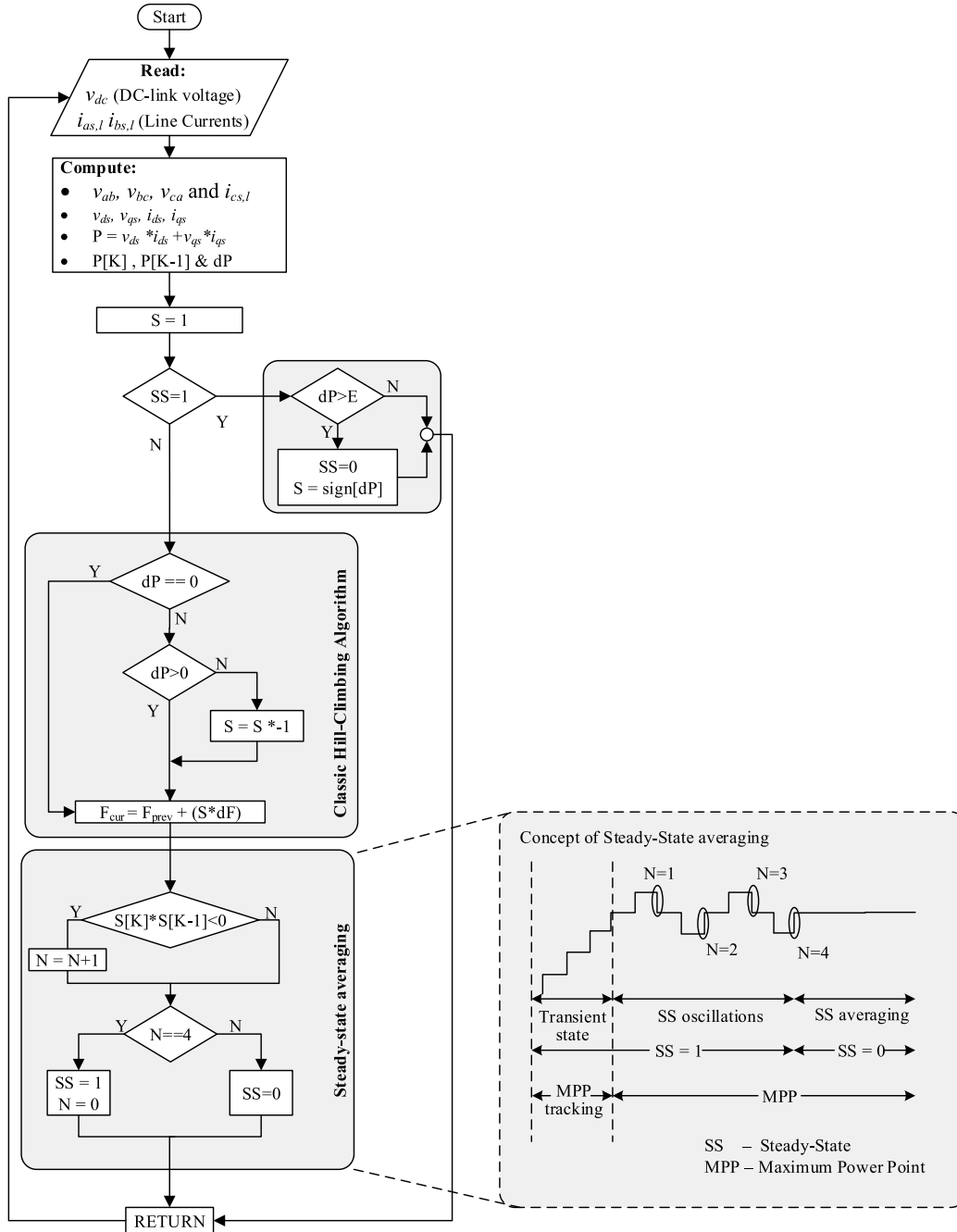


Figure 5.4: Proposed hill-climbing MPPT algorithm with ZSSO for SEIG based WECS

5.4.2.3 SVPWM pulse generation with constant 'V/F' ratio.

The WECS algorithms discussed in section 5.4.2.1 and 5.4.2.2 provide F as the output. This F is taken as input by the SVPWM pulse generation block to produce pulses

required ($S_1 - S_6$) by the VSC. In this study, the SEIG and the IM pump used are three-phase squirrel cage induction machine. These machines draw high magnetizing current if the operating flux is not maintained constant. Hence, to ensure constant flux operation in these machines, a variable voltage variable frequency supply at the PCC is made available by maintaining the ‘V/F’ ratio constant for the entire operating range.

The implementation of the constant ‘V/F’ algorithm is shown in Figure 5.3.(d). It consists of the harmonic oscillator, which generates the unit orthogonal sinusoidal voltages (sine and cosine) for given F . Inverse Clarke’s transformation is used to obtain three sinusoids using the unit orthogonal sinusoids. Three Space Vector Pulse Width Modulated (SVPWM) signals are generated by injecting the third harmonic into the three sinusoids obtained using inverse Clarke transformation. The SVPWM sinusoids are multiplied with amplitude modulation index (m_a) which is calculated using equation 5.2 (Mohan et al., 2003). These weighted SVPWM sinusoids are compared with high frequency carrier signal to obtain the required pulses $S_1 - S_6$.

$$m_a = \frac{V_{Lrms}}{v_{dc}} \cdot \frac{2 \cdot \sqrt{2}}{\sqrt{3}} \quad (5.2)$$

From the Figure 5.3.(d) and equation 5.2, it is evident that the value of v_{dc} is monitored at all instants to ensure constant ‘V/F’ ratio even against variation in v_{dc} .

5.4.3 Dump-load with ELC

The dump-load with ELC consists of a resistor and a series switch connected in parallel with the C_{dc} . Here, the C_{dc} acts as a reservoir for the storage of active power generated by both the solar PV and the WECS. If the cumulative generated power is more than the rated load, then the excess active power is absorbed by this dump-load which is electronically controlled by ELC. A boolean controller is employed in this study to realize ELC given by

$$S_d = \begin{cases} 1 & \text{if } v_{dc} > 360V \\ 0 & \text{if } v_{dc} < 360V \end{cases} \quad (5.3)$$

The dump load is designed to absorb rated active power capacity of solar PV (300 W) and the WECS (≈ 600 W) to ensure system safety under sudden

disconnection of the load and light-load conditions.

5.4.4 Composite controller for hybrid Wind-PV WPS

The overall structure of the composite controller for hybrid Wind-PV WPS is shown in Figure 5.3. It offers the P&O algorithm for a solar PV system and two algorithms for WECS, one for voltage regulation and another for MPPT. An informed decision about the combination of these algorithms for real-time implementation is possible by assessing their merits and demerits. Furthermore, due to two renewable energy sources, directions for cumulative active power generation and its allocation to the load are essential. Hence, in the following section, a simple energy management strategy is discussed for the system's coherent operation, revealing attributes of each algorithm for WECS in particular.

5.5 Energy Management Strategy

In this section, the Energy Management Strategy (EMS) employed for the proposed system's operation is illustrated. The solar PV and wind energy, are renewable sources in the system. These renewables are highly stochastic and hence for the orderly functioning of this complex system, EMS is crucial (Merabet et al., 2016, Campos et al., 2020).

5.5.1 Proposed Energy Management Strategy

The EMS's primary objective is to ensure seamless transfer of generated active power to the IM pump and divert the surplus power to the dump load. Secondly, EMS ensures the system's stability by shedding load during inadequate generation from both the renewables. Figure 5.5 unveils the flowchart describing the EMS employed in this study. In addition to the management of active power generated by the solar PV and the SEIG, the m_a is continuously monitored to ensure the stable DC-link voltage, which indirectly represents the hybrid system's stability. Based on the availability of the active power, the EMS suggests the following three modes of operation for the system under consideration:

- *Mode 0* : The cumulative active power generation ($P_h = P_{pv} + P_s$) is more than

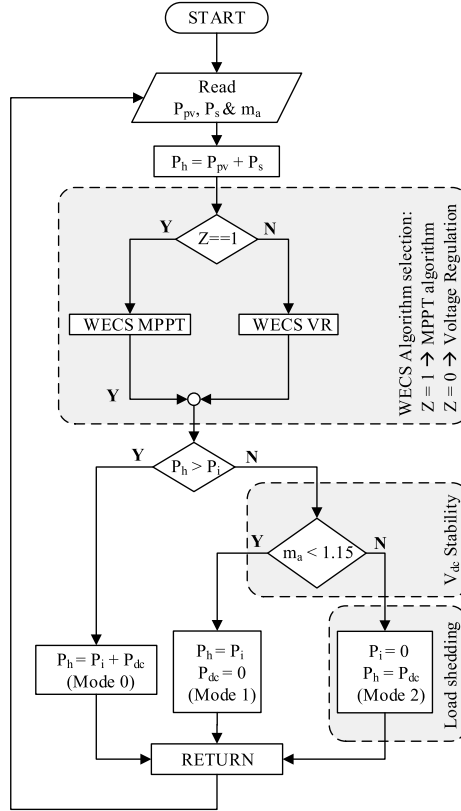


Figure 5.5: Flowchart of Energy management strategy

power requirement of the load (P_i). Hence the surplus power is diverted to the dump load (P_{dc}) using ELC.

- *Mode 1* : The cumulative active power generation ($P_h = P_{pv} + P_s$) is equal to the power requirement of the load (P_{IM}). Hence no power is diverted to the dump load. This mode of operation demonstrates the priority in the load allotment (P_i is preferred to P_{dc}).
- *Mode 2* : The cumulative active power generation ($P_h = P_{pv} + P_s$) is less than power requirement of the load (P_i). Hence the active load (IM pump) is disconnected and the generated power is diverted to the load. This mode of operation demonstrates the priority of system stability to load allocation.

The EMS is designed to continuously feed the cumulative active power to the load while ensuring system stability at all times.

5.5.2 Choice of Algorithm for SEIG based WECS

The boost converter fed by solar PV array in hybrid Wind-PV system always runs at the MPP employing P&O algorithm. However, the SEIG based VSC assisted WECS can be run either using the VR algorithm or the hill-climbing MPPT algorithm with ZSSO. The choice between two algorithms is governed by preferences offered by these algorithms and are explained as follows:

5.5.2.1 Voltage Regulation (VR) Algorithm

The details of VR algorithm are discussed in section 5.4.2.1. The control variable (F) in this algorithm is governed by equation 3.20 and is influenced by G and v_w . Any active power contribution from P_{pv} to DC-link capacitor results in a change in F , thus causing C_p to deviate from its theoretical maximum (0.48). This leads to a reduced P_s for a given v_w . The deviation in C_p is found to increase with higher penetration of P_{pv} into the DC-link capacitor. The merits of this algorithm are two-fold, Firstly the v_{dc} is regulated at 350 V for any variations in v_w , G and load. Further, for a given v_w and G , more power is transferred to the IM pump than the hill-climbing MPPT algorithm. In other words, if VR algorithm is chosen for WECS, then the hybrid Wind-PV WPS predominantly operates in Mode 1.

5.5.2.2 Hill-climbing MPPT algorithm

The implementation of hill-climbing MPPT algorithm is shown in Figure 5.4 and is discussed in section 5.4.2.2. In this algorithm, F corresponding to optimal C_p is tracked continuously for changes in v_w . Even in hybrid wind-PV mode of operation, any active power changes due to variation in G will be diverted to v_{dc} and dump load. Hence C_p in this algorithm is independent of G and is governed by v_w alone. This algorithm will ensure optimal C_p hence maximum power extraction for given v_w . Any surplus generation in hybrid mode of operation, is diverted to the dump load. Simply put, if WECS functions with MPPT algorithm, then the hybrid Wind-PV WPS will substantially operate in Mode 0.

5.5.2.3 Suggestions

If the preference in the hybrid Wind-PV mode of operation is transferring more power to the IM pump, then VR algorithm has to be used. On the contrary, if the priority

is maximum power extraction from both the renewables, then hill-climbing algorithm has to be employed. Further, if sizing of P_{pv} in hybrid wind-PV configuration is large, then hill-climbing algorithm has to be employed because the VR algorithm will result in lower C_p leading to reduced efficiency of the WECS.

5.6 Simulation and Experimental study

In this section, simulation and experimentation results are presented to prove the viability of the low-complex composite controller for hybrid Wind-PV WPS. In the present study, a 300 W solar PV array is integrated with 1.5 HP SEIG-based WECS to configure a hybrid Wind-PV WPS. The 300 W solar PV array is obtained by connecting six solar PV modules in series whose parameters are defined in Table A.1. The details of induction machines used for SEIG and IM pump are provided in Table A.2. Lastly, the experimental prototype developed to obtain test results is discussed in appendix B.3.

5.6.1 Simulation Results

The v_w and G profile used for simulation is shown in Figure 5.6 (a). The perturbations are orderly introduced to demonstrate different modes of operation for the system under consideration. For the entire operating range, the boost converter is controlled using simple P&O algorithm to extract maximum power from the solar PV array. Performance of two control algorithms for SEIG based WECS is demonstrated, namely, hill-climbing MPPT algorithm with ZSSO from $t = 0 - 20$ s and a Voltage Regulation (VR) algorithm from $t = 20 - 40$ s. In the present study, the SEIG, IM pump and the bidirectional VSC are connected in parallel at the PCC. Both SEIG and the IM pump are rated for 230 V and 50 Hz. To facilitate this required line-line voltage at PCC, v_{dc} is maintained in the range of 350-360 V.

Figure 5.6 (c) shows the response of v_{dc} for the entire operating range. At $t = 0$ s, the self excitation of the SEIG is initiated, A 12 V battery in parallel with C_{dc} provides the initial reactive power for the voltage build-up process. The IM pump is inserted into the system at $t = 2$ s. A momentary dip in v_{dc} is observed, attributed to large active and reactive power requirements during the starting of the IM pump. For hill-climbing MPPT algorithm with ZSSO ($t = 0-20$ s), v_{dc} is maintained at a

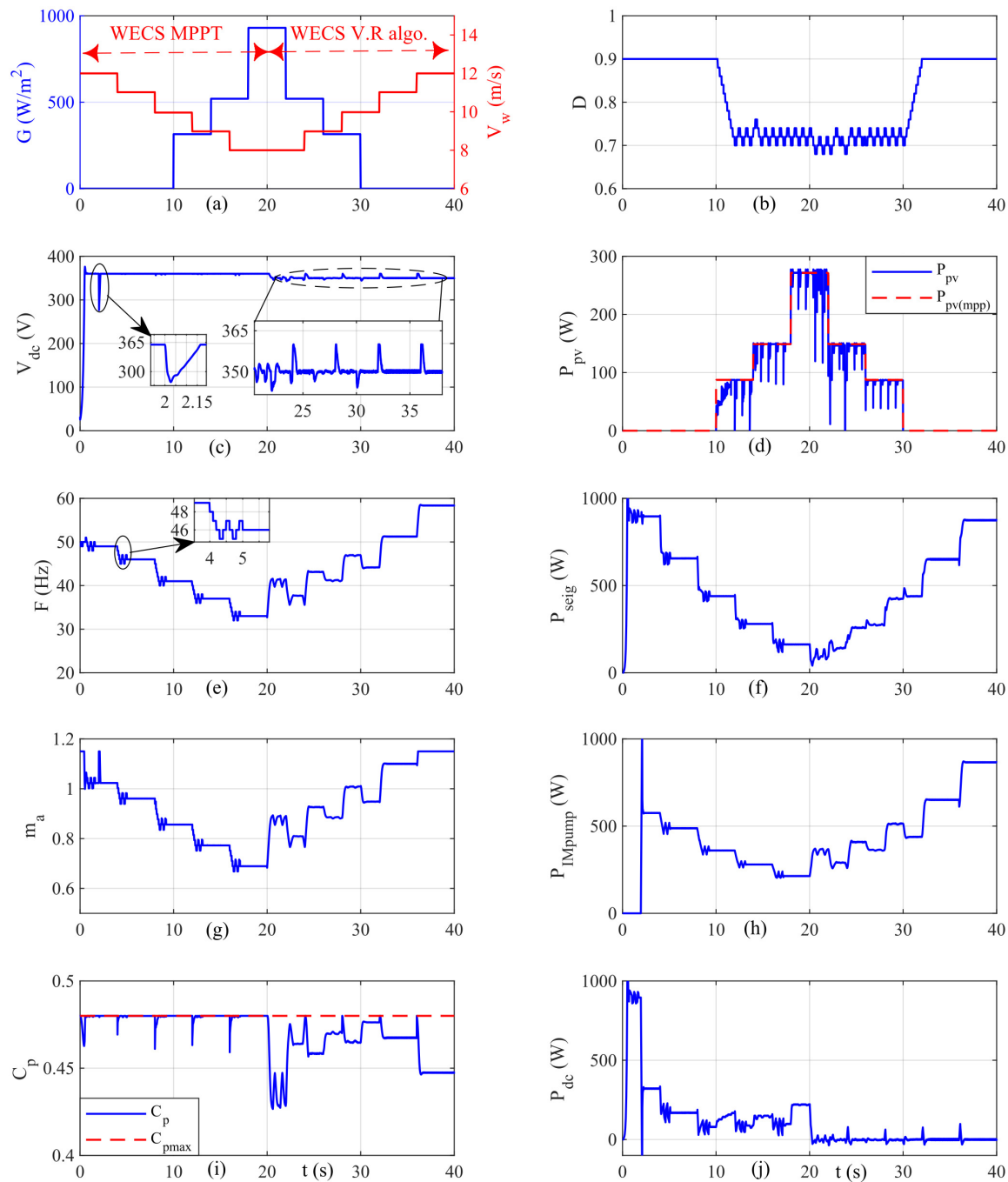


Figure 5.6: Simulation Results: (a) Solar irradiance and wind velocity profile, (b) Duty ratio of boost converter, (c) DC-link voltage, (d) Solar PV power, (e) Operating frequency of the VSC, (f) SEIG active power, (g) Amplitude modulation index of the VSC, (h) IM pump active power, (i) Wind power coefficient, (j) Dump load active power

value of 360 V and for VR algorithm ($t = 20-40$ s), the v_{dc} is regulated at 350 V. In both algorithms, F of the VSC is employed as the control variable. This F is obtained as indicated in Figure 5.4 in hill-climbing algorithm and in case of VR algorithm it is governed by (3.20). The variation of v_{dc} and the control variable F for the entire operating range is shown in Figure 5.6 (c) and (e) respectively. The m_a captured in Figure 5.6 (g) is designed to vary in accordance with F to maintain constant ‘V/F’ ratio (4.6, with $v_{rated} = 230$ V and $F_{rated} = 50$ Hz) at PCC to prevent saturation issues in SEIG and IM pump.

Figure 5.6 (i) shows the plot of C_p for variations in v_w , G and the load along with its theoretical maximum (0.48). It is obvious from the waveform that the efficiency of the WECS is better for hill-climbing algorithm ($t = 0 - 20$ s) compared to VR algorithm ($t = 20 - 40$ s). This can be apprehended to the characteristic of the algorithms. The hill-climbing algorithm decides F output based on changes in v_w alone. Hence the resulting ω_{sh} yields optimal λ forcing C_p to settle for 0.48 for every change in v_w . On the contrary, the VR algorithm monitors v_{dc} and varies F governed by (3.20). Hence the F varies for any changes in either v_w or G . Furthermore, for given v_w , if a large change in G is encountered, this results in proportional change in F . The F influences the tip-speed ratio (λ) which in turn governs C_p . Hence VR algorithm suffers inferior C_p comparatively.

Figure 5.6 (b) shows another control variable D , which oscillates around MPP to ensure maximum power extraction from the solar PV array against variations in G . The P_{pv} and its theoretical maximum are shown in Figure 5.6 (d), proving the efficacy of the solar PV system in this hybrid Wind-PV configuration.

Figure 5.6 (d) and (f) represent the active power generation by solar PV system and SEIG respectively and that of Figure 5.6 (h) and (j) shows the active power consumption by the IM pump and the dump load respectively. At all operating points, it is observed that the cumulative active power generation by the solar PV system and SEIG equals the cumulative power consumption by the IM pump and the dump load.

5.6.2 Experimental Results

The details of the laboratory prototype developed for experimentation is presented in appendix B.3. The test results are obtained for the same set of perturbations

presented in Figure 5.6 (a). The behavior of v_{dc} , F , m_a and D can be explained similar to discussions presented in section 5.6.1.

Figure 5.7 shows the behaviour of v_{dc} for hill-climbing MPPT with ZSSO and VR algorithm of WECS. It is evident from the waveform that the v_{dc} is maintained at 360 V with aid of ELC unit ($t = 0 - 20$ s). For VR algorithm of the WECS, it is regulated at a value of 350 V against variations in G and v_w ($t = 20 - 40$ s). The stable v_{dc} for the entire operating range is indication of system stability for all the disturbances considered for the investigation.

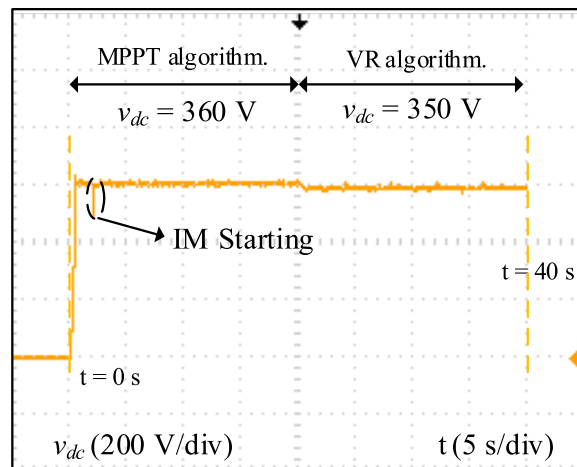


Figure 5.7: DC link Voltage

The response of F and m_a are captured in Figure 5.8 which reveals MPPT in compliance with the algorithm discussed in section 5.4.2.2 for $t = 0 - 20$ s. The oscillations around MPP and its steady-state averaging are also clearly depicted. Further, careful observation of ' F ' reveals the tracking time of the algorithm to be equal to 5-6 sampling instants (≈ 0.5 s - 0.6 s) for step change in v_w of 1 m/s. Secondly, to regulate the v_{dc} to 350 V from $t = 20 - 40$ s, F varies for changes in G and v_w as governed by equation (3.20). The m_a varies in accordance with changes in F to maintain constant ' V/F ' ratio at the PCC.

Figure 5.9 shows the response of control variable (D) of the solar PV system. From the waveform, it is apparent that the D oscillates around MPP of solar PV array from $t = 10 - 30$ s which indicates that the solar PV system always works at the MPP employing P&O algorithm in this hybrid Wind-PV configuration. Further, during MPPT, the constant steady state value of D for varying G and v_w is justified by discussions presented in 5.4.1.

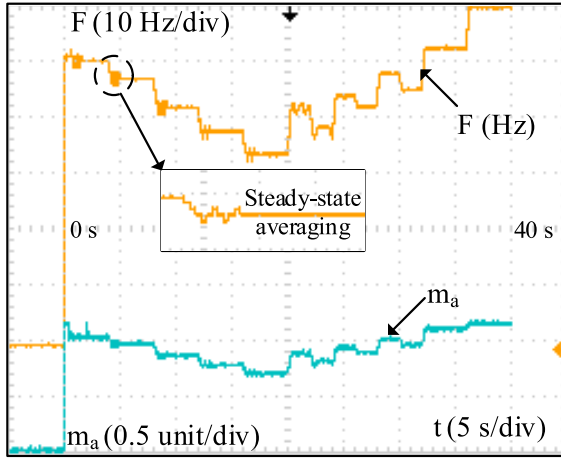


Figure 5.8: Frequency and amplitude modulation index

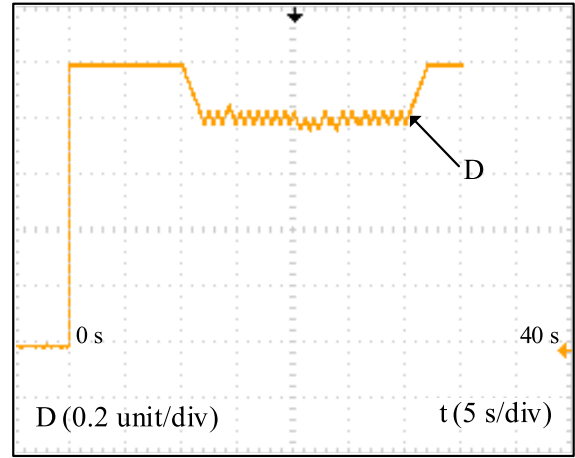


Figure 5.9: Duty ratio of the boost converter

The dynamic and steady-state behavior of the line currents of the SEIG, VSC and the IM pump along with the line voltages at PCC are shown in Figure 5.10 (a) - (h). Following noteworthy observations can be made from the inspection of these waveforms:

1. The currents of the SEIG, VSC and the IM pump are within the permissible limits of the machines and the VSC for entire operating range including crucial disturbances like starting of the SEIG and IM pump.
2. At PCC, for all instants, $i_{abc(v)} = i_{abc(s)} + i_{abc(i)}$.
3. The magnitude of the $V_{L,PCC}$ varies in accordance with frequency to ensure constant 'V/F' ratio at the PCC. This helps in preventing saturation issues in the SEIG and the IM pump.
4. By virtue of the line filter (section 3.3.3) employed in the study, the $V_{L,PCC}$ and all the system currents are quasi sinusoidal. These balanced sinusoidal system voltages and currents add to the increased stability and life expectancy of the overall system.

Finally, to substantiate the power balance at the PCC in the hybrid Wind-PV configuration, the steady-state active and reactive power of the SEIG, IM pump and the dump load (VSC) are measured using MECO 3510PHW (clamp-on true RMS

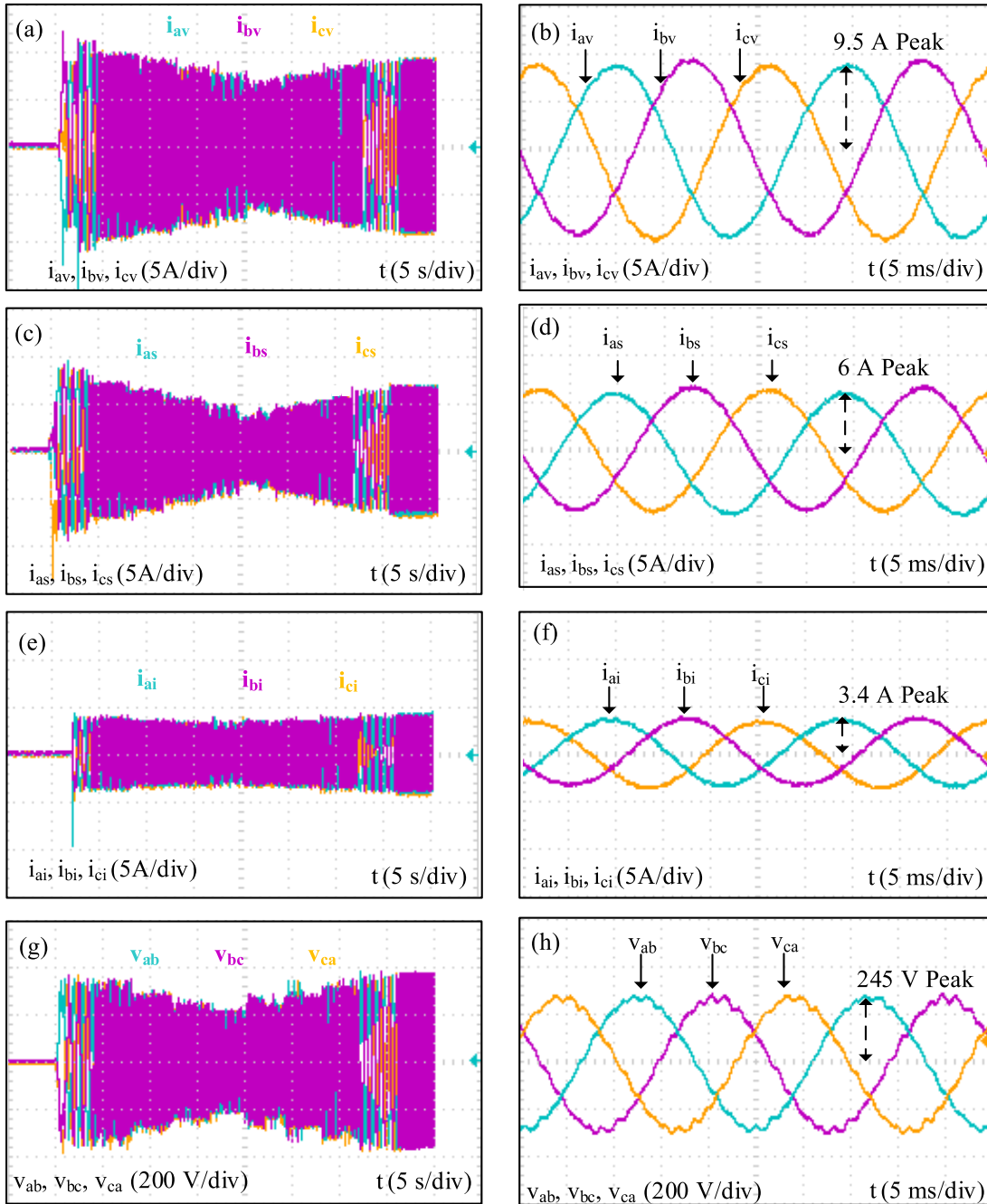


Figure 5.10: Dynamic behavior of system currents and voltages for proposed composite controller: (a) VSC currents, (c) SEIG currents, (e) IM pump currents and (g) Line voltages at PCC for entire operating range ($t = 0 - 40$ s); Steady-state behavior of system currents and voltages for $F = 40$ Hz : (b) VSC currents, (d) SEIG currents, (f) IM pump currents and (h) Line voltages at PCC

power meter) and that of active power generated by solar PV system is recorded using Solar Magna emulator. The active and reactive power flow for all the perturbations are summarized in Table 5.1. It is apparent from the data presented that the cumulative sum of active power generated by solar PV system and the SEIG cater to the effective load and losses of the system ($P_s + P_{pv} = P_i + P_{dc} + P_{loss}$) and that of reactive power requirement in the system is fulfilled by the DC-link capacitor of the VSC ($Q_{vsc} = Q_{seig} + Q_{im}$).

Table 5.1: Steady-state active and reactive power recorded at every interval for entire operating range (t = 0-40 s)

Interval S.No (time)	V_w (m/s)	G (W/m ²)	Ppv (W)	Ps (W)	Pi (W)	Pdc (W)	Qvsc (VAR)	Qseig (VAR)	Qim (VAR)
1 (0-2 s)	12	0	0	895	0	881	1891	1874	0
2 (2-4 s)	12	0	0	895	544.2	313.8	2677	1854	812.8
3 (4-8 s)	11	0	0	656.5	461.2	154.5	2247	1469	776.5
4 (8-10 s)	10	0	0	438	332.4	73.26	1780	1116	661.5
5 (10-12 s)	10	290	87.43	438	340.4	141.6	1780	1111	661.5
6 (12-14 s)	9	290	87.43	279.6	252.8	71.74	1433	832	595
7 (14-16 s)	9	540	149	279.6	251.8	130.8	1433	837	595
8 (16-18 s)	8	540	149	161.7	181.8	82.46	1107	589.7	509.8
9 (18-20 s)	8	950	277	161.7	193.8	203.7	1107	588.4	509.8
10 (20-22 s)	8	950	277	77	323.2	0	1423	765.9	648.3
11 (22-24 s)	8	540	148.5	140	234.4	0	1352	757.4	587
12 (24-26 s)	9	540	148.5	255.6	374.3	0	1654	964.7	680.4
13 (26-28 s)	9	290	86.7	277.6	331.2	0	1640	987	648.2
14 (28-30 s)	10	290	86.7	423.1	481.1	0	2053	1257	786.9
15 (30-32 s)	10	0	0	439.8	404.8	0	2038	1292	739.2
16 (32-36 s)	11	0	0	650.1	639.8	0	2466	1582	880.6
17 (36-40 s)	12	0	0	876.3	858.1	0	2635	1781	849.2

5.7 Comparative analysis

In the present study, to substantiate the merits of the proposed composite controller, a comparative analysis is performed with other similar controllers for hybrid wind-PV WPS. The brief details of the comparison is presented in Table 5.2.

According to Table 5.2, the system feeding DC motor pump requires least power electronic interface, resulting in low cost, size, and complexity (de Oliveira Ferreira et al., 2020). The majority of hybrid Wind-PV WPS have proposed AC motors for

water pumping owing to their merits (Priyadarshi et al., 2020, Femi et al., 2021, Mezghani et al., 2020, Gholamshahi et al., 2019). Among these studies, some researchers have suggested three (Femi et al., 2021) and four (Priyadarshi et al., 2020, Mezghani et al., 2020) power converters for power conditioning and PMSG for WECS leading to increased system cost and complexity. One of the investigations using an AC motor pump is reported to use only two power converters for power conditioning employing SEIG as wind generator (Gholamshahi et al., 2019). However, this study reports limitations such as using nine sensors for control algorithms besides compromising on MPPT of WECS.

It is worth mentioning that the proposed system employs just two power converters and SEIG based WECS with MPPT capability for both renewables. Furthermore, to achieve MPPT, it uses only current and voltage sensors, making the scheme speed sensorless and system parameter independent. Because the suggested system includes only two power converters and employs simple control strategies, the design emerges to be less complex and low-cost compared to other similar controllers for hybrid Wind-PV WPS.

Table 5.2: Comparison of available controllers with proposed composite controller for hybrid Wind-PV water pumping system

Parameter \ Reference	1	2	3	4	5	Proposed
Motor pump used	DC Motor	IM	BLDC	IM	IM	IM
Wind generator used	PMSG	PMSG	PMSG	PMSG	SEIG	SEIG
Power converter count	One	Four	Three	Four	Two	Two
Sensor count	Four	Four	Three	Nine	Nine	Five
MPPT for Solar PV	Yes	Yes	Yes	Yes	Yes	Yes
MPPT for WECS	Yes	Yes	No	Yes	No	Yes
Knowledge of system parameter	No	Yes	Yes	No	Yes	No
Speed sensorless algorithms	No	Yes	No	Yes	No	Yes
Complexity	Low	Moderate	Complex	Complex	Moderate	Low
Cost	Low	High	High	Moderate	Moderate	Low
Controller	–	Dspace	DSP	Arduino	–	DSP

1. (de Oliveira Ferreira et al., 2020)
2. (Priyadarshi et al., 2020)
3. (Femi et al., 2021)
4. (Mezghani et al., 2020)
5. (Gholamshahi et al., 2019)

Chapter 6

Conclusions and Future Scope

6.1 Conclusions

In the coming days, the paradigm shift in using renewable energy to pump water is inevitable for a sustainable future. It was learned from an extensive literature review that vital contributions are already made in SPWPS. However, there is scope to propose new systems with reduced part count and control strategies to utilize wind energy and hybrid Wind-PV energy sources effectively for water pumping application. On this line, the primary objective of this research work is formulated as effective operation and control of hybrid Wind-PV WPS with minimal power electronics interface employing low-complex composite controller and reduced sensor set. This problem statement fragments into four objectives that the thesis has answered in chapters 2 through 5. The chapter wise conclusions of these objectives will be deliberated in this section.

In Chapter 2, the effects of system parameters (input capacitance, the cut-off frequency of the digital filter and the sampling time) on the solar photovoltaic system's performance with the perturbation-based MPPT technique are investigated. First, two simple step tests are recommended to determine the effective system time constant of the solar PV system eluding the need to obtain small-signal model of the system. Then, based on the estimated system time constant, comprehensive guidelines for choice of optimal sampling time are suggested. Finally, simulation and experimental results of solar PV fed boost converter with P&O algorithm revealed the significance of the optimal sampling time in experimentation due to nonidealities and noise added during ADC of sensed variables. It is noteworthy that the work presented in this

chapter is comprehensive and can be easily extended to any other converter, load and perturbation-based MPPT algorithm.

In Chapter 3, investigations on the proposed voltage regulation algorithm with constant flux operation of the VSC assisted SEIG feeding IM pump have been carried out. Simulation studies revealed the successful variable frequency operation of the SEIG (including saturation effects), the VSC and the IM pump connected in parallel at the PCC (the AC terminals). Besides voltage regulation, the developed algorithm demonstrated the constant flux operation of the SEIG and the IM pump. The overall control strategy has been examined for various perturbations like the starting of the IM load, ELC on, ELC off, variations in load and wind velocities. Additionally, an exhaustive active and reactive power analysis has been performed to verify the power balance at the PCC. Experimental tests were carried out on 1.5 HP SEIG feeding 0.75 HP IM pump to validate claims of the simulation studies. Results of simulation and experimentation were found to be in close agreement proving the effectiveness of the system under test for a stand-alone application.

Chapter 4 proposes a speed sensorless hill-climbing MPPT algorithm for a single-stage SEIG-based WECS feeding an IM pump. A VSC is used for both power conditioning and maximum power extraction employing a reduced sensor set. The proposed algorithm has effectively maintained the power coefficient (C_p) of wind-turbine to an optimal value of 0.48 against wind velocity and load variations. The tracking time is reported to be approximately equal to 6-time constants (equal to 0.6 s in this study). To ensure the system's protection against light/no-load conditions/surplus generation, the dump load with ELC has been effective for all the perturbations. As a result, the system currents are limited below the permissible limits of the SEIG and the IM pump for the entire operating range. In addition to extracting maximum power from the wind turbine, the SEIG and the IM pump's constant flux operation has been ensured for increased efficiency and life expectancy of the overall system. Decisively, the system and the proposed algorithm's performance have been assessed using a laboratory prototype, proving the efficacy of the system and the proposed algorithm.

Chapter 5 proposes a simple and economical solution for a hybrid Wind-PV water pumping system by eliminating a dedicated power converter for WECS in particular. Formulation and implementation of the proposed composite controller, consisting of a P&O algorithm for a solar PV system and voltage regulation/ hill-climbing MPPT

algorithm with zero steady-state oscillations for WECS, has been illustrated. To increase the life expectancy of the overall system, constant flux operation of the IM pump and the SEIG for an entire operating range has been demonstrated while ensuring optimal energy extraction from both renewables. A suitable energy management strategy has been suggested to effectively transfer the cumulative active power generated to the load while ensuring system stability. Furthermore, comprehensive active and reactive power flow has been illustrated to prove the synergy between the solar PV and the WECS to maintain power balance at the PCC. A mathematical model has been developed by taking data from real machines to obtain insights into system dynamics and evaluate system performance. Results obtained via experiments are promising and indicate that the proposed system is an attractive and reliable solution for a stand-alone hybrid Wind-PV system owing to reduced cost, simple controls and optimal energy extraction using minimal power electronics interface and reduced sensor set.

6.2 Scope for Future Work

Based on the research carried out in this thesis, the recommendations for future research are as follows:

- Inclusion of appropriate sized batteries and design of energy management strategies can be considered to make the hybrid Wind-PV system truly autonomous.
- If the hybrid Wind-PV WPS is located near to the grid, then challenges concerning grid interfacing can be explored.
- The control strategies for other types of motor pumps namely PMSM and BLDCM in hybrid Wind-PV WPS can be explored.
- Investigations can be carried out to propose a novel converter with reduced part count which can integrate functionalities of DC-DC boost converter and bidirectional VSC.
- The effect of wind-turbine inertia on the overall performance of WECS is worth investigating to assess the operability and efficiency of the control algorithms.

Appendix A

System Attributes

This chapter presents the details of the system attributes used for simulation and experimental verification of contributions in Chapters 2 through 5, comprising of data pertaining to the solar PV array, electrical machines, and the wind turbine.

A.1 Solar PV array

The system parameters used to emulate solar PV module characteristics are taken of commercial 50 W PV module from WAREE and are listed in Table A.1. In the present study, the mathematical model of the solar PV module is suitably formulated to extend the module characteristics to obtain desired solar PV array characteristics.

Table A.1: Solar PV array specifications

System parameter	Value
Open circuit Voltage, (V_{OC})	21.47 V
Short circuit current, (I_{SC})	3.11 A
Voltage at Maximum Power, (V_{mp})	17.21 V
Current at Maximum Power, (I_{mp})	2.91 A
Module maximum power, (P_{mp})	50 W
Temperature coefficient of Current, (K_v)	0.0154 ($^{\circ}C/V$)
Temperature coefficient of Voltage, (K_i)	-0.2775 ($^{\circ}C/mA$)

A.2 Induction machine parameters

In this research work, two induction machines are used, one is configured as SEIG (1.5 HP) to extract power from the wind turbine and the other is used to emulate IM pump characteristics (0.8 HP). The machine parameters are obtained by conducting appropriate tests and are enlisted in Table A.2. An additional synchronous speed test on the 1.5 HP induction machine is performed to obtain the magnetization characteristics expressed as a sixth-order polynomial given by equation 3.15. The coefficients of this polynomial are enlisted in Table A.3

Table A.2: Electrical Machine specifications

Induction machine parameter	SEIG	IM pump
Type of connection	Δ	Δ
Power Rating (P)	1.5 HP	0.8 HP
Rated (L-L) RMS voltage (V_{LL_RMS})	230 V	230 V
Rated line current (I_{L_RMS})	3.82 A	2.42 A
Rated Frequency (F)	50 Hz	50 Hz
Stator Resistance (R_s)	6.8 Ω	13.228 Ω
Rotor Resistance (R_r)	5.2523 Ω	6.7024 Ω
Stator Leakage inductance (L_{ls})	25.57 mH	35 mH
Rotor Leakage inductance (L_{lr})	25.57 mH	35 mH
Pump constant (K_p)	–	141.9 $\mu\text{N}\cdot\text{m}/(\text{rad}/\text{s})^3$
Number of poles (P)	4	4
Moment of inertia (J)	0.06	0.02
Rated magnetizing inductance (L_m)	–	550 mH

Table A.3: Co-efficients of Magnetization Curve of 1.5 HP SEIG

Coefficients	Value
a_0	0.5943
a_1	0.5012
a_2	-1.089
a_3	1.1285
a_4	-.6382
a_5	0.01783
a_6	-0.0192

A.3 Wind-Turbine Characteristics

Wind turbine is characterized by non-dimensional power coefficient (C_p) as a function of tip-speed ratio (λ). The coefficients C_1 to C_6 used in equation 3.2 are enlisted in Table A.4.

Table A.4: Wind-Turbine Specifications

System parameter	Value
Blade Pitch angle, (β)	0
Air density, (ρ)	1.085
Radius of wind turbine blade, (r)	1.05 m
Gear Ratio, (GR)	1.85
Co-efficients ($C_1 - C_6$)	$C_1=0.5176$; $C_2=116$; $C_3=0.4$; $C_4=5$; $C_5=21$; $C_6=0.0068$;

Appendix B

Experimental Setup

This chapter describes the experimental setup used to obtain test results of all investigations carried out in this research work which consists of standalone solar PV system and SEIG based Wind Energy Conversion System (WECS).

B.1 Solar PV System

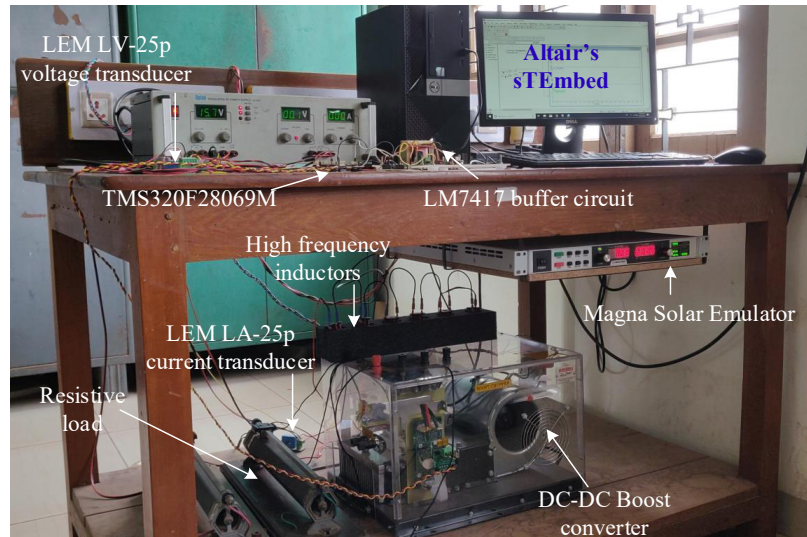


Figure B.1: Experimental setup of solar PV system

The solar PV system consists of a solar PV emulator, boost converter (Semikron make), high-frequency inductor, input capacitance and resistive load. This setup is used for conceptual validation of studies in Chapter 2. Figure B.1 shows the

Table B.1: Particulars of components used to develop laboratory prototype of solar PV fed boost converter

Component	Type/Value
IGBT Module	SKM 200 GB12E4
IGBT driver	SKYPER 32 Pro
Input capacitor	220 μF
Output Capacitor	2350 μF
Load resistor	120 Ω
Switching Frequency	10 kHz
Inductor	3 mH, coilcraft
Current Sensor	LA 25-P
Voltage sensor	LV 25-P
250 W Solar PV Array	Magna SL 300-5 Emulator

laboratory prototype of solar PV fed boost converter and the specifications of the components used in the setup are described in Table B.1. The system attributes used to emulate PV profiles using solar emulator are enlisted in Table A.1.

B.2 SEIG based WECS

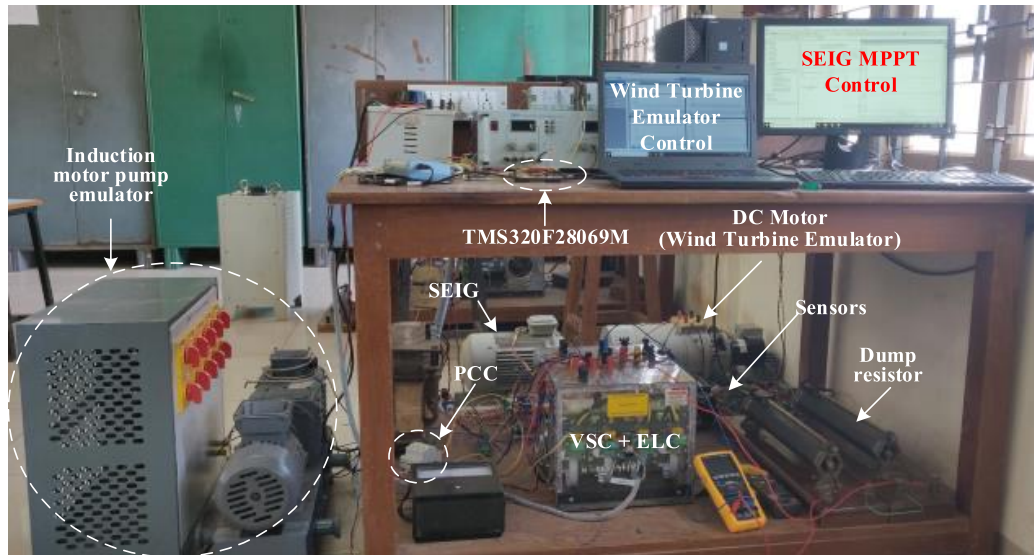


Figure B.2: Experimental setup of SEIG based WECS

Figure B.2 shows the experimental prototype of standalone SEIG-based WECS.

Table B.2: Particulars of components used to develop laboratory prototype of SEIG based WECS

Component	Type/Value
IGBT Module	SKM75GB12T4
IGBT driver	SKYPER 32 R
DC link Capacitor	2250 μF
Switching Frequency	5 kHz
Current Sensor	LA 25-P
Voltage sensor	LV 25-P
Filter inductance (L_f)	1 mH
Filter capacitance (C_f)	10 μF
Filter resistance R_f	1 Ω

It consists of armature current-controlled separately excited DC motor drive (wind-turbine emulator), three-phase SEIG, bidirectional Voltage Source Converter (VSC), dump load with Electronic Load Control (ELC) and a three-phase induction motor pump. The specifications of the wind turbine, the SEIG and the IM pump used for simulation and experimental study are enlisted in Appendix A and the particulars of hardware components are specified in Table B.2. This setup is utilized to obtain test results for verification of the DC-link voltage regulation algorithm and speed sensorless hill-climbing algorithm for SEIG based WECS in Chapter 3 and Chapter 4 respectively.

B.3 Hybrid Wind-PV Water Pumping System

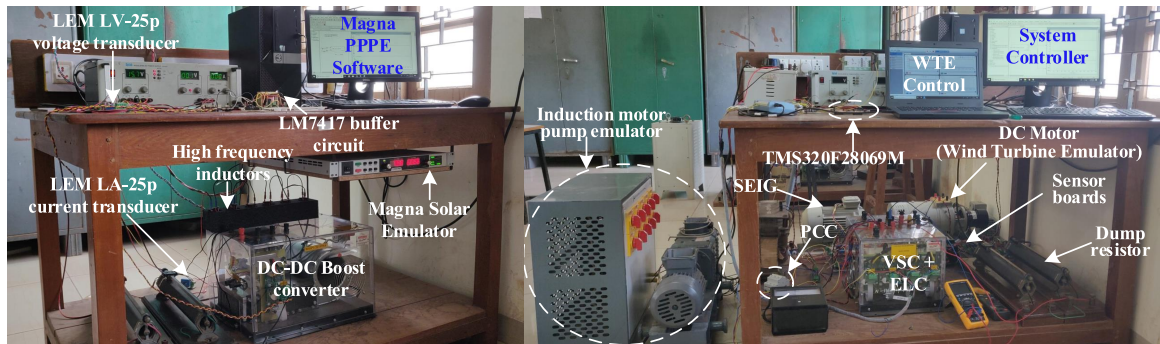


Figure B.3: Experimental setup of hybrid Wind-PV WPS

The experimental testbench for hybrid Wind-PV water pumping system shown in Figure B.3 is configured by integrating the solar PV system and SEIG-based WECS discussed in sections B.1 and B.2. This integrated experimental setup is employed to verify the operability of the low-complex composite controller for hybrid wind-PV WPS deliberated in Chapter 5.

B.4 Control Strategies: Model Based Design

All the control strategies of the research work carried out in this thesis are developed using Altair Embed and TMS320F28069M target hardware. Altair Embed is certified Model Based Design (MBD) software for developing control algorithms via automatic code generation facility and loading them to popular target hardware for the deployment or interactive simulation (Embed, 2021).

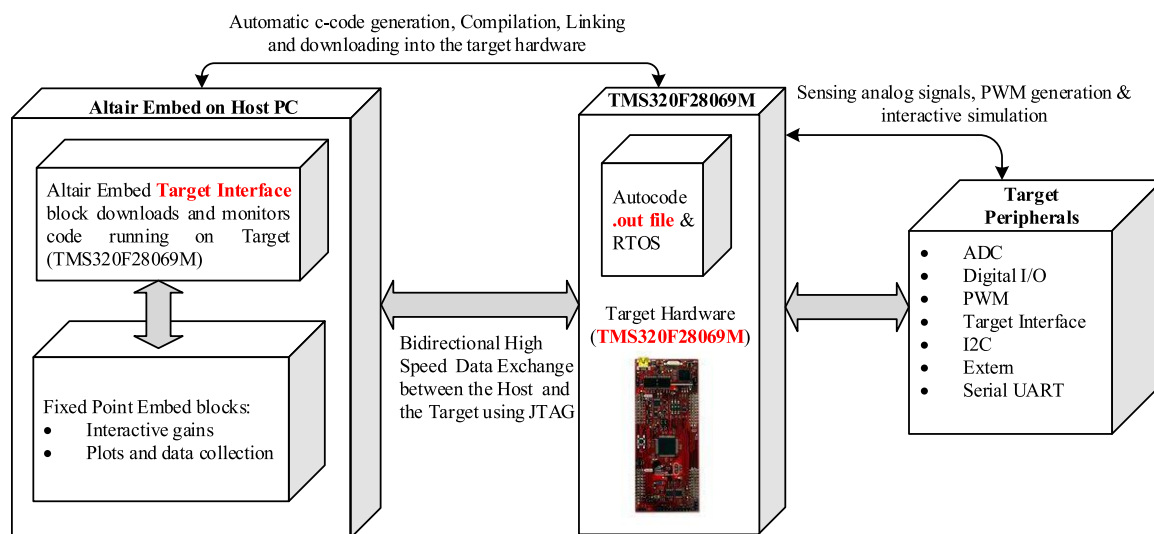


Figure B.4: Model Based Design Framework using Altair Embed and TMS320F28069M for Rapid Control Prototyping and Interactive HIL simulation

The framework of MBD for controller design using Altair Embed is shown in Figure B.4. The MBD software and the backend software (Code composer studio) are installed on Host PC. A communication link is established between the target hardware (TMS320F28069M) and sT-Embed using the JTAG communication protocol. The controller design and specifications are finalized before deployment using preliminary simulation studies. The MBD approach for controller design using Altair Embed involves following steps:

1. The designed controller is drawn as model using fixed point blocks in Altair Embed and is checked for logical, syntax error or any overflows.
2. The Altair Embed tool generates the *c-code* compatible with chosen target hardware.
3. The generated *c-code* is compiled using code composer studio to generate .out file.
4. The .out file can either be used for *interactive HIL simulation* or can be burnt into flash of the target hardware for final deployment.

Bibliography

- Al-Atrash, H., Batarseh, I., and Rustom, K. (2010). Effect of measurement noise and bias on hill-climbing mppt algorithms. *IEEE transactions on aerospace and electronic systems*, 46(2):745–760.
- Antonello, R., Carraro, M., Costabeber, A., Tinazzi, F., and Zigliotto, M. (2017). Energy-efficient autonomous solar water-pumping system for permanent-magnet synchronous motors. *IEEE Transactions on Industrial Electronics*, 64(1):43–51.
- Ayop, R. and Tan, C. W. (2018). Design of boost converter based on maximum power point resistance for photovoltaic applications. *Solar Energy*, 160:322–335.
- Bašić, M., Bubalo, M., Vukadinović, D., and Grgić, I. (2021). Sensorless maximum power control of a stand-alone squirrel-cage induction generator driven by a variable-speed wind turbine. *Journal of Electrical Engineering & Technology*, 16(1):333–347.
- Bašić, M., Vukadinović, D., Grgić, I., and Bubalo, M. (2019). Energy efficient control of a stand-alone wind energy conversion system with ac current harmonics compensation. *Control Engineering Practice*, 93:104185.
- Bhende, C. N. and Malla, S. G. (2012). Novel control of photovoltaic based water pumping system without energy storage. *International Journal of Emerging Electric Power Systems*, 13(5).
- Boopathi, R., Jayanthi, R., and Ansari, M. M. T. (2020). Maximum power point tracking-based hybrid pulse width modulation for harmonic reduction in wind energy conversion systems. *Computers & Electrical Engineering*, 86:106711.
- Campos, R. A., do Nascimento, L. R., and Rütther, R. (2020). The complementary nature between wind and photovoltaic generation in brazil and the role of energy

- storage in utility-scale hybrid power plants. *Energy Conversion and Management*, 221:113160.
- Caracas, J. V. M., de Carvalho Farias, G., Teixeira, L. F. M., and de Souza Ribeiro, L. A. (2013). Implementation of a high-efficiency, high-lifetime, and low-cost converter for an autonomous photovoltaic water pumping system. *IEEE Transactions on Industry Applications*, 50(1):631–641.
- Chandel, S., Naik, M. N., and Chandel, R. (2015). Review of solar photovoltaic water pumping system technology for irrigation and community drinking water supplies. *Renewable and Sustainable Energy Reviews*, 49:1084–1099.
- Chandel, S., Naik, M. N., and Chandel, R. (2017). Review of performance studies of direct coupled photovoltaic water pumping systems and case study. *Renewable and Sustainable Energy Reviews*, 76:163–175.
- Chen, J., Lin, T., Wen, C., and Song, Y. (2016). Design of a unified power controller for variable-speed fixed-pitch wind energy conversion system. *IEEE Transactions on Industrial Electronics*, 63(8):4899–4908.
- Dadkhah, J. and Niroomand, M. (2018). Real-time mppt optimization of pv systems by means of dcd-rls based identification. *IEEE Transactions on Sustainable Energy*, 10(4):2114–2122.
- Daniel, S. A. and AmmasaiGounden, N. (2004). A novel hybrid isolated generating system based on pv fed inverter-assisted wind-driven induction generators. *IEEE Transactions on energy conversion*, 19(2):416–422.
- de Oliveira Ferreira, A., Brito, A. U., Galhardo, M. A. B., Ferreira, L., and Macêdo, W. N. (2020). Modeling, control and simulation of a small photovoltaic-wind water pumping system without battery bank. *Computers & Electrical Engineering*, 84:106619.
- Driemeier, C. and Zilles, R. (2010). Six-element circuit for maximum power point tracking in photovoltaic-motor systems with variable-frequency drives. *Progress in Photovoltaics: Research and Applications*, 18(2):107–114.

- Elgendy, M. A., Zahawi, B., and Atkinson, D. J. (2011). Assessment of perturb and observe mppt algorithm implementation techniques for pv pumping applications. *IEEE transactions on sustainable energy*, 3(1):21–33.
- Elgendy, M. A., Zahawi, B., and Atkinson, D. J. (2012). Assessment of the incremental conductance maximum power point tracking algorithm. *IEEE Transactions on sustainable energy*, 4(1):108–117.
- Elkholy, M. M. and Fathy, A. (2016). Optimization of a pv fed water pumping system without storage based on teaching-learning-based optimization algorithm and artificial neural network. *Solar Energy*, 139:199–212.
- Embed, A. (2021). Altair Embed[®] Applications. <https://www.altair.com/embed-applications/>. Accessed: 2021-09-27.
- Errouha, M., Derouich, A., Nahid-Mobarakeh, B., Motahhir, S., and El Ghzizal, A. (2019). Improvement control of photovoltaic based water pumping system without energy storage. *Solar Energy*, 190:319–328.
- Fannakh, M., Elhafyani, M. L., and Zouggar, S. (2018). Hardware implementation of the fuzzy logic mppt in an arduino card using a simulink support package for pv application. *IET Renewable Power Generation*, 13(3):510–518.
- Fathabadi, H. (2017). Novel maximum electrical and mechanical power tracking controllers for wind energy conversion systems. *IEEE Journal of Emerging and Selected Topics in Power Electronics*, 5(4):1739–1745.
- Femi, R., Sree Renga Raja, T., and Shenbagalakshmi, R. (2021). A positive output-super lift Luo converter fed brushless dc motor drive using alternative energy sources. *International Transactions on Electrical Energy Systems*, 31(2):e12740.
- Femia, N., Petrone, G., Spagnuolo, G., and Vitelli, M. (2005). Optimization of perturb and observe maximum power point tracking method. *IEEE transactions on power electronics*, 20(4):963–973.
- Femia, N., Petrone, G., Spagnuolo, G., and Vitelli, M. (2009). A technique for improving p&o mppt performances of double-stage grid-connected photovoltaic systems. *IEEE transactions on industrial electronics*, 56(11):4473–4482.

- Gholamshahi, A., Fadaeinedjad, R., Mohammadi, E., and Moschopoulos, G. (2019). A new control strategy for hybrid water pumping systems used by utilities in developing countries. In *2019 IEEE Applied Power Electronics Conference and Exposition (APEC)*, pages 2406–2413. IEEE.
- Gopal, C., Mohanraj, M., Chandramohan, P., and Chandrasekar, P. (2013). Renewable energy source water pumping systems—a literature review. *Renewable and Sustainable Energy Reviews*, 25:351–370.
- Hussain, J. and Mishra, M. K. (2016). Adaptive maximum power point tracking control algorithm for wind energy conversion systems. *IEEE Transactions on Energy Conversion*, 31(2):697–705.
- IEEFA (2018). Solar irrigation pumps can help India reach 38% of its green energy target. <https://ieefa.org/solar-irrigation-pumps-can-help-india-reach-38-of-its-green-energy-target/>. Accessed: 2021-09-27.
- Katherine, T. (2014). India Plans to Install 26 Million Solar-powered Water Pumps. <https://spectrum.ieee.org/energywise/green-tech/solar/india-plans-for-26-million-solar-water-pumps>. Accessed: 2021-09-27.
- Kazmi, S. M. R., Goto, H., Guo, H.-J., and Ichinokura, O. (2010). A novel algorithm for fast and efficient speed-sensorless maximum power point tracking in wind energy conversion systems. *IEEE Transactions on Industrial Electronics*, 58(1):29–36.
- Kewat, S., Singh, B., and Hussain, I. (2018). Power management in pv-battery-hydro based standalone microgrid. *IET Renewable Power Generation*, 12(4):391–398.
- Kivimäki, J., Kolesnik, S., Sitbon, M., Suntio, T., and Kuperman, A. (2017a). Design guidelines for multiloop perturbative maximum power point tracking algorithms. *IEEE Transactions on Power Electronics*, 33(2):1284–1293.
- Kivimäki, J., Kolesnik, S., Sitbon, M., Suntio, T., and Kuperman, A. (2017b). Revisited perturbation frequency design guideline for direct fixed-step maximum power point tracking algorithms. *IEEE transactions on industrial electronics*, 64(6):4601–4609.

- Koreboina, V. B., Narasimharaju, B., and Kumar, D. V. (2017). Performance investigation of simplified pwm mppt approach for direct pv-fed switched reluctance motor in water pumping system. *IET Electric Power Applications*, 11(9):1645–1655.
- Koutroulis, E. and Kalaitzakis, K. (2006). Design of a maximum power tracking system for wind-energy-conversion applications. *IEEE transactions on industrial electronics*, 53(2):486–494.
- Krause, P. C., Wasynczuk, O., Sudhoff, S. D., and Pekarek, S. (2002). *Analysis of electric machinery and drive systems*, volume 2. Wiley Online Library.
- Krishan, O. and Suhag, S. (2020). A novel control strategy for a hybrid energy storage system in a grid-independent hybrid renewable energy system. *International Transactions on Electrical Energy Systems*, 30(4):e12262.
- Kumar, R. and Singh, B. (2016). Bldc motor-driven solar pv array-fed water pumping system employing zeta converter. *IEEE Transactions on Industry Applications*, 52(3):2315–2322.
- Kumar, R. and Singh, B. (2019). Solar pv powered-sensorless bldc motor driven water pump. *IET Renewable Power Generation*, 13(3):389–398.
- Kumar, S. and Vijayakumar, K. (2020). Simulation and experimental comparative analysis of the dc-dc converter topologies for wind driven seig fed dc nanogrid. *Electric Power Systems Research*, 181:106196.
- Lara, D., Merino, G., and Salazar, L. (2015). Power converter with maximum power point tracking mppt for small wind-electric pumping systems. *Energy conversion and management*, 97:53–62.
- Lee, B.-K. and Ehsami, M. (2001). A simplified functional simulation model for three-phase voltage-source inverter using switching function concept. *IEEE transactions on industrial electronics*, 48(2):309–321.
- Li, G., Jin, Y., Akram, M., and Chen, X. (2017). Research and current status of the solar photovoltaic water pumping system—a review. *Renewable and Sustainable Energy Reviews*, 79:440–458.

- Ma, T., Yang, H., Lu, L., and Peng, J. (2014). Technical feasibility study on a standalone hybrid solar-wind system with pumped hydro storage for a remote island in hong kong. *Renewable energy*, 69:7–15.
- Maissa, F., Barambones, O., Lassad, S., and Fleh, A. (2017). A robust mpp tracker based on sliding mode control for a photovoltaic based pumping system. *International Journal of Automation and Computing*, 14(4):489–500.
- Malla, S. and Bhende, C. (2014). Voltage control of stand-alone wind and solar energy system. *International Journal of Electrical Power & Energy Systems*, 56:361–373.
- Merabet, A., Ahmed, K. T., Ibrahim, H., Beguenane, R., and Ghias, A. M. (2016). Energy management and control system for laboratory scale microgrid based wind-pv-battery. *IEEE transactions on sustainable energy*, 8(1):145–154.
- Mezghani, D., Mami, A., and Dauphin-Tanguy, G. (2020). Bond graph modelling and control enhancement of an off-grid hybrid pumping system by frequency optimization. *International Journal of Numerical Modelling: Electronic Networks, Devices and Fields*, 33(4):e2717.
- Miller, A., Muljadi, E., and Zinger, D. S. (1997). A variable speed wind turbine power control. *IEEE Transactions on Energy Conversion*, 12(2):181–186.
- Miranda, M. S., Lyra, R. O., and Silva, S. R. (1999). An alternative isolated wind electric pumping system using induction machines. *IEEE transactions on energy conversion*, 14(4):1611–1616.
- Mishra, A. K. and Singh, B. (2017). Solar photovoltaic array dependent dual output converter based water pumping using switched reluctance motor drive. *IEEE Transactions on Industry Applications*, 53(6):5615–5623.
- Mishra, J., Pattnaik, M., and Samanta, S. (2019). Drift-free perturb and observe mppt algorithm with improved performance for seig-based stand-alone wind energy generation system. *IEEE Transactions on Power Electronics*, 35(6):5842–5849.
- Mohan, N., Undeland, T. M., and Robbins, W. P. (2003). *Power electronics: converters, applications, and design*. John wiley & sons.

- Moulay-Idriss, C. and Mohamed, B. (2013). Application of the dtc control in the photovoltaic pumping system. *Energy conversion and management*, 65:655–662.
- Mudlapur, A., Ramana, V. V., Damodaran, R. V., Balasubramanian, V., and Mishra, S. (2019). Effect of partial shading on pv fed induction motor water pumping systems. *IEEE Transactions on Energy Conversion*, 34(1):530–539.
- Muhsen, D. H., Khatib, T., and Nagi, F. (2017). A review of photovoltaic water pumping system designing methods, control strategies and field performance. *Renewable and Sustainable Energy Reviews*, 68:70–86.
- Muljadi, E. (1997). Pv water pumping with a peak-power tracker using a simple six-step square-wave inverter. *IEEE Transactions on industry applications*, 33(3):714–721.
- Murshid, S. and Singh, B. (2019). Energy-efficient single-stage solar pv powered sensorless pmsm drive for water pumping. *IET Renewable Power Generation*, 13(13):2267–2277.
- Narayana, V., Mishra, A. K., and Singh, B. (2017). Development of low-cost pv array-fed srm drive-based water pumping system utilising csc converter. *IET Power Electronics*, 10(2):156–168.
- Nindra, S., Paila, L. R., Natarajan, K., and Parvathy, S. M. (2019). Experimental investigation on a new hybrid system employing wind-driven dfig and solar pv panels. *Journal of The Institution of Engineers (India): Series B*, 100(6):561–574.
- Olhoff, A. and Christensen, J. M. (2020). Emissions gap report 2020. Technical report, UNEP DTU Partnership.
- Ouchbel, T., Zouggar, S., Elhafyani, M., Seddik, M., Oukili, M., Aziz, A., and Kadda, F. (2014). Power maximization of an asynchronous wind turbine with a variable speed feeding a centrifugal pump. *Energy conversion and management*, 78:976–984.
- Packiam, P., Jain, N., and Singh, I. (2015). Steady and transient characteristics of a single stage pv water pumping system. *Energy Systems*, 6(2):173–199.

- Parida, A. and Chatterjee, D. (2018). Stand-alone ac-dc microgrid-based wind-solar hybrid generation scheme with autonomous energy exchange topologies suitable for remote rural area power supply. *International Transactions on Electrical Energy Systems*, 28(4):e2520.
- Parida, A., Choudhury, S., and Chatterjee, D. (2018). Microgrid based hybrid energy co-operative for grid-isolated remote rural village power supply for east coast zone of india. *IEEE Transactions on Sustainable Energy*, 9(3):1375–1383.
- Paz, F. and Ordonez, M. (2014). Zero oscillation and irradiance slope tracking for photovoltaic mppt. *IEEE Transactions on Industrial electronics*, 61(11):6138–6147.
- Periasamy, P., Jain, N., and Singh, I. (2015). A review on development of photovoltaic water pumping system. *Renewable and Sustainable Energy Reviews*, 43:918–925.
- Pradhan, S., Singh, B., Panigrahi, B. K., and Murshid, S. (2019). A composite sliding mode controller for wind power extraction in remotely located solar pv–wind hybrid system. *IEEE Transactions on Industrial Electronics*, 66(7):5321–5331.
- Prakash, S. L., Arutchelvi, M., and Jesudaiyan, A. S. (2016). Autonomous pv-array excited wind-driven induction generator for off-grid application in india. *IEEE Journal of Emerging and Selected Topics in Power Electronics*, 4(4):1259–1269.
- Priyadarshi, N., Padmanaban, S., Bhaskar, M. S., Blaabjerg, F., and Holm-Nielsen, J. B. (2020). An improved hybrid pv-wind power system with mppt for water pumping applications. *International Transactions on Electrical Energy Systems*, 30(2):e12210.
- Rawat, R., Kaushik, S., and Lamba, R. (2016). A review on modeling, design methodology and size optimization of photovoltaic based water pumping, standalone and grid connected system. *Renewable and Sustainable Energy Reviews*, 57:1506–1519.
- Rehman, S. and Sahin, A. Z. (2016). A wind-solar pv hybrid power system with battery backup for water pumping in remote localities. *International Journal of Green Energy*, 13(11):1075–1083.

- Rezkallah, M., Chandra, A., Tremblay, M., and Ibrahim, H. (2019). Experimental implementation of an apc with enhanced mppt for standalone solar photovoltaic based water pumping station. *IEEE Transactions on Sustainable Energy*, 10(1):181–191.
- Rezkallah, M., Hamadi, A., Chandra, A., and Singh, B. (2018). Design and implementation of active power control with improved p&o method for wind-pv-battery-based standalone generation system. *IEEE Transactions on Industrial Electronics*, 65(7):5590–5600.
- Sashidhar, S., Reddy, V. G. P., and Fernandes, B. (2018). A single-stage sensorless control of a pv-based bore-well submersible bldc motor. *IEEE Journal of Emerging and Selected Topics in Power Electronics*, 7(2):1173–1180.
- Shaltout, A. and Abdel-Halim, M. (1995). Solid-state control of a wind-driven self-excited induction generator. *Electric Machines and Power Systems*, 23(5):571–582.
- Shukla, S. and Singh, B. (2018). Reduced current sensor based solar pv fed motion sensorless induction motor drive for water pumping. *IEEE Transactions on Industrial Informatics*, 15(7):3973–3986.
- Singh, B., Sharma, U., and Kumar, S. (2018). Standalone photovoltaic water pumping system using induction motor drive with reduced sensors. *IEEE transactions on industry applications*, 54(4):3645–3655.
- Singh, B. and Shukla, S. (2018). Induction motor drive for pv water pumping with reduced sensors. *IET Power Electronics*, 11(12):1903–1913.
- Singh, S. and Singh, B. (2015). Solar pv water pumping system with dc-link voltage regulation. *International Journal of Power Electronics*, 7(1-2):72–85.
- Sontake, V. C. and Kalamkar, V. R. (2016). Solar photovoltaic water pumping system—a comprehensive review. *Renewable and Sustainable Energy Reviews*, 59:1038–1067.
- Talbi, B., Krim, F., Rekioua, T., Mekhilef, S., Laib, A., and Belaout, A. (2018). A high-performance control scheme for photovoltaic pumping system under sudden irradiance and load changes. *Solar Energy*, 159:353–368.

- Traoré, A. K., Cardenas, A., Doumbia, M. L., and Agbossou, K. (2018). Comparative study of three power management strategies of a wind pv hybrid stand-alone system for agricultural applications. In *IECON 2018-44th Annual Conference of the IEEE Industrial Electronics Society*, pages 1711–1716. IEEE.
- Tutterow, V., Hovstadius, G., and McKane, A. (2002). Going with the flow: Life cycle costing for industrial pumpingsystems. Technical report, Ernest Orlando Lawrence Berkeley NationalLaboratory, Berkeley, CA (US).
- Vick, B. D. and Neal, B. A. (2012). Analysis of off-grid hybrid wind turbine/solar pv water pumping systems. *Solar Energy*, 86(5):1197–1207.
- Villalva, M. G., Gazoli, J. R., and Ruppert Filho, E. (2009). Comprehensive approach to modeling and simulation of photovoltaic arrays. *IEEE Transactions on power electronics*, 24(5):1198–1208.
- Vitorino, M. A., de Rossiter Corrêa, M. B., Jacobina, C. B., and Lima, A. M. N. (2011). An effective induction motor control for photovoltaic pumping. *IEEE Transactions on Industrial Electronics*, 58(4):1162–1170.
- Yao, Y., Bustamante, P., and Ramshaw, R. (1994). Improvement of induction motor drive systems supplied by photovoltaic arrays with frequency control. *IEEE Transactions on Energy conversion*, 9(2):256–262.
- Zeddini, M. A., Pusca, R., Sakly, A., and Mimouni, M. F. (2016). Pso-based mppt control of wind-driven self-excited induction generator for pumping system. *Renewable Energy*, 95:162–177.

Publications Based on the Thesis

Journals (Published/Accepted)

1. **Sachin Angadi**, Udaykumar R. Yaragatti, Yellasiri Suresh, A. B. Raju (2021). “Comprehensive Review on Solar, Wind and Hybrid Wind-PV Water Pumping Systems-An Electrical Engineering Perspective”. **CPSS Transactions on Power Electronics and Applications, (IEEE)** Vol. 6, No. 1, Pg 1-19
2. **Sachin Angadi**, Udaykumar R. Yaragatti, Yellasiri Suresh, A. B. Raju (2021). “System Parameter Based Performance Optimization of Solar PV Systems with Perturbation Based MPPT Algorithms”. **Energies, (MDPI)**, Vol 14, Issue 07, Pg 1-20
3. **Sachin Angadi**, Udaykumar R. Yaragatti, Yellasiri Suresh, A. B. Raju . “Design and Implementation of Constant Flux Controller for VSI Assisted SEIG Feeding Induction Motor Pump”, **International Journal of Power Electronics (Inderscience)**. **Paper Accepted**, Article in Press.
4. **Sachin Angadi**, Udaykumar R. Yaragatti, Yellasiri Suresh, A. B. Raju. “Speed Sensorless Maximum Power Point Tracking Technique for SEIG based Wind Energy Conversion System Feeding Induction Motor Pump”, **Electrical Engineering, (Springer)**, **Paper Accepted**, Article in Press.
5. **Sachin Angadi**, Udaykumar R. Yaragatti, Yellasiri Suresh, A. B. Raju. “An Effective Stand-alone Hybrid Wind-PV Water Pumping System with Reduced Power Converter Count” **International Transactions on Electrical Energy Systems (Wiley)**, Vol. 31, No. 12, Pg 13140.

Conferences (Published/Accepted)

1. **Sachin Angadi**, Udaykumar R. Yaragatti, Yellasiri Suresh, A. B. Raju (2020). “Implementation of Perturbation Based MPPT Technique Using Model Based Design”. **Electronic Systems and Intelligent Computing. Lecture Notes in Electrical Engineering, vol 686. Springer**, Singapore.

Biodata

Name : Sachin Angadi

Date of birth: 03-06-1989

Marital status: Married

E-mail: sachin@kletech.ac.in, sachinangadi@ieee.org

Mobile: +91-9060007631

Address

H#05, Ravindra Nagar

Unkal Extension

Hubli, Karnataka-580031, India.

Education

- M.Tech., Computers Application to Industrial Drives, National Institute of Engineering, Mysuru-570008, Karnataka, Aggregate-9.75, 2013
- B.E., Electrical & Electronics Engineering, B. V. Bhoomaraddi College of Engineering and Technology, Hubli-580031, Aggregate-9.19, 2011.
- Pre University Education, P. C. Jabin PU College of Science, Hubli-580031, Aggregate-82.5%, 2007.
- SSLC, Sri M R Sakhare English Medium School, Hubli-580031, Aggregate-89.92%, 2005.

Work Experience

- 25-05-2012 to 12-03-2013: Worked as Project Trainee in Control Electronics Division, ISRO Satellite Centre (ISAC), Bangalore.
- 01-08-2013 to Present, Working as Assistant Professor, Department of Electrical and Electronics Engineering, KLE Technological University, Hubballi-580031.

